Dissertation for the Degree of Doctor of Philosophy

Plasmonic nanowire waveguides and devices operating at telecom wavelengths

Tiberiu Rosenzveig

*

Raunvísindadeild
Verkfræði- og náttúruvísindasvið
Háskóli Íslands

Reykjavík, febrúar 2011

A Dissertation at the University of Iceland to be publicly examined in the Ceremonial Auditorium of the Main University Building, Monday, February 14, 2011 at 14:00 for the Degree of Doctor of Philosophy. The examination will be conducted in English

Doctoral Committee
Research Scientist Kristján Leósson (principal supervisor)
Department of Physics, University of Iceland
Assist. Prof. Alexandra Boltasseva (co-supervisor)
Department of Photonics Engineering, Technical University of Denmark
Prof. Hafliði P. Gíslason
Department of Physics, University of Iceland

Opponents
Prof. Pierre Berini
School of Information Technology and Engineering, University of Ottawa
Assist. Prof. Halldór Svavarsson
School of Science and Engineering, University of Reykjavik

Rosenzveig, T. 2011. Plasmonic nanowire waveguides and devices operating at telecom wavelengths. Acta Universitatis Islandiae. *Reykjavík Dissertations from the Faculty of Physical Sciences* . 167 pp. Printed in Iceland by Háskólaprent.

Tiberiu Rosenzveig, Faculty of Physical Sciences, University of Iceland, VR II, Hjardarhaga 2-6, IS-107 Reykjavík

© Tiberiu Rosenzveig 2011
ISBN 978-9979-9953-7-1

Ágrip

Í þessu verkefni er kynntur möguleikinn á að nota málmbylgjuleiðara sem grunneiningu fyrir ljósrás með stillanlegu gegnskini á bylgjulengd sem algeng er í ljósleiðarasamskiptakerfum (λ=1550 nm). Ljósrásin er samhæfð við hefðbundna ljósleiðara og ljósrásatækni. Bylgjuleiðarinn samanstendur af kjarna úr gullnanóvír sem umlukinn er kápu úr benzocyclobútan (BCB) fjölliðu, sem valin er með tilliti til þess hvernig ljóseiginleikar fjölliða breytast með hitastigi.

Nanóvírarnir eru með ferningslaga þverskurð, með hliðarlengd milli 150 nm og 200 nm. Í slíkum vírum má örva langsæknar rafgaseindir með því að tengja vírinn beint við hefðbundinn ljósleiðara. Fernings-samhverfa nanóvírsins tryggir að skautunarháð tap er í lágmarki. Útreikningar voru framkvæmdir með bútaaðferð til að meta áhrif lögunar vírs og kápu á sveifluhætti ljósleiðarans, auk þess sem áhrif viðloðunarlags undir gullinu voru könnuð. Besta lögun ljósleiðara var fundin, m.t.t. yfirfærslutaps, útbreiðslutaps og skautunarháðs taps. Stillanlegt gegnskin er fengið fram með því að senda rafstraum gegnum nanóvírinn og auka þannig hitastig vírsins og efnisins umhverfis hann. Hærra hitastig lækkar brotstuðul fjölliðunnar í kápunni, sem aftur hækkar útbreiðslutap vegna þess að aukinn hluti ljóssins sleppur frá ljósleiðaranum og út í kápuna. Ljóstapinu má stjórna nákvæmlega með því að stilla rafstrauminn sem rennur gegnum gullvírinn.

Ljósrásir byggðar á málmbylgjuleiðurum voru framleiddar með stöðluðum aðferðum í hreinherbergi, þ.á.m. ljóslitógrafíu, rafeindalitógrafíu og málmhúðun í lofttæmi. Sýnt var fram á virkni rásanna með litlum drifstraum. Rásirnar eru hlutfallslega litlar, hafa hátt myrkvunarhlutfall (>20 dB) og svörunartíma nálægt 1 ms, sem gerir þær vel samkeppnishæfar við aðrar gerðir ljósrása sem notaðar eru í sama tilgangi.

Abstract

In this work we present the possibility of using plasmon waveguides as an active, variable optical attenuator (VOA) operating at telecom wavelength (λ=1550 nm) that can be easily interfaced with existing fiber-optic technology and integrated optical circuits. The waveguides consist of a gold nanowire core embedded in a benzocyclobutene (BCB), a polymer chosen for its thermo-optic properties.

The nanowires have a symmetric, square cross-section with the sides between 150 nm and 200 nm. Long-range surface plasmon polaritons (LRSPP) are excited in the waveguides by means of end-fire coupling; due to their symmetry, the waveguides present low polarization-dependent loss (slightly over 1 dB). We performed finite element analysis to evaluate the effect of various cross-section geometries, thickness and width of the cladding or the presence of an adhesion layer beneath the Au core. The waveguides were optimized with respect to coupling and propagation loss as well as polarization-dependent loss. The optical attenuation is achieved by passing an electric current through the nanowire which raises the temperature of the wire and the surrounding polymer through Joule heating; the temperature increase lowers the refractive index of the cladding which in turn leads to added propagation loss as part of the plasmon uncouples into freely propagating light in the cladding. The level of attenuation can be controlled by the intensity of the current through the gold wire.

LRSPP waveguide samples were created making use of cleanroom fabrication techniques such as UV lithography, e-beam lithography and vacuum deposition of Au through thermal evaporation. The viability of the waveguides as a VOA driven by a small current was demonstrated. The devices have a small footprint, high extinction ratio (>20 dB) and switching times in the millisecond range, all of these make the LRSPP-based device a viable alternative to the existing competitors.

"It is sometimes said that scientists are unromantic, that their passion to figure out robs the world of beauty and mystery. But is it not stirring to understand how the world actually works [. . .]? It does no harm to the romance of the sunset to know a little bit about it."

– Carl Sagan

List of Papers

This thesis is based on the following papers, which are referred to in the text by their Roman numerals.

I **Compact plasmonic variable optical attenuator**
K. Leósson, T. Rosenzveig, P.G. Hermannsson, A. Boltasseva
Optics Express ***16****(20) (2008) 15546.*

II **Modelling of polarization-dependent loss in plasmonic nanowire waveguides**
T. Rosenzveig, P.G. Hermannsson, K. Leósson
Plasmonics ***5****(1) (2010) 75.*

III **Optimizing performance of plasmonic devices for photonic circuits**
T. Rosenzveig, P.G. Hermannsson, A. Boltasseva, K. Leósson
Applied Physics A ***100****(2) (2010) 341.*

IV **Demonstration of laser-fabricated DLSPPW at telecom wavelength**
A. Seidel, C. Reinhardt, T. Holmgaard, W. Cheng, T. Rosenzveig, K. Leósson, S.I. Bozhevolnyi, B.N. Chichkov
IEEE Photonics Journal ***2****(4) (2010) 652.*

Reprints were made with permission from the publishers.

Acknowledgements

I wish to thank my supervisor Kristján Leósson for his guidance and confidence during these past years that we have worked together. He is one of those rare types of leader who is always available with advice or instructions, but at the same time gives you the freedom to do things your own way. I also thank him for his patience on the occasions when I didn't meet the deadline while writing this thesis. I'd like to thank my co-supervisor Alexandra Boltasseva for her assistance during the time that I spent at the Danish Technical University, for showing me around the lab and the cleanroom and instructing me in the fabrication and measurement techniques she used. To my colleague Petur Hermannsson I thank for his involvement in the project, for his help with the numerical simulations, as well as for his friendship and the advice and opinions he has voiced both in and out of the lab.

I'd like to thank Carsten Reinhardt and his group from Hannover for our collaboration, for their great hospitality, for showing me around the city and for the making my short stay there both pleasant and productive. I would also like to thank Snorri Ingvarsson for making lab equipment available for the electromigration measurements and Mustafa Arikan for his help with automating the measurement process. I thank Peixiong Shi from the Danish Technical University (DTU) for his assistance with the e-beam lithography car-

ried out there and Christophe Peucheret, also from DTU, for his guidance concerning the polarization-dependent loss measurements. I wish to thank all the members of the group and my colleagues working at the Science Institute for the amazing atmosphere at the office, all the great time we had, the Monday waffles, the lunches on Wednesdays, the Friday burgers, the birthdays, the Christmas parties and generally the outstanding companionship.

On a more general note, I wish to thank my family: my late grandparents, my parents, Andrei and Cornelia, my brother Victor and my girlfriend Katja for their continued support, love and understanding. I'd also like to thank them all for putting up with me when I was, at times, grumpy, stressed or dismissive during the writing of this thesis; their encouragements and trust mean a great deal to me and they helped me maintain focus when I had difficulties.

I'd like to express my gratitude towards Andrei and Ileana Manolescu and Daniela Gunnarsson for welcoming me and making me feel at home when I was freshly arrived in a foreign land. Also, I'd like to thank Cosmin and Valeriu for their friendship and all the good times we had together.

While not directly involved with the work presented in this thesis, I wish to thank professors Patrice Baldeck and Simion Astilean who were my supervisors during my master's and undergraduate theses; it was they who raised my interest in the field of nanotechnology, in general, and nanophotonics, in particular. In the same vein, I wish to mention my pre-university physics teachers, Károly Bogdan, Valentin Cucer

and Vasile M. Gârba, who have nurtured my interest in physics and encouraged me to pursue a career in science.

The research presented in this thesis was financed by the Icelandic Research Fund, the Eimskip Research Fund at the University of Iceland and Icelandic Fund for Research Equipment. The research carried out in collaboration with Dr. Reinhardt's group at Laser Zentrum Hannover was supported by COST (European Cooperation in Science and Technology).

Contents

List of Figures **xvii**

1 Introduction **1**

2 Theoretical background **19**

2.1 Maxwell equations 20

2.2 Electromagnetic fields in metals 23

2.3 A metal-dielectric interface 26

2.4 A double interface 33

2.5 Strip and wire waveguides 38

3 Modelling **43**

3.1 The Finite Element Method 44

3.2 COMSOL Multiphysics 50

3.3 Simulation Results 53

4 Sample fabrication **67**

4.1 Strip waveguides 68

4.2 Nanowire waveguides 73

4.3 Dielectric-loaded waveguides 79

5 Experimental results **81**

5.1 Strip waveguide measurements 82

5.2 Nanowire waveguides 88
5.3 Dielectric-loaded waveguides 96

6 Conclusions 101

References 103

7 Included Papers 111

List of Figures

1.1 Surface plasmon propagating along a single and a double interface 2
1.2 Illustration of the cross-section of a strip waveguide and a nanowire waveguide 5
1.3 Schematic depiction of various types of SPP waveguides . 6
1.4 Dispersion curve of a SPP at a metal/dielectric interface . 8
1.5 The prism coupling technique for exciting surface plasmons 9
1.6 Various plasmon coupling techniques 10
1.7 Illustration of plasmon extinction due to resistive heating of the waveguide core 13
1.8 Plasmon-based variable optical attenuator 14

2.1 A surface plasmon polariton propagating at the interface between two media: ϵ_1 and ϵ_2 26
2.2 Propagation length and evanescent decay length of a surface plasmon polariton 32
2.3 A surface plasmon polariton propagating at a double interface in a dielectric/metal/dielectric structure 33
2.4 Propagation of a hybrid surface plasmon mode in a strip waveguide 38
2.5 Surface plasmon mode propagating along a nanowire waveguide 39

2.6 A schematic, cross-sectional representation of the plasmon modes supported by a nanowire waveguide 40

3.1 A triangular finite element and an arbitrary domain D meshed with triangular and quadrilateral elements 46
3.2 Example of a coarse mesh, a fine mesh and a mesh with elements of mixed sizes 49
3.3 Steps taken by COMSOL during the pre-processing, processing and post-processing stages 52
3.4 The coupling loss and propagation loss simulations when increasing the size of the gold nanowire core while maintaining the square cross-section. 57
3.5 Simulations for the coupling loss and propagation loss for nanowires with asymmetric cross-sections 59
3.6 Propagation loss simulations for nanowires with trapezoidal cross-sections 60
3.7 Propagation loss simulations for nanowires of various sizes in the presence of a Ti adhesion layer 61
3.8 Effects of polymer cladding size on propagation and coupling loss 63

4.1 Illustration of a negative- and positive-tone photoresist . . 70
4.2 The main steps of the UV lithography process 71
4.3 A schematic representation of the heat treatment of the polymer layers 73
4.4 AFM image of the e-beam resist after exposure and developing 74
4.5 SEM image of the e-beam resist before Au deposition . . . 75
4.6 Some of the major steps in the nanowire waveguide fabrication process 76
4.7 A mask design of the actual pattern used for our nanowire waveguide samples 77

4.8 A picture of a finished sample 77
4.9 An illustration of a DLSPPW and the main fabrication steps involved in its creation. 78
4.10 Microscope image of a DLSPPW sample 79

5.1 Experimental set-up for imaging plasmon mode fields and measuring insertion loss 83
5.2 Insertion loss results for 5-micron-wide Au strips 84
5.3 Propagation loss measurements for strip waveguides compared to theoretical results for an infinitely-wide double interface 85
5.4 Resistance measurements over time with a constant current applied to the strip waveguide 87
5.5 Constant current of different values applied to identical Au strips 88
5.6 Insertion loss measurements in nanowire waveguides at λ=1064 nm 89
5.7 Transmission through a 5 mm-long nanowire waveguide at variable input power levels 90
5.8 Waveguide mode image recorded with a CCD camera . . . 91
5.9 Mode profiles for $E^{1,0}$ plasmon propagating through waveguides of various lengths 92
5.10 Schematic representation of two polarization-dependent loss measurement techniques 93
5.11 Polarization-dependent loss measurements and theoretical estimates for 2 mm-long nanowire waveguides 95
5.12 Photograph of a 1 mm-long sample during the VOA measurements 96
5.13 Illustration of the leakage radiation microscopy set-up . . 97
5.14 Leakage radiation microscope images of SPPs propagating along straight waveguides 98

1

Introduction

Surface plasmon polaritons (SPP) are strongly bound electromagnetic waves which propagate along an interface between a metal and a dielectric (1, p. 20); they are distinct from the *bulk plasmons* which occur, as the name suggests, in the volume of a metal (also called *plasma oscillations*) (2, p. 19). SPPs travel along a metal/dielectric interface and decay exponentially into the two media perpendicular to the direction of propagation. This property of SPPs to be highly confined to the interface gives rise to high electric field intensities in relatively small volumes making the plasmon propagation highly sensitive to changes to the interface (defects, surface roughness, molecules adsorbed on the surface, etc.). Thus SPPs are well suited for various sensing applications, especially of biological molecules (3; 4). One example is the surface-enhanced Raman spectroscopy technique (SERS) where nanometer-scale surface roughness on a metallic film causes high intensity localized electric fields that, in turn, amplify the signal from molecules on the surface by several orders of magnitude (5); the technique is sensitive enough to be used for detecting single molecules (6). Other sensor techniques make use of Mach-Zehnder interferometers (7; 8) or plasmon waveguides sandwiching microfluidic channels (9). Besides the high sensitivity to the surface, the strong confinement of the electric fields allows surface plasmons to occupy volumes much smaller than the diffraction limit; this property gave rise to the field of *sub-wavelength optics*(10; 11) with applications such as: enhanced second harmonic generation (12) or transmission through sub-wavelength apertures (13).

On the other hand, because most of the electric field is concentrated at the interface between the metal and the dielectric, the SPP will be strongly attenuated as it propagates due to inelastic scattering on the electrons of the metal (ohmic loss). A measure of this is the *propagation loss* expressed in dB per unit of length, or more intuitively the *propagation length*, defined as the distance after which the electric field intensity associated with the SPP has decreased by a factor of e; for SPP in the infrared region traveling along a gold or silver interface the propagation length is typically on the micrometer scale (14, p. 7). One way to overcome the limitation of the short propagation length (15) is to use a

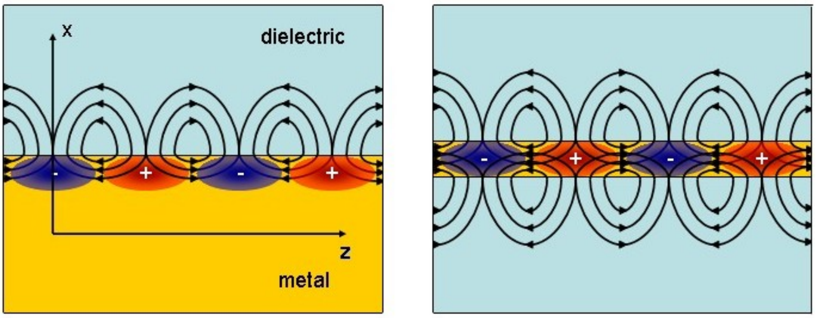

Figure 1.1: Schematic illustration of the electric field lines and charge distribution for surface plasmons propagating along a single interface between a dielectric and a metal (left) and a double interface, dielectric/metal/dielectric sandwich (right). The propagation is in the z direction.

structure which presents a double interface: instead of a metal in contact with a dielectric, a thin metallic film sandwiched between two dielectric media. If the metallic film is thin enough, comparable or smaller to the distance the plasmon penetrates into the media (also known as *evanescent decay length*, discussed later in chapter 2), the SPPs along the two interfaces can interact with each other and couple to form what is known as a *supermode*. This geometry supports a symmetric and antisymmetric supermode, of which the symmetric one has a propagation length several times longer than a single-interface plasmon, for this reason it is known as a *long-range surface plasmon polariton* (LRSPP) (1, p. 33). The LRSPP mode is less confined spacially than a plasmon propagating along a single interface, hence less of the electric field overlaps with the metal, resulting in lower attenuation. It should be noted however that one of the main advantages surface plasmons circuitry and devices have over existing fiber optic and dielectric waveguide technology is that the high confinement allows miniaturization of components below the diffraction limit. Since the main loss mechanism is dampening due to electrons in the metal, reducing loss by moving the electric field out of the metal will in result in a less confined mode. For the plasmonic devices presented in this thesis, minimizing propagation loss is essential, however, it should be noted that for some applications it might be preferable to trade off propagation length for a more confined plasmon (16). It should also be mentioned that a balance must be struck between reducing propagation loss and reducing confinement to the point where the plasmon is so loosely bound that small structural irregularities in the metallic film can couple it into freely propagating light (this might happen for example if the metallic film is too thin).

Types of waveguides

Since a waveguide for LRSPPs consisting of a metallic film between two layers of dielectric extending each to infinity above and below the film doesn't have any confinement laterally, the plasmon traveling along such a film would simply dissipate sideways. To circumvent this a waveguide geometry was proposed (17) where the infinitely-wide metal film was replaced by a metallic strip, or slab, of finite width encased all around in dielectric (see figure 1.2 below). The design calls for a metallic strip of few tens of nanometers thickness and a width of several microns. This geometry was later realized experimentally using gold strips encased in SiO_2 (18). These type of plasmonic waveguides are known as *strip waveguides*. We mention that while the waveguide designs we present in this work use the same dielectric for the top and bottom layers around the metallic components, this need not be the case. Designs where the metal rests on top of a polymer and is exposed to air on the other side are possible; one advantage they offer being that various probes (like the ones used in *scanning near-field optical microscopy* techniques discussed later) are able to get close to the plasmons within the *evanescent decay length* to interact with the electric fields perpendicular to the direction of travel. Another possibility is using two different dielectrics for the top and bottom cladding (19), with different thermo-optical properties for example, where this might suit a particular application (20).

The LRSPP supermode supported by these *strip waveguides*, similarly to the infinitely wide metallic film, are predominantly TM-polarized, that is the main component of the electric field is perpendicular to the metallic film or strip (and the magnetic field is transversal). These modes will be presented in chapter 2, however we note here that, while referring to them as TM- or TE-polarized, the modes of these geometries are hybrids that can be predominantly one polarization or the other, they are technically not pure TE or TM modes. As we'll see later, when using incoming light to excite surface plasmons, the efficiency of the process depends greatly on whether the polarizations of the exciting light and the plasmon mode match; this is a problem for applications where the polarization state of the incoming light is not known. To circumvent this, a waveguide with a symmetrical geometry was proposed: instead of using a metallic strip at the core of the waveguide, a wire with a square cross-section in the range of a hundred nanometers was suggested (21). Such a *nanowire waveguide*, due to its cross-sectional symmetry, would support arbitrarily polarized waves (figure 1.2). It is this geometry that we use in our plasmonic devices.

While not discussed in detail in this thesis, we mention several other types of surface plasmon waveguides. In the so-called *gap plasmons waveguides*, surface plasmons propagate along two metal surfaces separated by a narrow dielectric gap couple to form a supermode; the electric field of the plasmons is mostly located in the gap between the metal, hence it experiences low attenuation (22; 23). A somewhat similar geometry is the *channel plasmon waveguides*, where the plasmon travels along a groove ‘cut‘ in a metal slab, either covered by dielectric or exposed

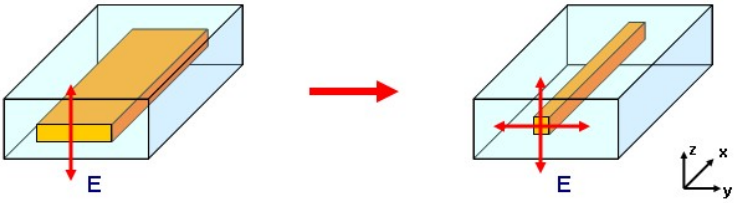

Figure 1.2: Illustration of the cross-section of a strip waveguide (left) and a nanowire waveguide with a symmetric core (right). While the strip waveguide only supports plasmon modes with the electric field perpendicular to the strip, the waveguide with the square cross-section supports both normal and transverse orientations of the electric field.

to air; the channel may have straight walls or a v-shape (see figure 1.3) (24; 25; 26). The inverse structure can also support plasmon propagation, that is instead of a v-shaped channel in the metal, the structure has a v-shaped metallic ridge with the plasmon traveling along the top edge (27), referred to as a *wedge plasmon*. An advantage of the gap and channel waveguides is that they strike a good balance between mitigating propagation losses and maintaining high enough confinement; structures have been suggested that would allow sharp 90^o bends with acceptable loss for practical applications (28), previously only accomplished with photonic crystal waveguides (29).

There have also been efforts to manufacture such geometries by nanoimprint lithography (30), which can significantly reduce both costs and production times (as it is a parallel process, that is several structures are fabricated simultaneously, as opposed to a sequential process, like writing the structures line-by-line with a laser or electron beam).

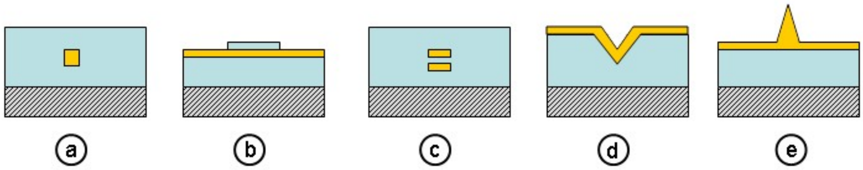

Figure 1.3: Schematic depiction of the cross section of various types of SPP waveguides: **a.**nanowire waveguide with a square cross-section; **b.**dielectric loaded waveguide; **c.**gap-plasmon waveguide; **d.**channel plasmon waveguide; **e.**wedge plasmon waveguide.

Exciting surface plasmon polaritons

Having covered the major types of plasmonic waveguides let us now look at how surface plasmons can be excited. It is possible to induce plasma oscillations in structures that can support them by using incident electrons or photons. Having electrons tunnel through various metallic films or junctions has been theorized (31) and observed (32; 33) to give rise to surface plasmons; this technique will not be further detailed here since the topic of this thesis is using plasmonic waveguides and devices in optical circuits.

The other method of exciting plasmons, by using incident light, can be broken down into two broad categories: techniques that couple light into a structure by matching the momentum of the incoming photons to that of the plasmons, and techniques that match the spatial distribution of the electric field, the so-called *mode profile*, of the two.

Figure 1.4 illustrates a typical plot of the plasmon *dispersion curve*, that is the the relation of the wavenumber k (which is tied to the momentum) and the frequency of a plasmon propagating at a metal/dielectric interface; the equations and the way to derive them are presented in the following chapter. The dashed black line in the figure represents the dispersion curve of light in the dielectric (e.g. air), called the *light line*. It is clear that at any given frequency the light propagating through free space has a smaller wavenumber than the plasmon of the same frequency this means that shining a light on a smooth metallic surface will not excite surface plasmons (1, p. 42). There are several ways to overcome this mismatch in momentum; one being the *prism coupling* method. The dashed blue line in figure 1.4 shows the light line inside a dielectric with a higher refractive index than the first one; this light has enough momentum to excite plasmons along the interface between the metal and the first dielectric. In practice the set-up consists of a prism (illustrated

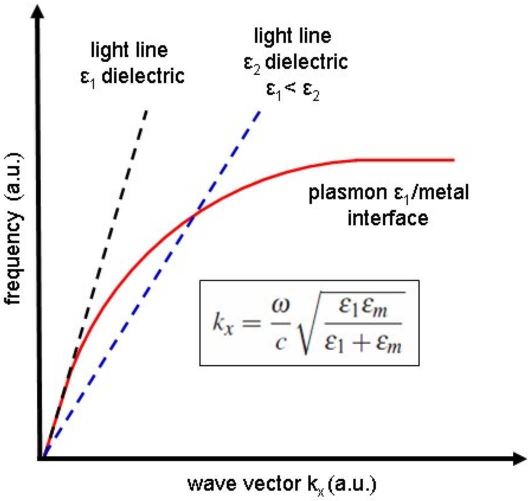

Figure 1.4: Dispersion curve of a SPP at a metal/dielectric interface. The black dashed line is the dispersion curve for a freely propagating lightwave in the dielectric; this light cannot couple to the plasmon modes supported by the interface because it has smaller momentum than the plasmon. The blue dashed line represents light propagating through a second dielectric with a larger dielectric constant than the first; this light has the necessary momentum to excite surface plasmons at the interface between dielectric 1 and the metal, but not at an interface between itself and a metal (dispersion curve not pictured)

in figure 1.5) in which the the incident light undergoes total internal reflection; the resulting evanescent wave excites surface plasmons on the air/metal interface of a thin metallic film deposited on the prism surface (Kretschmann configuration (34)) or a metallic surface separated by an air gap or dielectric from the face of the prism (Otto configuration (35)) or in a dielectric/metal/dielectric double interface (36). Another way of exciting surface plasmons, without adding the bulk and complexity of a prism, is to couple freely propagating light into the structure using a grating (37). The periodic structure of the grating adds to the wave vector parallel to the surface thus allowing light to couple into surface plsmons while still conserving momentum (1, p. 44). However, not just periodic gratings may be used for this, the presence of surface roughness (14) or metallic nanoparticles on the film (38) can accomplish similar results.

For our plasmonic devices we are more interested in the mode matching method. It is also called *end-fire coupling* because the end facet of an optical fiber is aligned with the input facet of the waveguide and if there is sufficient overlap between the fiber mode and the plasmon mode supported by the waveguide, the electromagnetic wave will efficiently ex-

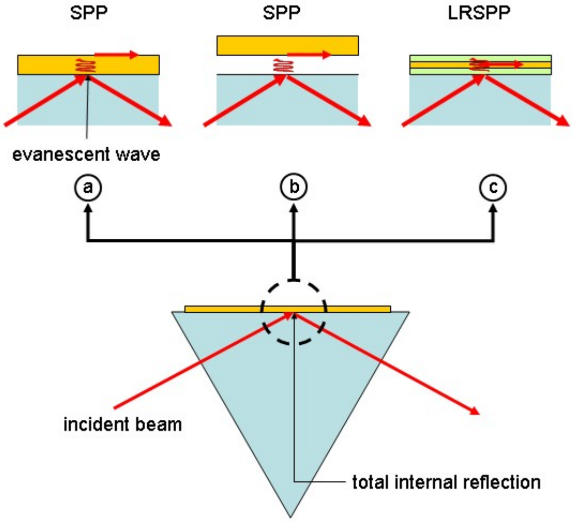

Figure 1.5: The prism coupling technique for exciting surface plasmons. The light suffers total internal reflection inside the prism and the resulting evanescent wave excites surface plasmon polaritons along a single interface in **a.**Kretschmann configuration and *b.*Otto configuration or **c.**a long-range surface plasmon polariton supported by a double interface

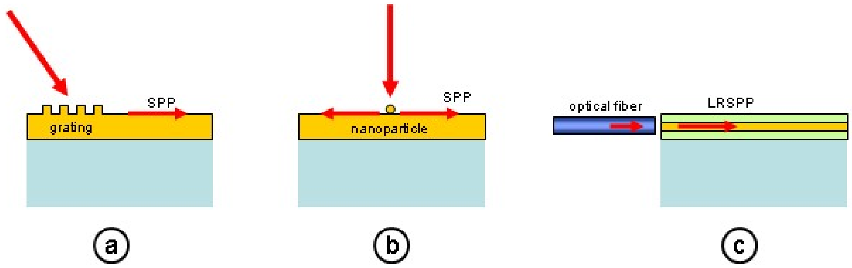

Figure 1.6: Other techniques for plasmon coupling: **a.**periodic grating method; **b.**scattering from a nanoparticle on a metallic film; **c.**end-fire coupling

cite the plasmon mode (39). The main advantage is that the technique doesn't require either bulky prisms or gratings or grooves that need to be designed and included into the structure during fabrication. Devices using end-fire coupling can easily be interfaced with existing optical fiber infrastructure without the need for extensive modifications. The end-fire coupling has a good efficiency which can be further improved by using an index matched liquid between the fiber and plasmon waveguide facets to eliminate reflections.

Characterizing surface plasmon polaritons

When imaging SPPs we distinguish between *near-field* techniques, which directly probe the evanescent components of the plasmon that penetrate the surrounding media and *far-field* techniques which study freely propagating light decoupled from the plasmon mode by defects or emitted by fluorescent molecules excited by the plasmon and others.

An example of near-field technique is the so-called *scanning near-field optical microscopy* (SNOM). A probe consisting of a strongly tapered optical fiber tip (sometimes also covered with a thin metal film) is brought in close proximity to the propagating SPP. The probe has to be close enough to interact with the exponentially decaying component of the plasmon that is normal to the direction of travel, this means typically distances in the 100 nm range; this precision and constant distance is achieved by using a cantilever and feedback system similar to the one used in atomic force microscopes. This method is useful for directly imaging the distribution of the electric field of a plasmon mode (1, p. 53).

Some of the far-field techniques include imaging scattered light from defects or perturbations at the interface (40) or decoupled light at the output facet of a plasmonic waveguide. Just as surface roughness may be used to couple freely propagating light into a plasmon-supporting structure, they may also be used to uncouple weakly bound SPPs resulting in emitted light which can be collected using conventional microscopy methods. The scattered light along a plasmon waveguide can be used to estimate the propagation losses or to work out the dispersion relation (1, p. 63). Imaging the light emitted from the output facet of a SPP waveguide can be used to determine the profile to the plasmon mode; our use of this technique is presented in the attached paper I.

Leakage radiation microscopy is another technique that can be used to investigate the propagation of SPPs (41). We made use of this method when characterizing *dielectric-loaded surface plasmon polariton waveguides* (DLSPPW) we fabricated (presented in chapter 4). A broader description of the technique and the experimental set-up is featured in chapter 5, while our results are detailed in paper IV.

Plasmonic waveguide applications

As we mentioned earlier, due to the strongly confined electric fields and the high sensitivity to the environment (surface defects, adsorbed molecules, refractive index changes, etc.) that are characteristic to surface plasmons, they have many potential applications as various sensors. Another large field of applications for SPPs is the use of plasmonic devices in optical circuits. The high confinement of the SPPs allows very compact components to be fabricated, presenting a tempting alternative to traditional dielectric-based and fiber optics components which are diffraction-limited. In the last decade there has been great interest in overcoming the limitations of SPPs and produce plasmon-based optical circuits that are competitive with existing telecom technologies (42; 43).

Based on their function, the components of an optical circuit can be divided into elements which guide the SPPs, such as straight waveguides, bends, Y-splitters, etc. and elements which modulate the signal or perform some simple function, e.g. directional couplers, ring resonators, variable attenuators, etc. A wide variety of components for directing surface plasmons, has been demonstrated for single interface plasmons: focusing lens (44), Bragg mirror (45), refractor (46), guiding and focusing by nanoparticle arrays (47) and others. Similarly, waveguiding solutions have been proposed and demonstrated for LRSPPs (straight and bent waveguides, Y-splitters) (48).

For functional optical circuits, besides waveguiding elements, components that can be used to manipulate the signal are also necessary; these can be divided into active and passive components. Examples of passive components for LRSPPs include, among others: ring resonators (49), Mach-Zender interferometers (50) or directional couplers (51). Among the active plasmonic devices we mention the use of a pumped gain medium to overcome propagation losses (52; 53) and components that rely on thermo-optic effects for inducing a phase change or a cutoff of the plasmon (20; 54).

One type of active plasmonic component, which is a central topic of this thesis, is the *variable optical attenuator* (VOA); this device, as the name suggests, allows one to control the extinction a signal put through the device experiences. The working principle of a VOA is illustrated in figure 1.7; the metallic core of the waveguide is connected to a source and an electric current is passed through it (in this case the presence of metallic components is a distinct advantage LRSPP waveguides have over their traditional, dielectric-based counterparts). The current causes Joule heating, raising the temperature of the wire and the dielectric surrounding it; this in turn causes the refractive index of the dielectric to increase or decrease, depending whether the medium's *thermo-optic co-*

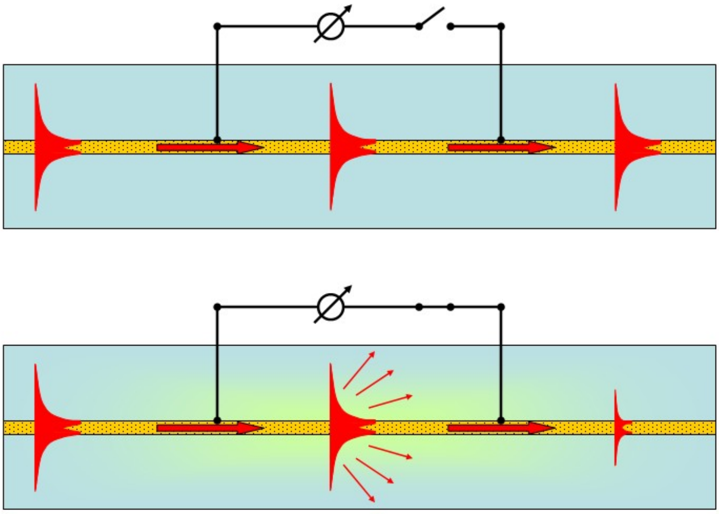

Figure 1.7: Illustration of plasmon extinction due to resistive heating of the waveguide core (inspired by (43))

efficient, $\partial n/\partial T$, is positive (e.g. glass) or negative (e.g. most polymers) respectively. Due to the weakly bound nature of the LRSPP mode, this change in the refractive index causes some of the plasmon to couple into freely propagating light, thus reducing the transmission or extinguishing it completely. The degree of attenuation is controlled by the temperature, which in turn depends on the voltage applied to the waveguide core. Such plasmon-based VOAs have been demonstrated operating at λ=1550 nm using gold strips embedded in polymer (55) and on a SiO_2 substrate (56) using the strips themselves as heaters as described above, and using a separate heater on the top polymer cladding (57).

In the examples listed previously the metal cores of the waveguides were gold strips 15-20 nm thick and a few microns wide. High attenuations of 20-30 dB were obtained at low operating powers (100mW). One inherent limitation of strip waveguides, as mentioned earlier, is that they only support mainly TM-polarized plasmon supermodes. In this thesis we propose a VOA that works on the same principle but utilizes a nanowire core instead of a strip, thus supporting, in theory, arbitrarily polarized

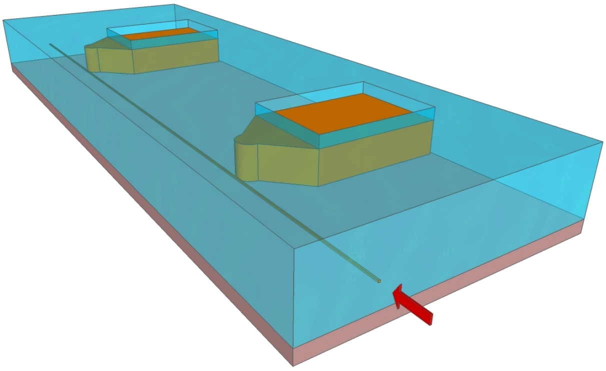

Figure 1.8: A schematic representation of the plasmonic VOA using a nanowire waveguide with a symmetrical square cross-section. The large rectangles are contact pads for electrodes

light which allows easier interfacing with existing fiber optic technologies. A rendering of the device is presented in figure 1.8. The resistive heating, heat dissipation and plasmon modes supported by the structure are modeled using (finite element method) software in order to design the optimum geometry; the samples are fabricated using cleanroom techniques and characterized using the cutback technique, mode profile imaging and polarization dependent loss measurements. Our VOAs should match or surpass the previous plasmonic devices in terms of attenuation, response time, power usage and insertion loss, but also be polarization-independent and maintain a small footprint.

Following is a summary outline of the chapters of this thesis:

Chapter 2 - Theoretical background

In the second chapter we present the theory behind the LRSPP waveguides. Starting from Maxwell's equations we derive the Helmholtz equation which describes a freely propagating electromagnetic wave. Then we consider the case of an electromagnetic wave inside a metal, the dispersion relation and bulk plasmon modes. Next, an electromagnetic wave bound to the interface between two media is analyzed, concluding that the interface must be between a metal and a dielectric and that only TM-polarized waves are supported. The LRSPP is introduced as a hybrid mode propagating along a suitably thin dielectric/metal/dielectric interface. Lastly, interfaces with lateral confinement, strips and wires, are discussed.

Chapter 3 - Modelling

As the cases of strip and nanowire waveguides can't be solved analytically, we resort to numerical methods for modeling our devices. We present the theoretical underpinnings of the finite element method and a commercially available software package, COMSOL Multiphysics, that was used for simulations. Studies of the influence of core asymmetry, adhesion layer and cladding geometry on insertion loss as well as heat dissipation in the waveguide are presented.

Chapter 4 - Sample fabrication

In this chapter the methods used to fabricate the samples are discussed. The cleanroom environment is introduced and standard micro- and nanofabrication techniques such as UV lithography, e-beam writing and vacuum deposition are illustrated. We go through the processing steps needed to manufacture micron-wide strip waveguides, nanowire waveguides with electrical contact pads for heating, in addition to describing fabrication of dielectric-loaded SPP waveguides.

Chapter 5 - Experimental results

We present the results of measurements performed on the manufactured waveguides. The shape and size of the mode field was measured for the strip and nanowire waveguides using CCD cameras operating at 1064 nm and 1550 nm wavelength. Cutback measurements were performed to derive the propagation and coupling loss. Fiber-to-fiber measurements were made on the heated VOAs and the attenuation as a function of the applied voltage and polarization dependence were investigated. The DL-SPPW were studied using leakage radiation microscopy techniques.

Chapter 6 - Conclusions

Lastly, some concluding remarks and future prospects are outlined.

2

Theoretical background

In this chapter we look at the theoretical tools needed to characterize the basic properties of surface plasmons. It was briefly mentioned in the introductory chapter that surface plasmon polaritons are electromagnetic waves strongly bound to, and propagating along, a metal-dielectric interface. However, before we tackle this problem, we look at how a metal interacts with electromagnetic radiation at different wavelengths. This interaction is described by the complex dielectric function $\hat{\epsilon}(\omega)$. In order to derive its expression we use a simplified model of a metal, the Drude model. While this model doesn't account for many properties of real metals (e.g. the electronic band structure) it does describe the interaction between electromagnetic waves and metals accurately enough for our purpose. We then look at the properties of waves propagating along a metal-dielectric interface as well as a double interface of a thin metal layer sandwiched between two semi-infinite dielectrics. In the latter case, when the metallic layer is thin enough for the two plasmons to interact, it can support long-range surface plasmon polaritons (LRSPP).

2.1 Maxwell equations

In order to characterize a freely propagating electromagnetic wave we start off with Maxwell's equations. At any given time, the state of an electromagnetic medium can be described by four quantities:

1. the number of electric charges per volume ρ
2. the number of electric dipoles per volume, called the polarization **P**
3. the number of magnetic dipoles per volume, called the magnetization **M**
4. the electric current per unit area, called the current density **J**

The Maxwell's equations describe how these physical quantities relate to each other:

$$\nabla \mathbf{E} = -\frac{1}{\epsilon_0} \nabla \mathbf{P} + \frac{\rho}{\epsilon_0} \tag{2.1}$$

$$\nabla \mathbf{H} = -\nabla \mathbf{M} \tag{2.2}$$

$$\nabla \times \mathbf{E} = -\mu_0 \frac{\partial \mathbf{H}}{\partial t} - \mu_0 \frac{\partial \mathbf{M}}{\partial t} \tag{2.3}$$

$$\nabla \times \mathbf{H} = \epsilon_0 \frac{\partial \mathbf{E}}{\partial t} + \epsilon_0 \frac{\partial \mathbf{P}}{\partial t} + \mathbf{J} \tag{2.4}$$

We now proceed to derive the Helmholtz equation that describes a propagating electromagnetic wave. We introduce the electric displacement **D** and the magnetic induction **B** defined by:

$$\mathbf{D} = \epsilon_0 \mathbf{E} + \mathbf{P} \tag{2.5}$$

$$\mathbf{H} = \frac{1}{\mu_0} \mathbf{B} - \mathbf{M} \tag{2.6}$$

The constant ϵ_0 is the electric permittivity of vacuum and μ_0 is the magnetic permeability of vacuum. By definition $\mu_0 = 4\pi \times 10^{-7}$[H/m]. The value of ϵ_0 must be determined through measurement. It is around $\epsilon_0 = 8.854 \times 10^{-12}$[F/m]. In isotropic and non-magnetic media we have:

$$\mathbf{D} = \epsilon \mathbf{E} \tag{2.7}$$

$$\mathbf{B} = \mu \mathbf{H} \tag{2.8}$$

ϵ and μ are the medium's electric permittivity and magnetic permeability, respectively. They are related to ϵ_0 and μ_0 thus:

$$\epsilon = \epsilon_r \epsilon_0 = (1 + \chi_e)\, \epsilon_0 \tag{2.9}$$

$$\mu = \mu_r \mu_0 = (1 + \chi_m)\, \mu_0 \tag{2.10}$$

The quantities ϵ_r and μ_r are the relative permittivity and permeability of the medium and χ_e and χ_m are called the electric and magnetic susceptibility of the medium. In light of the above, Maxwell's equations can be written:

$$\nabla \mathbf{D} = \rho \tag{2.11}$$

$$\nabla \mathbf{B} = 0 \tag{2.12}$$

$$\nabla \times \mathbf{E} = -\frac{\partial \mathbf{B}}{\partial t} \tag{2.13}$$

$$\nabla \times \mathbf{H} = \frac{\partial \mathbf{D}}{\partial t} + \mathbf{J} \tag{2.14}$$

Now we consider an electromagnetic wave in free space $\rho = 0$ and apply the following vector identity which will allow us to arrive at the Helmholtz equation:

$$\nabla \times \nabla \times \mathbf{A} = \nabla (\nabla \mathbf{A}) - \nabla^2 \mathbf{A} \tag{2.15}$$

Where ∇^2 is the Laplace operator and $\nabla^2 = \frac{\partial^2}{\partial x^2} + \frac{\partial^2}{\partial y^2} + \frac{\partial^2}{\partial z^2}$. We apply the identity 2.15 to equation 2.13:

$$\nabla \times \left(-\frac{\partial \mathbf{B}}{\partial t} \right) = \nabla \left(\nabla \mathbf{E} \right) - \nabla^2 \mathbf{E} \tag{2.16}$$

Considering eq. 2.8 and eq. 2.15, as well as the interchangeability of the time derivative and the curl operator, we may write:

$$\mu \frac{\partial}{\partial t} \left(\mathbf{J} + \frac{\partial \mathbf{E}}{\partial t} \right) = -\nabla^2 \mathbf{E} \tag{2.17}$$

Ohm's law gives us:

$$\mathbf{J} = \sigma \mathbf{E} \tag{2.18}$$

Where σ is the conductivity. Inserting the expression for **J** from Ohm's law in eq. 2.17, we get:

$$\mu \sigma \frac{\partial \mathbf{E}}{\partial t} + \mu \epsilon \frac{\partial^2 \mathbf{E}}{\partial t^2} = -\nabla^2 \mathbf{E} \tag{2.19}$$

If we consider **E** to be a plane wave:

$$\mathbf{E} = \mathbf{E}_0 e^{-i\omega t} \tag{2.20}$$

$$\frac{\partial \mathbf{E}}{\partial t} = -i\omega \mathbf{E} \tag{2.21}$$

$$\frac{\partial^2 \mathbf{E}}{\partial t^2} = -\omega^2 \mathbf{E} \tag{2.22}$$

then we arrive to:

$$\nabla^2 \mathbf{E} - \mu \omega^2 \left(\epsilon + \frac{\sigma i}{\omega} \right) \mathbf{E} = 0 \tag{2.23}$$

Equation 2.23 is the Helmholtz equation. We can define the complex permittivity $\hat{\epsilon}$:

$$\hat{\epsilon} = \epsilon + \frac{\sigma i}{\omega} \tag{2.24}$$

Next we take a look at the expression of the conductivity σ inside a metallic medium.

2.2 Electromagnetic fields in metals

Having addressed the problem of an electromagnetic wave propagating in free space, let us now consider one inside a metallic medium. The simplest model of a metal is the Drude model, named after German physicist Paul Drude (1863-1906). He proposed that, in a metal, the atomic nuclei and the core electrons that are attached to them are fixed, whereas the valence electrons are free to wander around almost like a free electron "gas" on the backdrop of the immobile ions. While this gross approximation of the complicated structure of a metal may seem a bit naive, the model does account for the DC and AC conductivity of metals, the Hall effect and magnetoresistance and thermal conductivity due to electrons. Below is a list of the relevant assumptions of the Drude model:

1. Other than the collisions, the interaction between electrons and other electrons as well as the interaction between electrons and the fixed ions is negligible. These are known as the independent electron approximation and the free electron approximation, respectively.

2. The collisions of the electrons are instantaneous

3. The average time between two collisions, called mean free time, is τ. The probability of an electron collision in the time interval dt is dt/τ.

The equation of motion for an electron in the presence of an external field **E** is:

$$m\frac{\partial^2 \mathbf{r}}{\partial t^2} + \frac{m}{\tau}\frac{\partial \mathbf{r}}{\partial t} = -e\mathbf{E} \tag{2.25}$$

where m is the mass of an electron and $\mathbf{r}$ is the coordinate of the electron. If the driving field has a form of $\mathbf{E} =$, then the displacement of the electron will also follow $\mathbf{r} =$.

$$-m\omega^2\mathbf{r} - \frac{i\omega m}{\tau}\mathbf{r} = -e\mathbf{E} \tag{2.26}$$

$$\mathbf{r} = \frac{e\tau}{m\left(\omega^2\tau + i\omega\right)}\mathbf{E} \tag{2.27}$$

The contribution of the displaced electrons to the polarization $\mathbf{P}$ is given by:

$$\mathbf{P} = -ne\mathbf{r} \tag{2.28}$$

where n is the number of electrons per unit of volume. Inserting Eq. 2.27 in Eq 2.28 and further in Eq 2.7, we have:

$$\mathbf{P} = -\frac{ne^2/m}{\omega^2 + i\omega/\tau}\mathbf{E} \tag{2.29}$$

$$\mathbf{D} = \epsilon_0\left(1 - \frac{ne^2/m\epsilon_0}{\omega^2 + i\omega/\tau}\right)\mathbf{E} \tag{2.30}$$

The term $ne^2/m\epsilon_0$ is called the plasma frequency:

$$\omega_p = \frac{ne^2}{m\epsilon_0} \tag{2.31}$$

From Eq 2.30 we also have the complex relative permittivity: $\hat{\epsilon_r} = \hat{\epsilon}/\epsilon_0$:

$$\hat{\epsilon_r} = 1 - \frac{\omega_p^2}{\omega^2 + i\omega/\tau} \tag{2.32}$$

We can separate the complex relative permittivity into its real and imaginary parts $\hat{\epsilon_r} = \epsilon_r' + \epsilon_r''$:

$$\epsilon_r' = 1 - \frac{\omega_p^2\tau^2}{1 + \omega^2\tau^2} \tag{2.33}$$

$$\epsilon_r'' = \frac{\omega_p^2 \tau}{\omega \left(1 + \omega^2 \tau^2\right)} \tag{2.34}$$

Furthermore, the complex refractive index can be defined as $\tilde{n} = \sqrt{\hat{\epsilon_r}}$, with its real and imaginary parts $\tilde{n} = n + i\kappa$

$$n^2 = \frac{\left(\epsilon_r'^{\,2} + \epsilon_r''^{2}\right)^{1/2} + \epsilon_r'}{2} \tag{2.35}$$

$$\kappa^2 = \frac{\left(\epsilon_r'^{\,2} + \epsilon_r''^{2}\right)^{1/2} - \epsilon_r'}{2} \tag{2.36}$$

The imaginary part κ represents the attenuation due to losses in a material. An electromagnetic wave with an initial intensity of I_0, propagating through a material with absorption coefficient α will have the intensity I after penetrating a distance d into the material. This is known as Beer's law.

$$I = I_0 e^{-d\alpha} \tag{2.37}$$

$$\alpha = \frac{2k\omega}{c} \tag{2.38}$$

Before we move on, let us take a look at the expression of the complex dielectric function for different values of ω. In the optical regime we have $\omega\tau >> 1$ which leads to:

$$\epsilon\prime_r = 1 - \frac{\omega_p^2}{\omega^2} \tag{2.39}$$

The plasmon frequency ω_p is the limit at which a Drude metal becomes transparent. If $\omega < \omega_p$, the electromagnetic radiation cannot propagate through the metal and is reflected. On the other hand, if $\omega > \omega_p$ metal will allow passage of the electromagnetic radiation. As pointed out earlier, the Drude model is not suitable for describing high-frequency regimes in real metals as it fails to account for interband electron transitions.

2.3 A metal-dielectric interface

We will now look at an electromagnetic wave propagating at the interface between a metal and a dielectric. These waves, coupled to the collective oscillations of the conduction electrons of the metal, give rise to so called surface plasmons. These plasmons, as opposed to bulk plasmons (collective electron oscillations in the volume of a metal), propagate along the interface and are strongly bound to it, decaying exponentially into the two media.

We consider the zero of the z axis to be at the interface. At this point

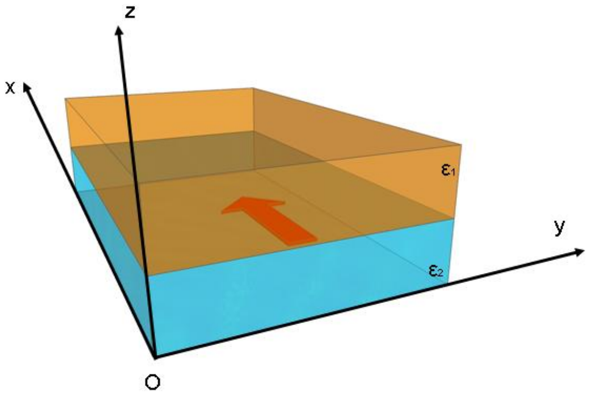

Figure 2.1: Schematic representation of a surface plasmon polariton propagating at the interface between two media characterized by ϵ_1 and ϵ_2; the two media extend to infinity in both direction of the z-axis

we do not make any assumptions about the nature of the two media, whether they are metallic or dielectric. Medium 1 extends to infinity in the positive direction on the z axis and is characterized by ϵ_1; medium two extends towards the negative direction of the z axis and is characterized by ϵ_2. Let us consider a propagating wave along the interface in the x direction: $\mathbf{E}\left(\mathbf{r},t\right)=\mathbf{E}\left(z\right)e^{i\beta x-i\omega t}$, where β is the propagation constant. If we insert this in the Helmholtz equation, it yields:

$$\frac{\partial^2\mathbf{E}}{\partial z^2}+\left(\omega^2\mu\hat{\epsilon}-\beta^2\right)\mathbf{E}=0 \tag{2.40}$$

Considering a harmonic time-dependence $e^{-i\omega t}$, Eq. 2.13 and Eq. 2.14 become:

$$\nabla\times\mathbf{E}=i\omega\mathbf{B} \tag{2.41}$$

$$\nabla\times\mathbf{B}=-i\omega\mu\hat{\epsilon}\mathbf{E} \tag{2.42}$$

This can be explicitly written:

$$\begin{bmatrix} 1 & 1 & 1 \\ \frac{\partial}{\partial x} & \frac{\partial}{\partial y} & \frac{\partial}{\partial z} \\ E_x & E_y & E_z \end{bmatrix}=i\omega\begin{bmatrix} B_x \\ B_y \\ B_z \end{bmatrix} \tag{2.43}$$

$$\begin{bmatrix} 1 & 1 & 1 \\ \frac{\partial}{\partial x} & \frac{\partial}{\partial y} & \frac{\partial}{\partial z} \\ E_x & E_y & E_z \end{bmatrix}=-i\omega\mu\hat{\epsilon}\begin{bmatrix} B_x \\ B_y \\ B_z \end{bmatrix} \tag{2.44}$$

$$\frac{\partial E_z}{\partial y}-\frac{\partial E_y}{\partial z}=i\omega B_x \tag{2.45}$$

$$\frac{\partial E_x}{\partial z}-\frac{\partial E_z}{\partial x}=i\omega B_y \tag{2.46}$$

$$\frac{\partial E_y}{\partial x}-\frac{\partial E_x}{\partial y}=i\omega B_z \tag{2.47}$$

$$\frac{\partial B_z}{\partial y} - \frac{\partial B_y}{\partial z} = -i\omega\mu\hat{\epsilon}E_x \tag{2.48}$$

$$\frac{\partial B_x}{\partial z} - \frac{\partial B_z}{\partial x} = -i\omega\mu\hat{\epsilon}E_y \tag{2.49}$$

$$\frac{\partial B_y}{\partial x} - \frac{\partial B_x}{\partial y} = -i\omega\mu\hat{\epsilon}E_z \tag{2.50}$$

But since $\frac{\partial}{\partial y} \to 0$ and $\frac{\partial}{\partial x} \to i\beta$, we have:

$$\frac{\partial E_y}{\partial z} = -i\omega B_x \tag{2.51}$$

$$\frac{\partial E_x}{\partial z} - i\beta E_z = i\omega B_y \tag{2.52}$$

$$i\beta E_y = i\omega B_z \tag{2.53}$$

$$\frac{\partial B_y}{\partial z} = i\omega\mu\hat{\epsilon}E_x \tag{2.54}$$

$$\frac{\partial B_x}{\partial z} - i\beta B_z = -i\omega\mu\hat{\epsilon}E_y \tag{2.55}$$

$$i\beta B_z = -i\omega\mu\hat{\epsilon}E_z \tag{2.56}$$

We find in literature that these equations allow for two solutions which represent two different polarizations: transverse magnetic (TM) with $E_x, E_z, B_y \neq 0$ and transverse electric (TE) with $B_x, B_z, E_y \neq 0$.
So for TM we have:

$$E_x = -i\frac{1}{\omega\mu\hat{\epsilon}}\frac{\partial B_y}{\partial z} \tag{2.57}$$

$$E_z = -\frac{\beta}{\omega\mu\hat{\epsilon}}B_y \tag{2.58}$$

$$\frac{\partial^2 B_y}{\partial z^2} + \left(\omega^2\mu\hat{\epsilon} - \beta^2\right) B_y = 0 \tag{2.59}$$

and for TE polarization:

$$B_x = \frac{i}{\omega}\frac{\partial E_y}{\partial z} \tag{2.60}$$

$$B_z = \frac{\beta}{\omega}E_y \tag{2.61}$$

$$\frac{\partial^2 E_y}{\partial z^2} + \left(\omega^2\mu\hat{\epsilon} - \beta^2\right) E_y = 0 \tag{2.62}$$

TM polarized modes

Now we apply the boundary conditions at the interface which require that the tangential components of **E** and **B** be continuous. First let us look at the TM modes. From eq. 2.59 at the interface we arrive to ${k_i}^2 = \beta^2 - \omega^2\mu_i\hat{\epsilon_i}$ for $i = 1, 2$ for the two sides of the interface, then, for medium 1, $z > 0$, we have:

$$B_y = A_1 e^{-k_1 z} e^{i\beta x} \tag{2.63}$$

$$E_x = iA_1\frac{k_1}{\omega\mu_1\hat{\epsilon_1}}e^{-k_1 z}e^{i\beta x} \tag{2.64}$$

$$E_z = -A_1 \frac{\beta}{\omega \mu_1 \hat{\epsilon_1}} e^{-k_1 z} e^{i\beta x} \tag{2.65}$$

and for medium 2, $z < 0$:

$$B_y = A_2 e^{k_2 z} e^{i\beta x} \tag{2.66}$$

$$E_x = -iA_2 \frac{k_2}{\omega \mu_2 \hat{\epsilon_2}} e^{k_2 z} e^{i\beta x} \tag{2.67}$$

$$E_z = -A_2 \frac{\beta}{\omega \mu_2 \hat{\epsilon_2}} e^{k_2 z} e^{i\beta x} \tag{2.68}$$

Here A_1 and A_2 are amplitude coefficients. As pointed out earlier, the tangential components need to be continuous B_y, E_x at the interface. To this we add the fact that we're dealing with non-magnetic media $\mu_1 = \mu_2 = \mu_0$
hence:

$$A_1 = A_2 \tag{2.69}$$

$$\frac{k_1}{k_2} = -\frac{\hat{\epsilon_1}}{\hat{\epsilon_2}} \tag{2.70}$$

In Eq. 2.70 both k_1 and k_2 need to be positive in order to have an electromagnetic wave which is strongly bound to the interface. This only happens if ϵ_1 and ϵ_2 are of opposite signs, that is one of the media has a metallic character and the other is a dielectric. There will be no SPPs propagating at the interface between two dielectric materials. By inserting the expressions for k_1 and k_2: ${k_i}^2 = \beta^2 - \omega^2 \mu_i \hat{\epsilon_i}$ in Eq. 2.70 we arrive to the dispersion relation:

$$\beta = \frac{\omega}{c} \sqrt{\frac{\hat{\epsilon}_{r1} \hat{\epsilon}_{r2}}{\hat{\epsilon}_{r1} + \hat{\epsilon}_{r2}}} \tag{2.71}$$

TE polarized modes

Now let us take a look at TE polarized waves. From Eq. 2.66 to 2.68 we get the following set of equations for the two media:
for $z > 0$:

$$E_y = A_1 e^{-k_1 z} e^{i\beta x} \tag{2.72}$$

$$B_x = -\frac{ik_1}{\omega} A_1 e^{-k_1 z} e^{i\beta x} \tag{2.73}$$

$$B_z = \frac{\beta}{\omega} A_1 e^{-k_1 z} e^{i\beta x} \tag{2.74}$$

for $z < 0$:

$$E_y = A_2 e^{k_2 z} e^{i\beta x} \tag{2.75}$$

$$B_x = \frac{ik_2}{\omega} A_2 e^{k_2 z} e^{i\beta x} \tag{2.76}$$

$$B_z = \frac{\beta}{\omega} A_2 e^{k_2 z} e^{i\beta x} \tag{2.77}$$

At the boundary E_y, B_x need to be continuous. This leads us to

$$k_1 + k_2 = 0 \tag{2.78}$$

but, as mentioned earlier, a bound mode at the interface requires that k_1 and k_2 is positive, which is in contradiction with eq. 2.78. We conclude that no TE polarized electromagnetic waves bound to the interface are possible. All SPP at a metal-dielectric interface are of TM polarization!

SPP propagation

The propagation of a SPP along an interface can be described by two quantities: *propagation length* and *evanescent decay length.* The propagation length describes the attenuation of the surface plasmon in the direction of travel; it is defined as the distance after which the intensity of the electric field has decreased by a factor of $1/e$, that is roughly to 37% of the original amplitude. The propagation length L is given by:

$$L = \frac{1}{2\mathbf{Im}(\beta)} \tag{2.79}$$

The evanescent decay length indicates how far the plasmon penetrates into the two media, on either side of the interface, perpendicular to the direction of propagation. The evanescent decay length $\hat{z}_i$, with $i = 1, 2$ for the two media, is defined as the distance after which the amplitude of the electric field, in the direction perpendicular to the propagation

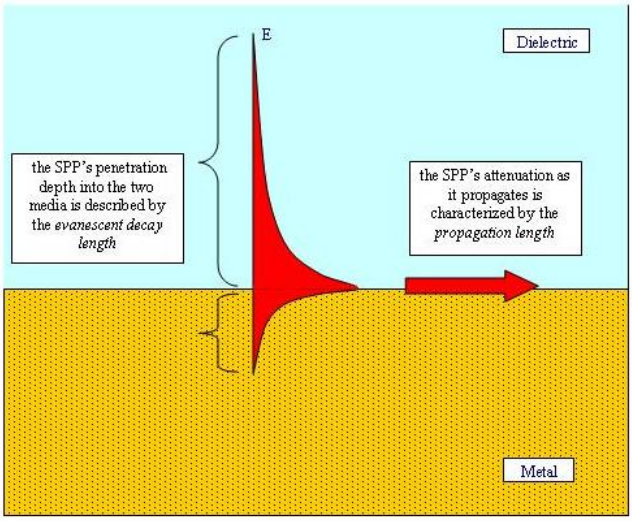
E
Dielectric
the SPP's penetration depth into the two media is described by the *evanescent decay length*
the SPP's attenuation as it propagates is characterized by the *propagation length*
Metal

Figure 2.2: Propagation length and evanescent decay length of a surface plasmon polariton

direction, has decreased by a factor of $1/e$, and is given by the formula:

$$\hat{z_i} = \frac{1}{|k_i|} \tag{2.80}$$

2.4 A double interface

Let us now consider an double interface. Our system becomes a thin metal layer sandwiched between two dielectric media. For simplicity we will consider the two dielectrics to be identical $\hat{\epsilon_{r1}} = \hat{\epsilon_{r2}}$, but this need not be the case. As in the case of a single interface, the SPPs are propagating along the x direction and the penetrate in the media along the z direction, decaying exponentially.

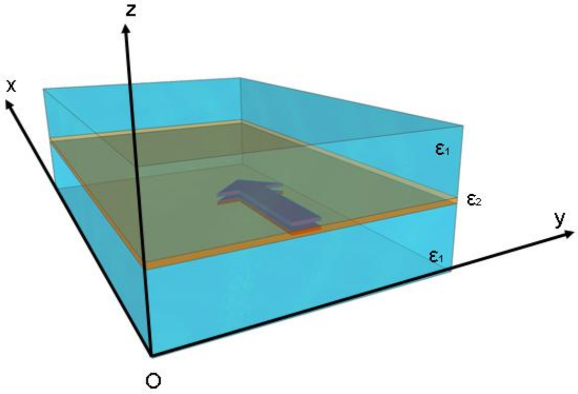

Figure 2.3: Schematic representation of a surface plasmon polariton propagating at a double interface in a dielectric/metal/dielectric structure

To work out the dispersion relation for a SPP propagating at this double dielectric/metal/dielectric interface, we follow the approach taken by Hermannsson in (58). We consider the metallic layer to have a thickness d and we will call half the thickness of the metallic layer a; $a = d/2$. We are only interested in bound modes, so only the TM polarization will be considered; described earlier by Eq. 2.57-2.59. We have ${k_i}^2 = \beta^2 - \omega^2 \mu_i \hat{\epsilon_i}$ for $i = 1, 2, 3$, which gives us:

$$\begin{aligned} B_y &= A_1 e^{-k_1(z-a)} e^{i\beta x} && z > a \\ B_y &= A_2 e^{k_1(z+a)} e^{i\beta x} && z < -a \\ B_y &= A_3 e^{k_2(z-a)} e^{i\beta x} + A_4 e^{-k_2(z+a)} e^{i\beta x} && -a < z < a \end{aligned} \tag{2.81}$$

If we plug this into Eq. 2.57-2.59, we get:
for $z > a$

$$B_y = A_1 e^{-k_1(z-a)} e^{i\beta x} \tag{2.82}$$

$$E_x = iA_1 \frac{k_1}{\omega \mu_1 \hat{\epsilon_1}} e^{-k_1(z-a)} e^{i\beta x} \tag{2.83}$$

$$E_z = -A_1 \frac{\beta}{\omega \mu_1 \hat{\epsilon_1}} e^{-k_1(z-a)} e^{i\beta x} \tag{2.84}$$

For $z < -a$ we have

$$B_y = A_2 e^{k_1(z+a)} e^{i\beta x} \tag{2.85}$$

$$E_x = -iA_2 \frac{k_1}{\omega \mu_1 \hat{\epsilon_1}} e^{k_1(z+a)} e^{i\beta x} \tag{2.86}$$

$$E_z = -A_2 \frac{\beta}{\omega \mu_1 \hat{\epsilon_1}} e^{k_1(z+a)} e^{i\beta x} \tag{2.87}$$

and $-a < z < a$

$$B_y = A_3 e^{k_2(z-a)} e^{i\beta x} + A_4 e^{-k_2(z+a)} e^{i\beta x} \tag{2.88}$$

$$E_x = -\frac{i}{\omega \mu_2 \hat{\epsilon_2}} \left(A_3 k_2 e^{k_2(z-a)} + A_4 k_2 e^{-k_2(z+a)} \right) e^{-i\beta x} \tag{2.89}$$

$$E_z = -\frac{\beta}{\omega\mu_2\hat{\epsilon_2}}\left(A_3 e^{k_2(z-a)} + A_4 e^{-k_2(z+a)}\right) e^{-i\beta x} \tag{2.90}$$

Requiring that B_y, E_x, E_y be continuous at the interfaces between media 1-2 and 2-3, we arrive to:
$z = a$

$$A_1 = A_3 + A_4 e^{-k_2 d} \tag{2.91}$$

$$\frac{k_1}{\hat{\epsilon_1}} A_1 = -\frac{k_2}{\hat{\epsilon_2}} A_3 + \frac{k_2}{\hat{\epsilon_2}} A_4 e^{-k_2 d} \tag{2.92}$$

and $z = -a$

$$A_2 = A_3 e^{-k_2 d} + A_4 \tag{2.93}$$

$$\frac{k_1}{\hat{\epsilon_1}} A_2 = -\frac{k_1}{\hat{\epsilon_1}} A_3 e^{-k_2 d} - \frac{k_2}{\hat{\epsilon_2}} A_4 \tag{2.94}$$

This can be written in matrix form

$$\begin{bmatrix} 1 & 0 & -1 & e^{-k_2 d} \\ 0 & 1 & -e^{-k_2 d} & -1 \\ \frac{k_1}{\hat{\epsilon_1}} & 0 & \frac{k_2}{\hat{\epsilon_2}} & -\frac{k_2}{\hat{\epsilon_2}} e^{-k_2 d} \\ 0 & \frac{k_1}{\hat{\epsilon_1}} & -\frac{k_2}{\hat{\epsilon_2}} e^{-k_2 d} & \frac{k_2}{\hat{\epsilon_2}} \end{bmatrix} \begin{bmatrix} A_1 \\ A_2 \\ A_3 \\ A_4 \end{bmatrix} = 0 \tag{2.95}$$

Equation 2.95 allow a non-trivial solution, that is $A_1, A_2, A_3, A_4 \neq 0$ if the determinant of the matrix on the left is zero. From this condition we arrive to the dispersion relation:

$$e^{-k_2 d} = \pm\frac{k_1/\hat{\epsilon_1} + k_2/\hat{\epsilon_2}}{k_1/\hat{\epsilon_1} - k_2/\hat{\epsilon_2}} \tag{2.96}$$

Let us now investigate the negative and positive solutions of the above equation.

Symmetric and antisymmetric plasmon modes

By inserting the negative solution in equation 2.95 and normalizing the constant $A_1 = 1$ we derive the y-component of the magnetic field in the three media:

$$B_y = e^{k_1(z+d/2)} e^{i\beta x} \qquad z < -d/2 \quad (2.97)$$

$$B_y = -\frac{\sqrt{(k_2/\hat{\epsilon_2})^2 - (k_1/\hat{\epsilon_1})^2}}{k_2/\hat{\epsilon_2}} e^{i\beta x} \cosh(k_2 z) \qquad -d/2 < z < d/2 \quad (2.98)$$

$$B_y = e^{-k_1(z-d/2)} e^{i\beta x} \qquad z > d/2 \quad (2.99)$$

This mode is also called the symmetric mode because the E_z component of the electric field is symmetric. Decreasing the thickness of the metallic film has a number of interesting effects on the propagation of this plasmon mode. We find in literature that as the metallic film becomes thinner, both the real and imaginary part of the propagation constant β decrease. When the film thickness goes to zero $d \to 0$, the propagation constant $\beta \to (\omega/c)\sqrt{\epsilon_{r1}}$. What does this mean for the propagation length L and evanescent decay length $\hat{z}$? Both the $\mathbf{Im}\beta \to 0$ and $k \to 0$ which results in $L \to \infty$ and $\hat{z} \to \infty$; the plasmon polariton mode becomes a plane wave propagating freely through the dielectric. In practice, as the thickness of the metal film is decreased, the plasmon becomes less confined to the interface (reflected by a longer evanescent decay length). Thus, the symmetric mode is loosely bound to the interface, which results in less absorption in the metal and consequently a propagation length orders of magnitude higher than a SPP propagating at a single interface. Due to this, the symmetric mode is also called a *long-range surface plasmon polariton* (LRSPP). It should be noted that a real metal/dielectric interface presents surface roughness as well as defects in the metal -grain boundaries, vacancies,etc.- all of which cause additional loss due to scattering. Because of its properties, the LRSPP is most suited for transmitting signals over long distances: on the millimeter scale as opposed to a few microns in case of the SPP at single interfaces. It is the LRSPP that we are interested in for use our variable optical attenuator.

Next, by inserting the positive solution of Eq. 2.96 in the matrix equation 2.95, we arrive to:

$$B_y = -e^{k_1(z+d/2)}e^{i\beta x} \qquad z < -d/2 \qquad (2.100)$$

$$B_y = -\frac{\sqrt{(k_1/\hat{\epsilon_1})^2 - (k_2/\hat{\epsilon_2})^2}}{k_2/\hat{\epsilon_2}} e^{i\beta x}\sinh(k_2 z) \qquad -d/2 < z < d/2 \qquad (2.101)$$

$$B_y = e^{-k_1(z-d/2)}e^{i\beta x} \qquad z > d/2 \qquad (2.102)$$

This is called an antisymmetric mode, because E_z and B_y are antisymmetric. When the thickness d of the metal film is decreased, we find that both the real and imaginary part of the propagation constant β increase. This results in a very strongly confined plasmon, with high losses due to absorption in the metal as it propagates and thus a propagation length that is shorter than the propagation length of a SPP at a single interface. Because of this, this mode is also referred to as a *short-range surface plasmon polariton* (SRSPP).

2.5 Strip and wire waveguides

In the previous chapters we have presented SPP propagating along the interface between a metal and a dielectric and concluded that a LR-SPP (the symmetric mode propagating at a dielectric/metal/dielectric interface) yields the longest propagation length and is best suited for our application. However, we have not included any lateral confinement yet in our analysis. An LRSPP propagating along an 'infinitely-wide' (from the plasmon's point of view) interface would have the possibility to quickly dissipate sideways. In 1999 Berini demonstrated the theoretical possibility of using a thin metallic strip of finite width encased in a dielectric to support plasmon propagation.

The plasmon modes supported by such a structure cannot be determined analytically and are instead characterized by numerical methods such as

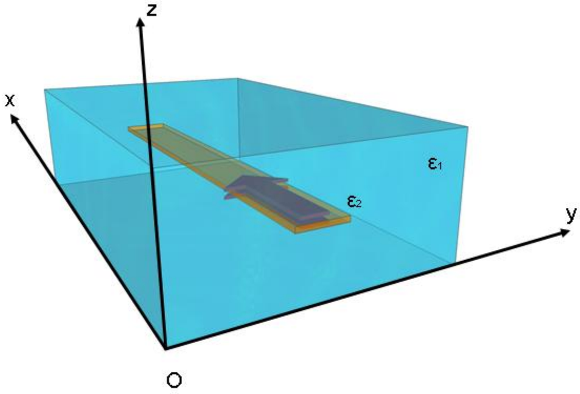

Figure 2.4: Propagation of a hybrid surface plasmon mode in a strip waveguide

the finite element method or the method of lines (used by Berini). These strip waveguides support four fundamental modes all of which are mostly TM polarized (these modes aren't pure TM modes, but the electric field has a predominant E_y component). One of the four fundamental modes is a non-radiative, bound mode that is symmetric in both x and y directions; this mode is the LRSPP mode. In the year 2000 the finite-width strip waveguides predicted theoretically were demonstrated experimentally in the form of a 20 nm thick, 8 μm wide Au strip embedded in SiO_2, operating at a free-space wavelength λ=1550 nm. The LRSPPs supported by such structures can be excited by end-fire coupling, however a polarization-maintaining optical fiber is required to ensure a TM polarized light.

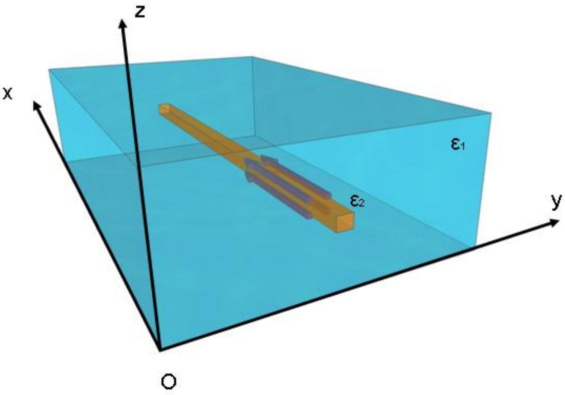

Figure 2.5: Surface plasmon mode propagating along a nanowire waveguide. The hybrid mode is made up of corner-modes

In order to obtain a waveguide that doesn't discriminate between a TM or TE polarized light from the input fiber, Berini suggested replacing the metallic strip (where the width is much larger than the height) with a metallic wire which has a symmetric, square cross-section (21). As in the case of the strip waveguides, the modes supported by the nanowires are coupled modes (sometimes called supermodes) formed from simpler modes. Unlike the strip waveguides though, we find in literature that for sufficiently narrow wires these modes are not formed from modes propagating on the sides of the square, rather it is corner-modes that couple to give rise to the supermodes. It should be noted that, similar to the double interface and the strip waveguides, if the cross-section of the wire is larger than a certain threshold, the corner mode are too far from each other to interact and a coupled mode is not formed.

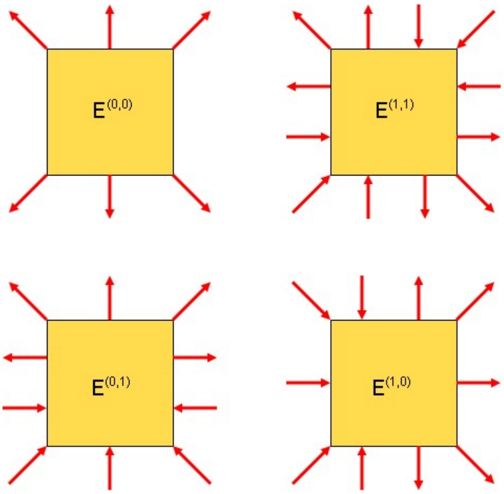

Figure 2.6: A schematic, cross-sectional representation of the plasmon modes supported by a nanowire waveguide (adapted from (59))

There are four modes that may be supported by a waveguide with a square cross-section and they can be designated(59): $E^{(0,0)}$, $E^{(1,0)}$, $E^{(0,1)}$ and $E^{(1,1)}$. Of these $E^{(0,1)}$ and $E^{(1,0)}$ are LRSPP modes and are orthogonally polarized.

So, we have found that a metal nanowire encased in a dielectric can serve as a waveguide for LRSPPs and can also be polarization-independent. In the next chapter we look at how we model the electric field distribution inside such a waveguide using the finite element method, then we determine the optimal geometry for a gold wire waveguide operating at telecom wavelength, λ=1550 nm.

3

Modelling

In the previous chapter we have seen how electromagnetic radiation confined at the interface between two media with dielectric constants of opposite signs (a metal and a dielectric) can give rise to plasmon waves propagating along that interface. As we have previously stated, analytical solutions can only be obtained for a single interface and a double interface (dielectric/metal/dielectric layers) between semi-infinite media. Once a lateral confinement is introduced, in the case of metallic strips or wires embedded in dielectric, the differential equations describing the system can no longer be solved analytically, so an approximate numerical solution is sought instead.

In this chapter we present the model that was used to estimate the insertion losses of our nanowire waveguides before fabrication. We used COMSOL Multiphysics (TM) software package which employs the finite element method to produce a numerical solution for partial differential equations. We briefly present the core principles of the finite element method and then show how COMSOL can be used to map the electric field distribution across our structures and how the significant quantities like coupling loss and propagation loss can be derived from this.

3.1 The Finite Element Method

The finite element method, also known as finite element analysis, is a numerical method that allows approximate solutions to be computed for certain types of problems involving partial differential equations. It is difficult to accurately pinpoint the origins of the finite element method. This method, when applied to real-world problems, yields a large system of linear or non-linear algebraic equations that can only be solved by using a computer. So, even though the mathematics and the principle of the finite element method have been around for the better part of the last century, it was not properly developed or gained widespread use until access to computing power became ubiquitous.

In 1943, R. Courant, a mathematician, published a paper (60) where he presented the possibility of numerically solving partial differential equations over a domain by dividing it into small triangular subdomains, finding a local solution within each subdomain while requiring that there be no discontinuity between adjacent subdomains and finally integrating over the entire domain. This, as we shall see, is the core of the finite element method. However, Courant's paper failed to gather much attention and the method was not further developed until the necessary computing power was more widely available. During the 50s the finite element method was used by the aeronautical industry to model mechanical stress in wings (61, p. 3). In 1956 Turner *et al.* published a paper (62) detailing the discretization of a domain into triangular and rectangular elements to model stress in 1-dimensional and 2-dimensional cases. Once computing power became more universally available, the finite element method also became more wide-spread. Since the 1980s the method has become available on personal computers (61, p. 3) and today it is being used in many different fields for problems such as fluid mechanics, heat transfer (from engine pistons to integrated circuits), sound propagation in solids and fluids (both stationary and in motion), chemical reaction kinetics, ion transport and diffusion, propagation of electromagnetic waves and many others.

The type of problems that the finite element method can be applied to are known as field problems, or alternatively, boundary value problems. In essence, there is a given domain with well defined boundaries over which some variables, known as field variables, need to be determined in every point of the domain. These field variables must satisfy a differential equation across the domain as well as some boundary conditions along the boundaries of the domain. Depending on the type of problem, the field variables may represent different physical quantities, such as: displacement for mechanical stress analysis, fluid velocity for problems of fluid dynamics, temperature in case of heat transfer problems or electric field intensity for optical applications.

Let us consider, for example, a 2-dimensional domain D of arbitrary shape and a variable $\varphi(x, y)$ that needs to be determined in every point of the domain. In most real-world problems an exact analytical solution will not be available and an approximate numerical solution will be sought instead. We can define a triangular element of finite size within our domain as shown in figure 3.1. This finite element is made up of three edges and three nodes. The nodes of this triangle are outside of the element so they are exterior nodes, however interior nodes may also be considered.

The values of the field variables $\varphi(x, y)$ are computed explicitly at the nodes of the element while at all the other points inside the element the values of the field variable are interpolated: $\varphi(x, y) = F_1\varphi_1 + F_2\varphi_2 + F_3\varphi_3$. Where F_1, F_2 and F_3 are interpolation functions and φ_1, φ_2 and φ_3 are the values of the field variable at the nodes which are treated as unknown constants that need to be determined. In order to compute the

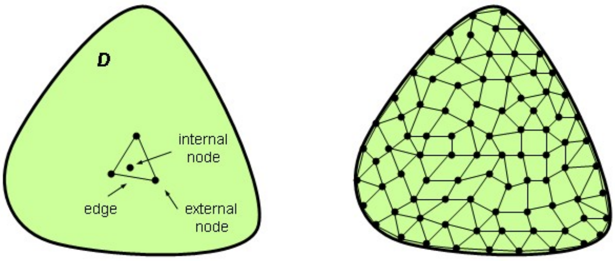

Figure 3.1: An arbitrary domain D with a triangular element. On the right, the same domain is *meshed* using triangular and quadrilateral elements; note that there are no gaps in the *mesh* and the elements connect at the nodes and along the sides without overlapping.

values of $\varphi(x, y)$ over the entire domain D, more triangular elements are considered that are connected at the exterior nodes and edges. These triangular elements cover the entire domain approximately and do not overlap with each other. This network of triangles is called a *mesh* and the process of dividing a domain into such elements is known as *meshing*. The mesh need not consist of triangular elements alone; quadrilateral elements or a mix of triangular and quadrilateral elements may also be used. Figure 3.2 shows how a mesh approximates the boundary of an irregular-shaped domain. By refining the mesh, that is decreasing the size of individual elements, a better approximation of the boundary is obtained. It is also imposed that the solution be continuous at the nodes connecting elements as well as across the inter-element edges. This way the solution is interpolated across the entire domain in piecewise fashion.

There are several methods for calculating the values of the field variable at the nodes, however, one technique that is easily applied to the finite element method is the weighted residual method. In essence, a test function is inserted into the differential equation and the result will differ from the correct solution by an amount we call a residual. By minimizing this residual, our test function approaches the solution. For sake of example, let us consider a differential equation:

$$D[f(x), x] = 0 \tag{3.1}$$

where $a < x < b$ and the boundary condition is:

$$f(a) = f(b) = 0 \tag{3.2}$$

We seek a solution that can be expressed as $g(x) = \sum c_i N_i(x)$, where c_i are unknown constant parameters and $N_i(x)$ are functions that are continuous over the domain and satisfy the boundary conditions. Inserting our proposed solution into the differential equation we find that our solution differs from the exact solution by a residual quantity:

$$D[g(x), x] = R(x) \tag{3.3}$$

The residual $R(x)$ also depends on the parameters c_i. For our approximate solution to approach the exact one these parameters need to be evaluated so that integral of the residual over the entire domain is zero; which can be formally written as:

$$\int_a^b w_i(x) R(x)\, dx = 0 \tag{3.4}$$

The functions w_i are *weighting functions* and there are several methods for choosing them (63, p. 8):

- *the collocation method:* the residual is required to become zero at specific points, equal in number to the parameters c_i. The weighting functions are of the form $w_i(x) = \delta(x - x_i)$.

- *the subdomain method:* the weighting function becomes unity $w_i(x) = 1$ over a region. The number of these regions is equal to the number of unknown parameters c_i.

- *the Galerkin method:* this is most frequently used in finite element software. The weighting functions are the same as the functions used in the approximate solution $w_i(x) = N_i(x)$. Hence equation 3.3 becomes:

  $$\int_a^b N_i(x)R(x)\,dx = 0 \tag{3.5}$$

  yielding n algebraic equations with a corresponding number of parameters c_i to be determined.

Another mathematical method which is often applied to similar, or the same, problems involving differential equations is the *finite difference method.* This method is also a numerical method and yields approximate solutions. The numerical solution is obtained by replacing the differentiable solution by a *grid function*; a function that is only defined at a finite number of points, called *grid points.* at these points the derivatives that appear in the function are replaced by an approximate finite quantity, since:

$$f\prime(a) = \lim_{h\to 0} \frac{f(a+h)-f(a)}{h} \approx \frac{f(a+h)-f(a)}{h} \tag{3.6}$$

The finite element method and the finite difference method are similar in the sense that both approach a differential equation problem by discretizing it and ultimately yield algebraic equations that need to be solved. There is also an equivalence between the nodes of the mesh in the finite element method and the grid points used in the finite difference method. It is at these points that the solutions are calculated explicitly in both methods. Also, by increasing the number of grid points and mesh nodes respectively, the approximate solutions of both methods approach the exact solution. The finite element method has some advantages over the finite difference methods:

- it can easily handle domains with irregular boundaries or complex geometrical shapes

- the mesh doesn't need to be uniform and denser meshes can be applied where the field variables are expected to vary rapidly (such as near the boundaries); this ensures that a correct solution is computed without requiring prohibitive computational resources

- the method can model domains which contain multiple materials each with different material properties and boundary conditions (including fluxes)

- the nature of the method allows for highly modular programming as the mesh generation is identical regardless of the nature of the field variables

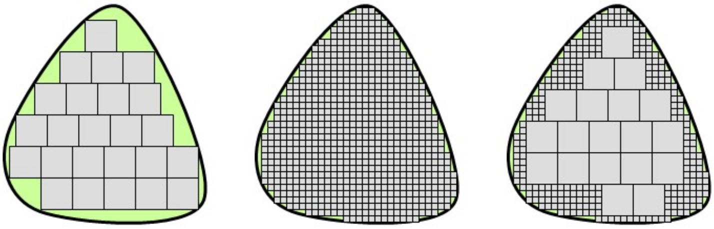

Figure 3.2: A coarse mesh might not cover the domain and since the field variables are computed explicitly only at the nodes and interpolated over the domain, a mesh like this may yield an invalid solution. A finer mesh has the advantage of providing enough nodes for characterizing the field variables along the boundary of the domain, however this comes at the cost of computing power. The ideal choice is to use a non-uniform mesh that is finer where the field variables are expected to vary fast over short distances and coarser mesh where this is not the case. (adapted from (64, p. 4))

3.2 COMSOL Multiphysics

COMSOL Multiphysics is a commercial software suite for modeling problems based on differential equations and extracting a solution using the finite element method. It comprises several modules designed for specific fields, such as electrical components, stress and strain analysis,acoustics ,heat transfer and others. These modules can be used in conjunction with one another in order to model processes where several phenomena overlap: *e.g.* the AC/DC module combined with the heat transfer module might be used to model Joule heating of electronic components or heat distribution inside an induction furnace; the AC/DC module together with the structural analysis module can describe piezoelectric components. In order to study the dependence of the insertion loss of the LRSPP on the specific geometry of the gold nanowires embedded in polymer we used COMSOL's RF module, designed for modeling electromagnetic waves (radio frequency, microwave, optical or high frequency) in various media. The RF module was used in conjunction with the heat transfer module for modeling the heating of the gold nanowire subjected to an electrical current and the effects on plasmon propagation.

COMSOL, like most finite element software (65, chapter 5), is subdivided into three routines: *the preprocessing step*, *the solution step* and *the postprocessing step*. During the preprocessing step, the problem's geometry is modeled in the computer. COMSOL provides a CAD-like (Computer Aided Design) interface for this purpose. Next, the material(s) making up the domain are defined through material constants relevant to the problem (these might be Young's modulus for a structural analysis problem, heat capacity and/or thermal conductivity for heat dissipation problems, etc). Once the geometry and the materials are defined, the domain is discretized into finite elements. The earliest finite element softwares needed the user to manually mesh the domain by defining the vertices along which the mesh elements would connect.

It's easy to see how this was a tedious, time-consuming and error-prone process, more so since the mesh had to be modified every time the domain geometry changed in the slightest. Current generation software uses meshing algorithms to automatically generate a discrete mesh over the domain. In the case of COMSOL the user may opt to rely entirely on the meshes generated by the program (called a *free mesh*), to impose some rules or constraints on the used mesh (known as a *mapped mesh*) or to use a combination of the two (*e.g.* a mapped mesh over a particular point of interest and a free mesh over the rest of the domain). Either way, after the mesh is generated, the user has the option of designating areas of interest where the mesh needs to be finer. It is worth noting that while the finer the mesh, the more elements (and implicitly vertices) it has, the higher the probability that the solution will converge and the closer the approximation is to the exact solution, one should be mindful not to overextend the calculation so much that the computers resources could not accommodate it. Failure to do so might result in extremely long computation times. Finally, once the program has created a database with the mesh elements, their relations to each other and to the physical geometry of the problem, the preprocessing module applies any existing boundary conditions or initial conditions defined by the user before moving on to the processing module.

The processing step is where the actual computations for providing a solution are performed. As discussed earlier, at each vertex, internal or external, the field variables are evaluated. This yields a set of algebraic equations which are collected in matrix form from the entire domain. These equations are then solved while accounting for any boundary conditions that were defined. When solving the matrix equations the software uses algorithms optimized for various types of problems; for static problems, a method based on Gauss elimination might be used.

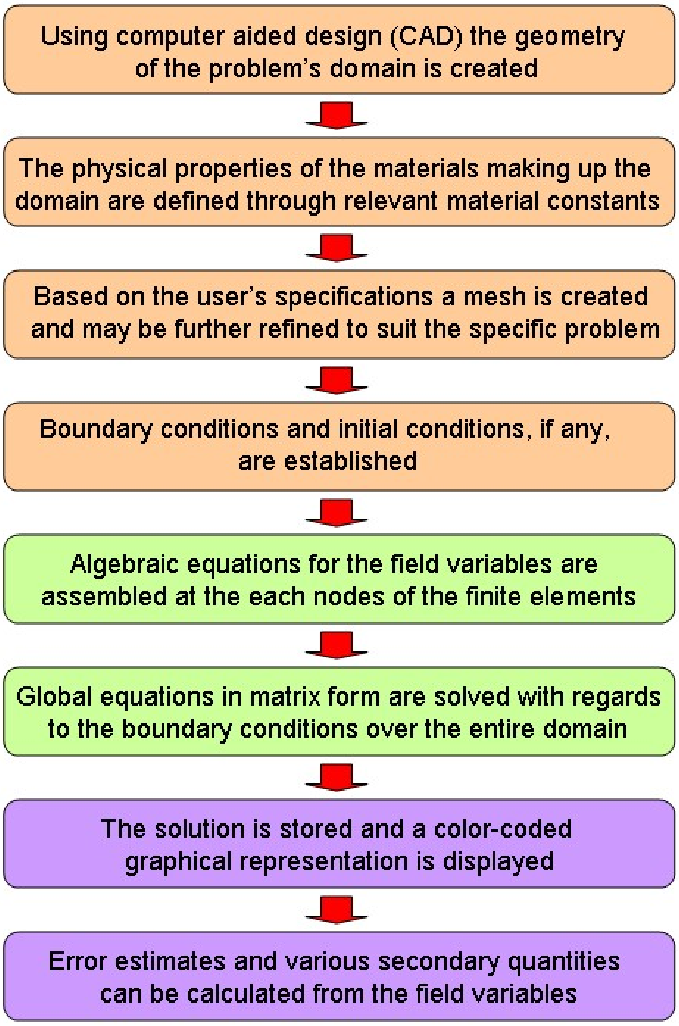
Using computer aided design (CAD) the geometry of the problem's domain is created
The physical properties of the materials making up the domain are defined through relevant material constants
Based on the user's specifications a mesh is created and may be further refined to suit the specific problem
Boundary conditions and initial conditions, if any, are established
Algebraic equations for the field variables are assembled at the each nodes of the finite elements
Global equations in matrix form are solved with regards to the boundary conditions over the entire domain
The solution is stored and a color-coded graphical representation is displayed
Error estimates and various secondary quantities can be calculated from the field variables

Figure 3.3: A schematic representation of the main steps taken by COMSOL during a simulation: the tan boxes pertain to the pre-processing module, the green ones to the solution module and lastly, the purple ones make up the post-processing module

Lastly, the postprocessing step outputs the results of the calculation in a graphical, often color-coded, representation. In case of a time-dependent problem a dynamic, animated representation is available. Often secondary quantities that depend on the field variables are calculated as these may present more practical interest (*e.g.* in structural analysis problems the field variable may be displacement, but the actual quantities of interest are strain and stress that can be derived from displacement).

3.3 Simulation Results

We used COMSOL to model the propagation of LRSPPs through our nanowire waveguides both in a static regime and while subjecting the metal wires to resistive heating by means of an electric current. This research was carried out in collaboration with Petur G. Hermannsson and a more detailed account is given in papers II and III. When investigating the nanowires in the absence of an electric current we modeled the cross section of the waveguide and computed the effective refractive index and the mode field (the spatial distribution of the electric field). As illustrated in the figure below, the waveguide was considered to consist of a gold nanowire with a square cross section embedded in a layer of polymer which is in turn enclosed in a box of air. Since the polymer layer is relatively thick, the silicon substrate can be safely omitted. The goal was to understand how various elements of the waveguide geometry affect the losses along the waveguide and how to minimize these losses. The factors we studied were:

- the effects of deviations of the metal core from square symmetry, such as slightly rectangular or trapezoidal cross sections
- the effect of the presence of an adhesion layer between the gold core and the polymer layer
- the effects of the size and shape of the polymer cladding

Our nanowire waveguides were designed to operate at the free space wavelength of λ=1550nm in order to ensure compatibility with standards used by the telecommunications industry. At this wavelength, Au is characterized by a complex refractive index of $\tilde{n} = 0.52 + 10.7i$ while our chosen polymer, benzocyclobutene (BCB), has a refractive index of $n = 1.535$. As mentioned in the previous chapter, the modes supported by a metallic wire with a square cross-section encased in a dielectric medium, are supermodes resulting from the interaction of the four corner modes. There are two long-range propagating modes that in literature (59) are designated $E^{(0,1)}$ and $E^{(1,0)}$.

There are two types of loss that characterize our nanowire waveguide devices: the *propagation loss* and the *coupling loss.* As the name suggests, the propagation loss is due to the LRSPP traveling along the waveguide and is caused by the absorption of the electromagnetic radiation in the metallic components. The propagation loss is computed from the *effective refractive index.* This is analogous to the refractive index in homogeneous media applied to optical fibers and waveguides; it is a measure of the speed of an electromagnetic wave in the medium relative to the speed in vacuum. Unlike the refractive index for homogeneous media, where the speed of the wave is solely dependent on the wavelength, in a waveguide the speed is dependent both on the wavelength and on the mode in which the light propagates, for this reason the effective refractive index is also called *modal index.* The effective refractive index, n_{eff}, is related to the propagation constant β:

$$\beta = n_{\text{eff}} \frac{2\pi}{\lambda} \tag{3.7}$$

The propagation constant describes how the electromagnetic wave behaves as it propagates in the medium. Note that n_{eff} may be a complex number (it is in our case) with the imaginary part describing the optical loss or gain when it's negative or positive, respectively. The propagation loss, measured in dB/mm, can be determined from the imaginary part of n_{eff}:

$$L_p = \frac{40\pi}{\lambda \ln(10)} Im(n_{\text{eff}}) \tag{3.8}$$

The total propagation loss for a waveguide of length l is $L_{p_{total}} = L_p\, l$. It should be noted that this model considers the metal to be characterized perfectly by its complex refractive index; additional losses due to scattering on surface roughness or defects in the bulk of the metal (grain boundaries, vacancies, etc) are not accounted for by the model. We find in literature that the structure of the metallic plasmonic waveguide (polycrystalline vs. monocrystalline) can have considerable effects on the propagation length of the plasmon in both silver (66) and gold (67) waveguides.

The coupling loss occurs when the surface plasmon is launched along the waveguide. There are several ways of exciting surface plasmons and some were briefly mentioned in the introductory chapter. In order to integrate our nanowire waveguides and the active devices based on them into the existing fiber optics technology, the most advantageous method was to excite the plasmons by *end-fire coupling*: an optical fiber is aligned precisely to the end of the waveguide and the spatial distribution of the electric field in the fiber is closely matched, by design, to the field distribution of the plasmonic modes supported by the nanowire waveguide. We find that this design is more advantageous to our applications than prism or grating coupling, since one of our goals is to minimize the footprint of the device. In case of the end-fire coupling method, the losses that occur when the electromagnetic wave ‘jumps‘ from the optical fiber to the nanowire waveguide are directly related to the overlap between the mode profile in the fiber and that in the waveguide. In order to ensure that no air gap is present, an index-matched oil was used between the input fiber and the waveguide. The overlap O between two 2-dimensional distributions F and G is given by:

$$O = \frac{\left[\int\int F\,G\,dxdy\right]^2}{\int\int F^2\,dxdy\int\int G^2\,dxdy} \tag{3.9}$$

COMSOL's postprocessing module can calculate this overlap if we supply it with the field distribution in the optical fiber. For the single-mode fiber that we use the electric field was approximated by a simple Gaussian distribution characterized by the *mode field diameter*: the distance from the center of the fiber where the intensity has dropped to $1/e^2$ of the center value. These values are supplied by the manufacturer of the optical fiber, but they may also be measured if an appropriate camera is available at the operating wavelength. Once the overlap O is known and assuming that the fiber and the waveguide are perfectly colinear, the coupling loss, expressed in dB is given by the formula:

$$L_c = -10\,\lg O \tag{3.10}$$

Here too, it should be noted that this way of computing the coupling loss considers the end facet of the optical fiber and the side of the nanowire waveguide to be perfectly flat and smooth surfaces. However, the sides of the sample containing the nanowires were not polished after the Si wafer was diced using a dicing saw and saw-marks were visible on the facet under a high magnification optical microscope. These dicing marks even in the presence of the index-matched contact oil introduce additional losses, so the measure coupling loss will always be higher than the theoretical values provided by our model. The quantity by which we evaluate our devices is the *insertion loss*, that is the total losses experienced by an electromagnetic wave coming from the input fiber exciting LRSPPs that travel along the waveguide and are coupled out at the end facet into a pick-up fiber. It is easy to see that the insertion loss of a nanowire waveguide of length l is given by:

$$L_{total} = 2L_c + L_p\,l \tag{3.11}$$

A square cross-section

Let us consider first the effects of the geometry of the metallic core on the propagation and coupling loss. We considered a nanowire with square cross-section and varied the length of the sides between 150nm and 200nm. In order to mimic our experimentally fabricated devices, the polymer cladding had a total thickness of 24 μm with the gold nanowire positioned in the middle. The figure below represents the results of our simulations. The graph only shows the simulations for the $E^{(1,0)}$ mode

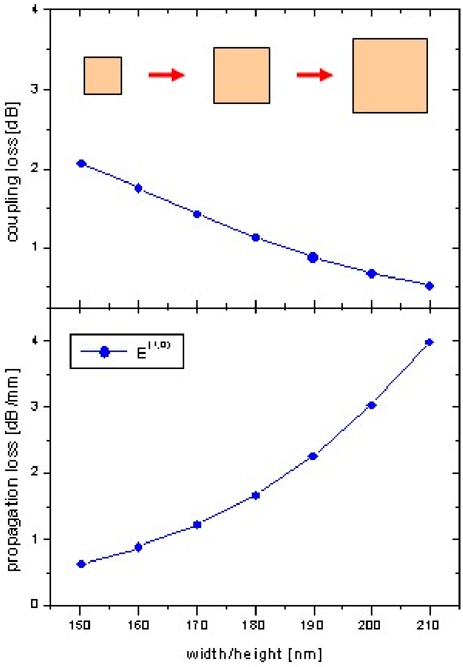

Figure 3.4: The coupling loss and propagation loss simulations when increasing the size of the gold nanowire core while maintaining the square cross-section.

because we found they were no different from the results for the $E^{(0,1)}$ mode. The graph also shows that while the coupling loss decreases as the side of the core's cross-section increases (due to an increased overlap between the supported LRSPP modes and the modes of the fiber), at the same time the propagation loss also increases. This means that minimizing the insertion loss will be a compromise between the coupling loss and propagation loss. The geometry needs to be tailored for he specific application for the device: a relatively short plasmon waveguide might benefit from low coupling loss and cope with higher propagation loss, while a longer waveguide will be aimed at minimizing propagation loss while incurring higher coupling loss.

An asymmetric cross-section

For our active plasmonic devices we aimed for a small footprint, which is one potential advantage over classical dielectric-based attenuator devices. For the overall length of our waveguides we aimed for 0.5 mm to 2 mm, and we chose a cross-section for the gold nanowire of $180 \times 180\,\mathrm{nm}^2$. Next we examined the effects of slight deviations from the square symmetry. Since the gold is deposited through thermal evaporation in a vacuum chamber, we expected fairly uniform height for our wires, however, due to errors or less-than-optimal calibration during the electron beam lithography process, the width of the wires might be slightly more or less than 180 nm. We modeled 180 nm-high nanowires with widths ranging from 160 nm to 200 nm. Similar trends can be observed as with the large and small square cross-sections: the coupling loss decreases as the surface of the cross-section increases and at the same time this leads to higher propagation loss. However, we can also observe that the $E^{(1,0)}$ and $E^{(0,1)}$ modes act differently and even small deviations from a perfect symmetry result in an increase of the propagation loss. The difference in the insertion loss between the $E^{(1,0)}$ and $E^{(0,1)}$ modes is

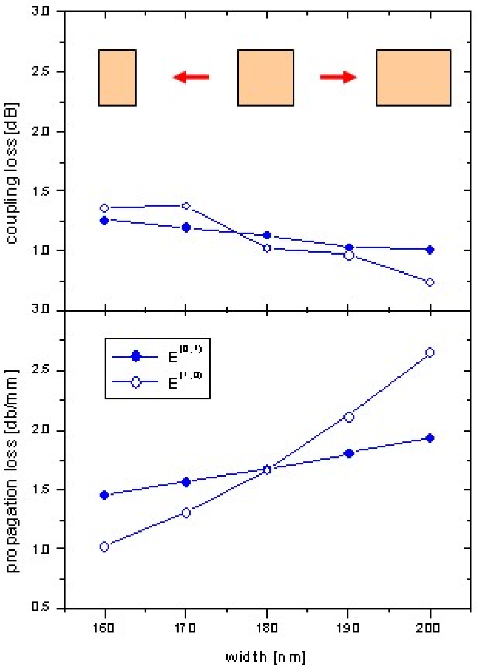

Figure 3.5: Simulations for the coupling loss and propagation loss for nanowires with asymmetric cross-sections. The deviation from a square cross-section causes distinction between the $E^{(1,0)}$ and $E^{(0,1)}$ modes.

known as the *polarization dependent loss* (PDL). The PDL needs to be low, or ideally zero, for a device that operates in an environment without a preferential polarization plane. As we discussed in paper I, for the PDL to be low enough that our plasmonic optical attenuators to perform properly, the deviation from square symmetry must be less than 10nm, for a $180 \times 180\,\mathrm{nm}^2$ wire.

Trapezoidal deviation due to manufacturing

During our early simulations we considered only square or rectangular cross-sections, however we found during manufacturing that some samples presented a slight trapezoidal shape, wider at the base and narrowing narrowing slightly towards the top. We decided to model these trapezoidal-shaped wires in COMSOL to evaluate their effect on the propagation loss of the plasmonic waveguides. The simulations revealed that for small deviations from square to trapeze cross-section, when the trapezoidal angle is less than 5 degrees, there is little change in the propagation loss. However, for larger deviations, the $E^{(1,0)}$ mode shows a strong increase in propagation loss that is not observed for the $E^{(0,1)}$ mode. This suggests that a moderately trapezoidal shape can be a source of PDL and should be avoided; as stated earlier, a close-to-square cross-section fabricated to tight tolerances is necessary for a polarization-

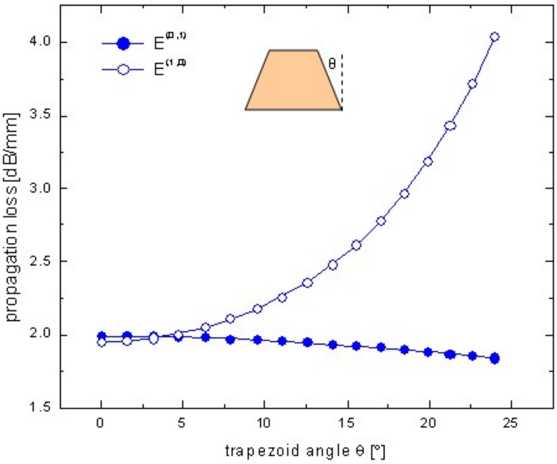

Figure 3.6: Propagation loss simulations for nanowires with trapezoidal cross-sections. The base of the wire is 180nm with the top narrowing down to 100nm at a trapezoidal angle θ=24°

insensitive waveguide.

The effects of an adhesion layer

Our initial models only considered the plasmonic waveguide to be made up of the gold nanowire encased in polymer. During fabrication it became apparent that the gold nanowire has poor adhesion to the surface of the polymer cladding. This would cause the wires to be damaged or completely detach from the polymer during the lift-off process (this is discussed in more detail in chapter 4). A comparatively very thin (2 nm) layer of titanium (Ti) was used in order to improve adhesion to the BCB. The Ti layer was deposited in a vacuum chamber just prior to the Au deposition. We modeled the influence of the Ti adhesion layer on the propagation and coupling loss of nanowires with various square

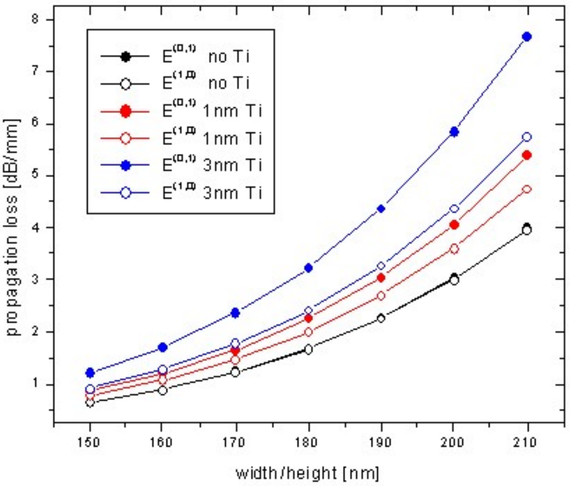

Figure 3.7: Propagation loss simulations for square cross-section nanowires of various sizes in the presence of a Ti adhesion layer of 1 nm and 3 nm

cross-sections, from 150 nm to 210 nm. The simulations revealed that the coupling loss slightly decreases by around 0.2 dB by adding a 1 nm or 2 nm Ti layer. this change affects both the modes equally so no PDL is introduced. However, the propagation loss increases more considerably and, more importantly, the loss is higher for the $E^{(0,1)}$ mode than the $E^{(1,0)}$ mode; the difference between the propagation losses for the two modes also increases with the thickness of the adhesion layer as shown in figure 3.8. The Ti adhesion layer is necessary due to the way the plasmonic waveguides are fabricated; alternatively Cr can be used but the effects are similar. One way of counteracting the PLD introduced by the Ti layer is to use slightly rectangular cross-sections with the width larger than the height. This will balance out the PDL, the trade-off being a slight increase in the total insertion loss.

The polymer cladding

So far we have looked at the how the various geometries of the metallic nanowire core can affect the insertion loss and the polarization-dependent loss. We considered a polymer cladding with a total thickness of 24 μm and a width of 80 μm. We also simulated several cladding thicknesses ranging from 12 μm to 40 μm as well as shrinking the lateral dimension of the cladding from 80 μm to 16 μm. Figure 3.9 presents the insertion loss for three plasmonic waveguides of 0.5 mm, 1 mm and 2 mm length as the height of the surrounding polymer is decreased followed by narrowing the width of the cladding. It should be noted that we didn't include the Si substrate that supports the waveguide in our simulations since it doesn't affect LRSPP propagation as it is separated from the Au core of the waveguide by a thick polymer layer. However, in case of a thin cladding there may be leakage into the Si substrate; a layer of low refractive index polymer might serve as a buffer layer prevent this. As

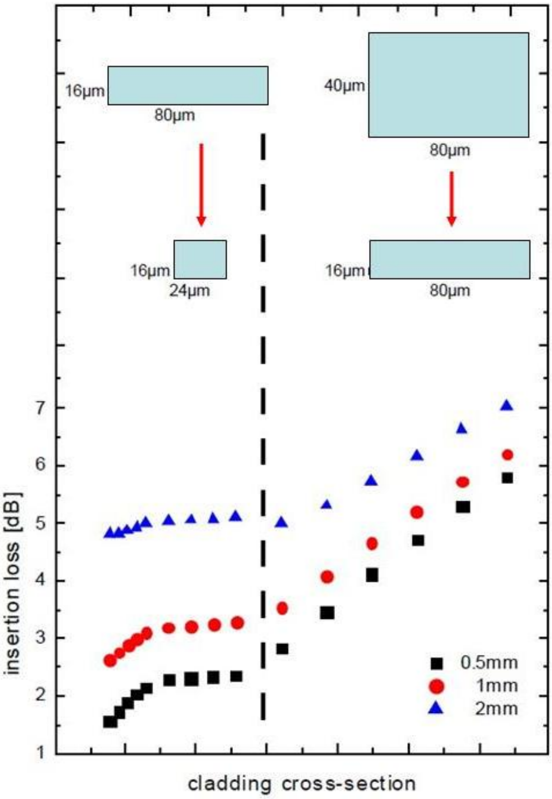

Figure 3.8: Insertion loss simulation for three waveguides of different length when the size of the polymer cladding is decreased

the figure shows, the nanowire insertion loss can be decreased substantially by introducing additional confinement from the dielectric cladding (mainly reducing coupling loss). This has, however, not yet been experimentally demonstrated.

Simulations of heated waveguides

We also conducted simulations of the heating of the waveguide when an electric current is passed through the metallic nanowire (58, p. 38). The Joule heating of the waveguide was modeled by considering the nanowire core as a constant power heat source. We also took into consideration that some material properties are temperature-dependent, such as: heat capacity, thermal conductivity and refractive index. The heat transfer between the air and BCB was modeled by requiring the temperature to be continuous along the air/BCB interface and setting the temperature at the outer edges of the air box at constant room temperature. COMSOL solves the following heat transfer equation:

$$\rho C_p \frac{\partial T}{\partial t} + \nabla\left(-k\nabla T\right) = Q - \rho C_p \mathbf{u}\,\nabla T \tag{3.12}$$

where ρ is the density; C_p the specific heat capacity at constant pressure; T is the temperature; k is the thermal conductivity; Q is the power density of the heat source and $\mathbf{u}$ is the velocity field vector, used to describe the motion of fluids. The polymer BCB was chosen because of its thermo-optic properties. BCB has a negative thermo-optic coefficient, meaning that its refractive index decreases as the temperature increases: $\partial n/\partial T = -2.5 \cdot 10^{-5} K^{-1}$. We have so far discussed the LR-SPP modes propagating at the interface between the Au nanowire and the polymer (more precisely, propagating mostly at the corners of the square nanowire), however the polymer cladding itself supports multiple bound electromagnetic waves since it has a higher refractive index than air. As the temperature is increased, the refractive index of the polymer and consequently the real part of the effective refractive index of the waveguide is lowered; due to the highly localized heating however the refractive index of the cladding changes relatively little. This causes the LRSPPs from the wire to couple out into the cladding where they are lost; this is the mechanism by which the attenuation of the transmitted LRSPP intensity is achieved. The results are more broadly discussed in papers I and III.

4

Sample fabrication

In this chapter we look at the techniques used to fabricate our samples. Our main goal was to create a gold wire with a square cross-section encased in a suitable polymer which featured electrical contact pads to allow the resistive heating of the wire. Such a nanowire waveguide could be used as a compact variable optical attenuator with the magnitude of the electric current controlling the intensity of the transmitted signal. We also produced strip waveguides where, as discussed earlier, the metallic core is a thin strip with the width much larger than the height. We studied the LRSPP propagation through these strip waveguides as well as the degrading of the strips due to electromigration when a current was passed through the strip for a prolonged time period. For a joint project with the Nanophotonics Department of the Laser Zentrum Hannover we fabricated dielectric-loaded SPP waveguides; plasmon propagation through these waveguides was studied through leakage radiation microscopy.

4.1 Strip waveguides

All the fabrication steps were carried out in a cleanroom to avoid contamination of our samples. A cleanroom is a standard environment employed in microelectronics manufacturing, semiconductor industry and research centers where microscopic airborne particles present a contamination hazard to the samples that are being produced. A cleanroom keeps the amount of particles present in check by strictly limiting the sources of contamination and using a constant flow of filtered air to get rid of particles already present. The cleanliness of a cleanroom can be gauged by the amount of particles with a certain size present in a specific volume, *e.g.* a class 1000 cleanroom has no more than 1000 particles of $0.5\,\mu$m diameter per cubic foot (in contrast, the air in an average room contains over one million such particles per cubic foot). The Science Department of the University of Iceland has at its disposal a cleanroom of Class 100-1000 that was used for most of our fabrication steps. For the part of the work carried out at the Danish Technical University, their own cleanroom was used; a class 100 cleanroom. For our presentation we will break down the fabrication process into producing the lower part of the polymer layer, creating the Au strip itself and eventually the top layer of the polymer cladding; each of these parts in turn include several manufacturing steps.

The lower polymer layer

As mentioned in the previous chapter, the polymer used for the cladding needs to have particular optical properties. We chose to use *benzocyclobutene* (BCB), commercially known as Cyclotene 3000 series, available from DOW Chemical Co. BCB has a refractive index $n = 1.535$ at λ=1550nm and a negative thermo-optic coefficient $dn/dT = -2.5 \cdot$

$10^{-5}\,K^{-1}$.

A standard 4″ silicon wafer was used as a substrate. Prior to coating it with BCB, an adhesion promoter was applied. The adhesion promoter recommended by Dow Chemicals is called AP3000 and it was spun on the Si substrate in an open-bowl spin coater. Following this BCB was spun on top of the primed wafer to yield a layer of a desired thickness (for most samples it was $14\,\mu$m). The spin coater is a device used for obtaining thin films of polymers on a flat surface. The target surface placed on a plate that can rotate at high speeds and is held in place usually by the pressure difference caused by a vacuum pump. A precise amount of the chemical dissolved in a solvent at a known concentration is then dispersed on the target surface. The surface is then spun at a constant speed for a given amount of time (most commercial spin coaters are capable of up to 5000 revolutions per minute). The spinning has two effects on the chemical solution: the solution spreads to cover the entire surface while any excess is ejected at the edges and the solvent also evaporates leaving behind a film of the desired polymer. The thickness of the film is controlled by the concentration of the solution and the speed and duration of the rotation. Often it is also necessary to bake the sample in an oven or on a hotplate to evaporate all the solvent and to cure the polymer. Curing is a process by which the polymer strands are cross-linked resulting in a hardening of the polymer and can be achieved by various chemical (additives) or physical (heat, UV radiation) means; the vulcanization of rubber is an example of such a process. Our wafer was baked in an oven to partially cure the BCB layer. The manufacturer recommends a curing temperature of 210°C for 40 minutes. A slow ramping is required for optimum planarization. BCB is susceptible to oxidation at temperatures above 150°C, which needs to be avoided as it changes the optical properties of the polymer. To achieve an inert atmosphere and keep the oxygen concentration below 100ppm there was a constant nitrogen flow in the oven during the curing. This thermal treatment doesn't fully cure the BCB, rather it results in a 75-82% cross-linking and is called *soft curing* or *soft baking*. After the Au strips are deposited and the second layer of BCB is spun on top of it the sample is baked again at a higher temperature to fully cure the polymer, this results in the lower and upper BCB layers integrating seamlessly without an interface between them.

The Au strip

Our aim was to create gold strips that are a few nanometers thick ($8 - 13\,\mathrm{nm}$), several microns wide ($4 - 10\mu\mathrm{m}$) and several millimeters in length. The thickness of the strips, we shall see, is controlled by the actual deposition process. The width and length of the strips is determined prior to the gold deposition by a pattern on top of the BCB layer.

The process most suited for making this pattern is determined by the size of the smallest feature, which in our case is the width. One process that lends itself to making patterns with a minimum feature size on the

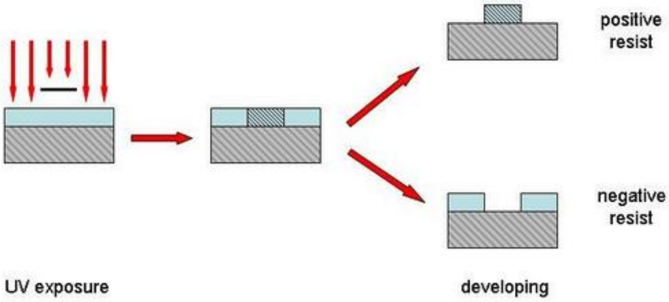

Figure 4.1: Illustration of a negative- and positive-tone photoresist

orders of a few microns is traditional UV lithography. First, a thin film of *negative-tone photoresist* was spin coated on top of the BCB layer. The photoresist, sometimes simply called resist, is a light-sensitive material, in our case sensitive to UV light at 365nm, that becomes soluble in a

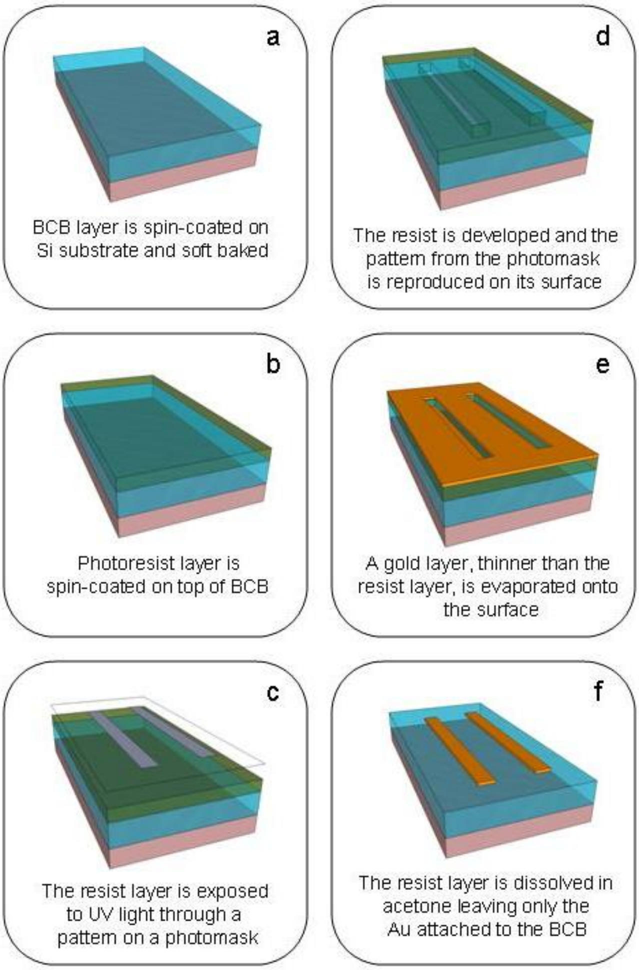
a
BCB layer is spin-coated on Si substrate and soft baked
d
The resist is developed and the pattern from the photomask is reproduced on its surface
b
Photoresist layer is spin-coated on top of BCB
e
A gold layer, thinner than the resist layer, is evaporated onto the surface
c
The resist layer is exposed to UV light through a pattern on a photomask
f
The resist layer is dissolved in acetone leaving only the Au attached to the BCB

Figure 4.2: The main steps of the UV lithography process; the result is a structure of Au pattern on top of a BCB layer, ready for putting on the top layer

specific solvent when exposed to light. In case of negative-tone resists, the regions exposed to the UV light become insoluble and remain standing after immersion in developer fluid, while in the case of positive-tone resists the exposed portions become soluble. (illustrated in figure 4.1)

Following the patterning of the resist surface, the next step was the actual deposition of the Au. This was achieved by means of thermal evaporation in vacuum. The wafer was placed in an upside-down position, with the patterned face downwards, inside a vacuum chamber. A small amount of high-purity Au was placed in a metallic boat that could be heated electrically inside the chamber. The vacuum is necessary to ensure that no other particles are present when the Au is deposited as these would be incorporated in the Au film and contaminate the sample. Once the chamber was pumped down to high vacuum (between 10^{-7} and 10^{-6} mbar), an electric current was passed through the boat containing the Au, causing it to heat up and evaporate onto the surface of the wafer placed right above it. The thickness of the deposited Au layer was monitored using a quartz crystal microbalance, a sensor containing a quartz crystal placed near the deposition target. It operates on the principle that a metallic film of the same thickness is deposited on both the target and the sensor. The resonant frequency of the quartz crystal depends on its mass and can be measured with very high precision. By knowing the surface of the sensor and the type of material that is being deposited, the minute changes in the quartz crystal's mass can be correlated with the thickness of the deposited film. After the gold deposition the chamber was vented and the wafer removed. The last step is called *lift-off* and it serves to remove the residual resist layer, leaving only the Au pattern that is attached directly to the BCB. In our case, an acetone bath was used for the lift-off.

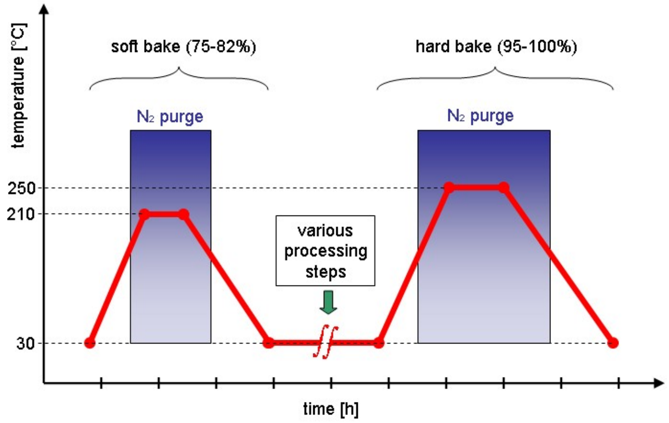

Figure 4.3: A schematic representation of the heat treatment of the polymer layers

The top polymer layer

After the Au strips were deposited on the BCB layer, a second layer of polymer, of the same thickness as the first, was spun on the wafer. Then the final heat treatment in the oven was applied to fully cure the polymer. The oven was purged with nitrogen and the temperature slowly ramped to 250°C (at a rate of 3°C/min) and maintained for one hour. The wafer was then cut using a dicing saw to yield samples of various lengths.

4.2 Nanowire waveguides

For realizing the nanowire waveguides we had to produce Au wires with a symmetric square cross-section with the length of the sides between 150-180nm. With traditional UV lithography techniques a resolution of 150nm cannot be achieved so instead we used electron beam lithography. This technique, as the name implies, uses a focused electron beam to pattern a resist that is is sensitive to electron irradiation. The main fabrication steps were the same as in the case of the strip waveguides: spin on the BCB layer and soft bake, spin on a resist, pattern the resist and develop it, deposit the gold followed by lift-off and a second BCB layer which is then hard baked. However, due to the nature of the e-beam process some additional steps were required.

The resist we used is called ZEP520; it is a high resolution resist which has been shown to allow feature sizes down to 50 nm; another possibility was using poly(methyl methacrylate) (PMMA), another popular resist that has a resolution of roughly 10 nm, either of these two was suitable for our purpose. On top of the e-beam resist a 15 nm-thick Al film was evaporated. The purpose of this Al layer is to prevent charge build-up

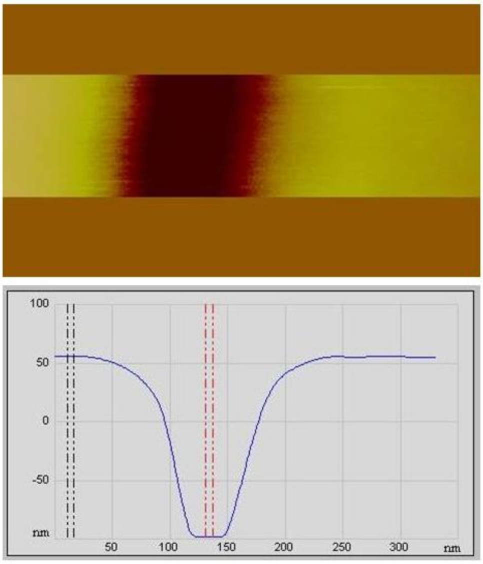

Figure 4.4: AFM image of the e-beam resist after exposure and developing, before the Au layer was evaporated on the surface. The depth of the groove is 150 nm. The sloping sidewalls are an artifact due to the shape of the AFM tip.

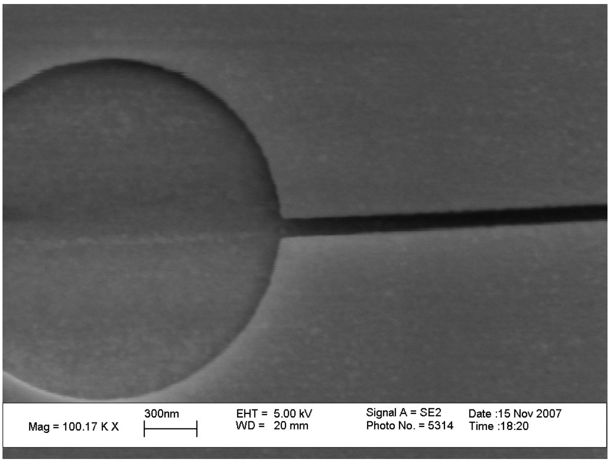

Figure 4.5: SEM image of the e-beam resist before Au deposition. The groove running from the middle of the image to the right is where the nanowire will be located after Au is evaporated.

on the surface during exposure, which in turn could compromise the pattern. The resist was patterned using a JEOL-JBX9300FS electron-beam writer housed in the cleanroom facilities of the Danish Technical University. After the patterning the Al layer was removed by wet etching and the resist was developed using a suitable developer (the commercially available ZED-N50). Before depositing the gold, the patterns were characterized using atomic force microscopy (AFM) and scanning electron microscopy (SEM) techniques. After the resist was developed, a 180 nm layer of gold was deposited by means of e-beam evaporation. A 2 nm-thick layer of Ti was used to enhance adhesion of the gold to the polymer. A low deposition rate of 1 angstrom/s was used. Finally, during the lift-off phase, the remainder of the resist layer was stripped off, leaving us with nanometer-scale Au wires sitting on top of the BCB layer (these were again investigated by means of AFM and SEM).

Before proceeding to spin on the second BCB layer we needed to create contact pads for electrodes to allow us to pass a current through the wires. These contact pads have a relatively large surface, with the sides

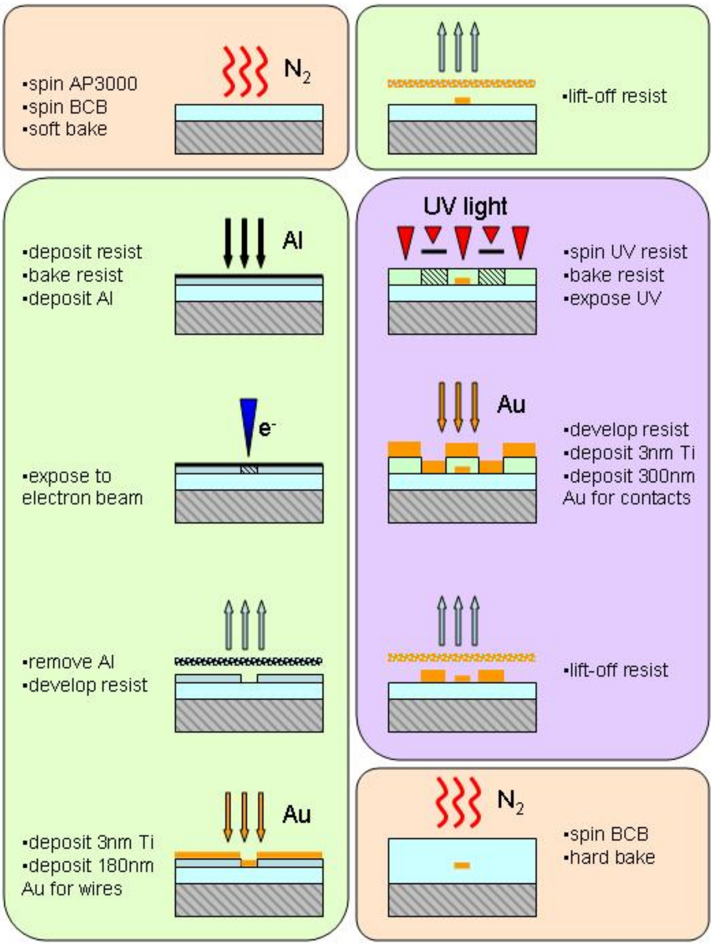
•spin AP3000
•spin BCB
•soft bake
N₂
•lift-off resist
•deposit resist
•bake resist
•deposit Al
Al
UV light
•spin UV resist
•bake resist
•expose UV
e⁻
•expose to electron beam
Au
•develop resist
•deposit 3nm Ti
•deposit 300nm Au for contacts
•remove Al
•develop resist
•lift-off resist
Au
•deposit 3nm Ti
•deposit 180nm Au for wires
N₂
•spin BCB
•hard bake

Figure 4.6: Some of the major steps in the nanowire waveguide fabrication process. The orange boxes mark processes which involve the polymer cladding; the green ones concern the fabrication of the Au nanowire and the purple one the Au contact pads necessary for running a current through the wire.

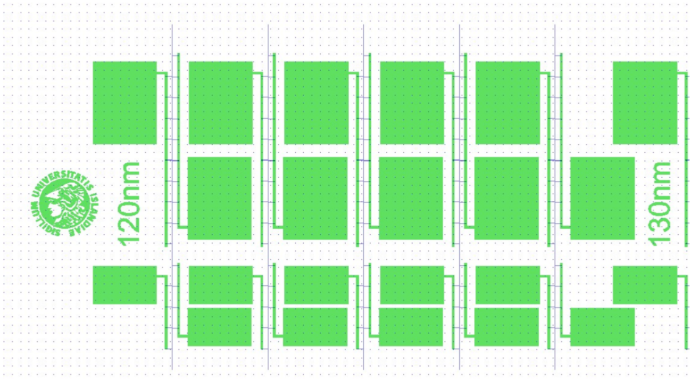

Figure 4.7: A mask design of the actual pattern used for our nanowire waveguide samples. The blue central wires are patterned with e-beam lithography and the green part are patterned with UV lithography (alignment marks (not shown) were used to ensure a good fit).

of around 0.5 mm, so it would not have been economical to use e-beam lithography for patterning them. Instead UV lithography was used: a resist layer was deposited on top of the existing nanowires, then a photomask containing the pattern for the contact pads was carefully aligned with the nanowires and the wafer was exposed to UV radiation. After

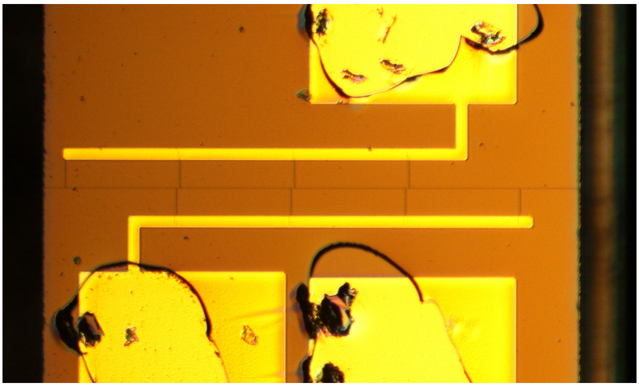

Figure 4.8: A picture of a finished sample; the areas where the BCB was removed to expose the contact pads are visible.

developing, 50nm of Au were evaporated onto the surface in a vacuum chamber, followed by lift-off. It should be noted that the actual design, as shown in figures 4.8 and 4.9, uses multiple, independent heated sections connected to common electrodes to achieve a higher yield fabrication process as breaks were common in the wires.

Lastly, the top BCB layer was spun on and the polymer was hard cured. The wafer was cut to appropriate length using a dicing saw and the BCB above the contact pads was removed manually using a scalpel to expose the pads.

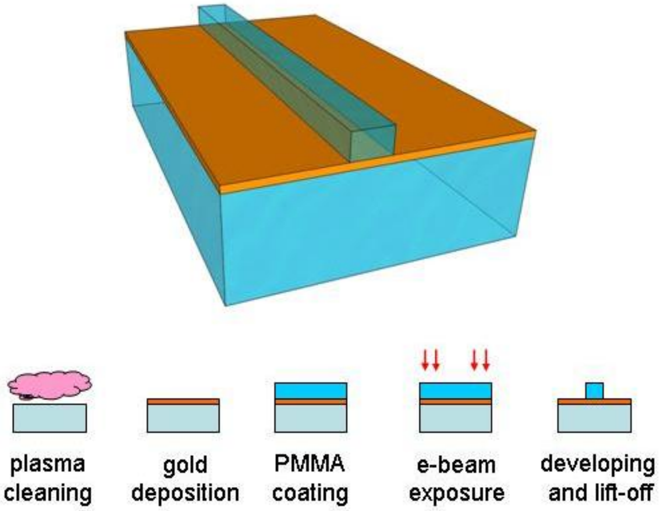
plasma cleaning
gold deposition
PMMA coating
e-beam exposure
developing and lift-off

Figure 4.9: An illustration of a DLSPPW and the main fabrication steps involved in its creation.

4.3 Dielectric-loaded waveguides

We fabricated dielectric-loaded surface plasmon polariton waveguides (DLSPPW) as part of a joint project with the group of Dr. Carsten Reinhardt from Laser Zentrum Hannover. The project was funded by COST (European Cooperation in Science and Technology) and entailed the fabrication of DLSPPWs using e-beam lithography. The quality of these samples was to be compared to similar samples produced through two-photon polymerization by direct laser writing (68). The plasmon propagation through the waveguides was then studied by leakage radiation microscopy.

The DLSPPWs consist of a dielectric substrate covered by a Au film that is several tens of nanometers thick. On top of the Au film dielectric strips are placed which act a a top layer for the structure; it is along these strips that the waveguiding takes place (69). Ordinary microscope cover glass slides were used as a substrate. The surface of the glass was

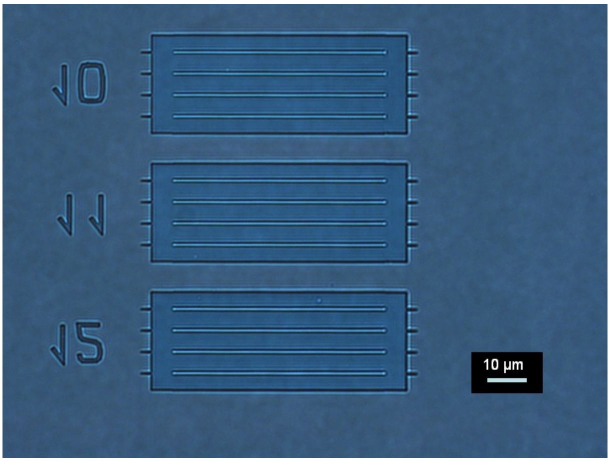

Figure 4.10: Microscope image of a DLSPPW sample; a 50x objective was used to capture this image.

cleaned using Ar plasma and a 50nm Au film was evaporated on the glass in a vacuum chamber. Following the gold film, a layer of PMMA was spin-coated to serve as an e-beam resist material. Using an e-beam writer, 50-micron-long lines of various widths (from 100nm to 500nm) were patterned in the PMMA.

5

Experimental results

In this chapter we briefly present the measurements that were performed on our plasmon waveguides. We first discuss the strip waveguides that we fabricated for the purpose of testing our experimental set-up before proceeding to study the nanowire waveguides. We measured the insertion loss of several strip waveguides of various cross-section sizes as well as the degradation of the Au core due to electromigration when a constant current is applied for extended periods of time. For the nanowire waveguides we characterized the shape and size of the mode field upon decoupling by using an infrared camera operating at λ=1550 nm. Then, fiber-to-fiber insertion loss and polarization-dependent loss measurements were conducted both in the presence and absence of an electric current heating the Au nanowire. Lastly, plasmon propagation in the DLSPPW was studied by leakage radiation microscopy at Laser Zentrum Hannover. More details about experimental results are given in papers I, III and IV.

5.1 Strip waveguide measurements

Insertion loss

In order to work out the propagation loss of the specific strip waveguide geometries, we used the *cutback method*, a widely used technique for characterizing waveguide loss. The method involves measuring the total loss of a length of waveguide, then substituting it with a shorter waveguide (or alternatively just cutting part of the waveguide away). By measuring the loss for several different waveguide lengths, a plot can be made of insertion loss as a function of length; the slope of a linear fit to these points gives the propagation loss and the line's extrapolation at zero length (where it intersects the y-axis) yields the sum of the coupling loss at the input and output facets.

One advantage that both strip and nanowire waveguides have is that the LRSPPs propagating along them can be efficiently excited through the end-fire method. Many SPP geometries require prisms (in Kretschmann or Otto configuration), gratings or various defects to excite surface plasmons and these may be difficult to integrate into existing fiber optic technology. As discussed in the COMSOL modeling chapter, end-fire coupling is possible because the mode field of the LRSPPs is similar to the mode propagating inside a fiber. Minimal coupling loss is also ensured by careful alignment of the fiber to yield a good overlap of the two modes and the loss can further be decreased by using an index-matched contact oil between the waveguide and the fiber and by polishing the waveguide facet to eliminate surface roughness.

We used a free space wavelengths of 1450-1650 nm to excite the LRSPPs in the strip waveguides. We have seen earlier that the strip waveguides support predominantly TM polarized waves so a polarization-maintaining fiber (PM) was used at the input facet. A PM fiber doesn't have a radial

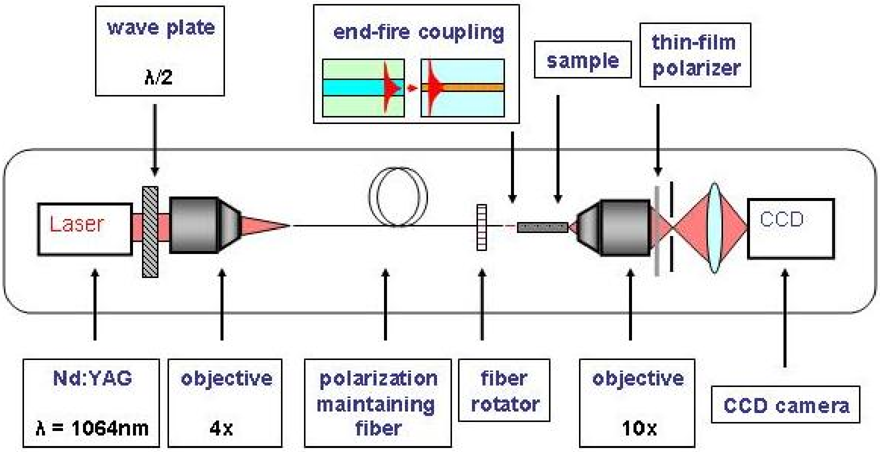
wave plate
λ/2
end-fire coupling
sample
thin-film polarizer
Laser
CCD
Nd:YAG
λ = 1064nm
objective
4x
polarization maintaining fiber
fiber rotator
objective
10x
CCD camera

Figure 5.1: An example of an experimental set-up for imaging plasmon mode fields and measuring insertion loss; for the insertion loss measurements the CCD camera and the focusing lens are replaced with a photodetector

symmetry, but instead it provides a preferential direction for the orientation of a linearly polarized wave. When polarized light is launched along the fiber in the correct orientation, the polarization will be maintained throughout the propagation in the fiber. A 4x magnification microscope objective was used to focus the laser onto the PM fiber with a *half-wave plate* in front of the objective to ensure launching in the correct polarization. A half-wave plate is used to rotate the polarization of an already linearly polarized wave by physically turning the wave plate around its axis. At the opposite end of the waveguides another microscope objective (10× or 100× magnification) was used to pick up the light as it exits from the waveguide. A thin-film polarizer was used to discriminate between polarization directions. Depending on the purpose of the set-up, a CCD camera with an additional focusing lens can be placed behind the second objective (when one is interested in the shape and size of the plasmon mode) or an appropriate photodetector when measuring the transmitted power. While photodetectors in the telecom range are readily available, it should be noted that there are few commercial manufacturers of cameras that operate around λ=1550 nm.

In figure 5.2 we present the results of typical cutback measurements performed on 5-micron-wide Au strips of various thicknesses (7 nm, 10 nm and 13 nm). The length of the waveguides we used were: 2 mm, 5 mm, 10 mm, 15 mm and 20 mm. The slopes of the dotted lines are the propagation loss values for the three types of waveguides. We also compared the propagation losses measured for these waveguides with the theoretical propagation loss in an infinitely-wide double interface BCB/Au/BCB at λ=1064 nm calculated using a 1-D mode solver (the loss was derived from the effective refractive index). At small values of the metallic layer thickness the theoretically predicted values are lower than the measured

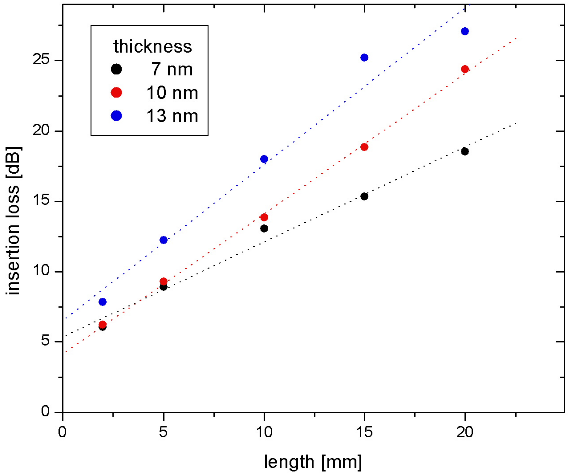

Figure 5.2: Insertion loss results for 5-micron-wide Au strips at 1064 nm wavelength

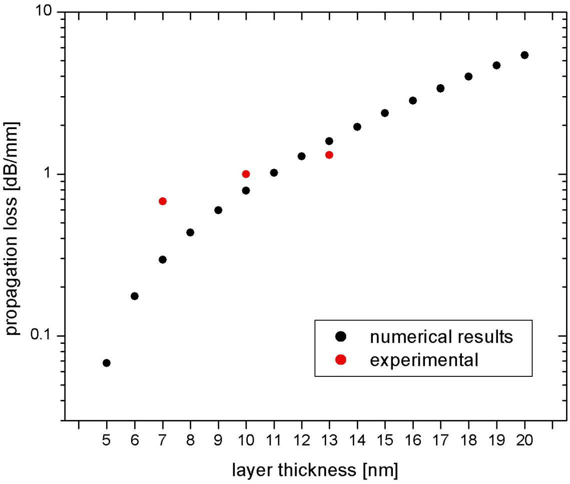

Figure 5.3: Propagation loss measurements for strip waveguides compared to theoretical results for an infinitely-wide double interface

ones; this is possibly due to additional losses because of scattering on surface roughness as opposed to a theoretical, perfectly smooth interface.

Elelctromigration measurements

Since our main objective was to manufacture VOAs based on nanowire LRSPP waveguides that could compete with existing dielectric-based technologies, we also wanted to study the reliability and rate of failure of the devices when operated over long time intervals. We decided to study the failure of strip waveguides due to *electromigration.* Electromigration is the phenomenon of dislocation and transport of metallic ions inside a conductor due to momentum transfer from electron impacts. The electromigration effect has been known to occur for over a hundred years, however it was largely ignored due to not having a significant effect in bulk wires where the current densities are limited by Joule heating. The effect became an engineering problem with the widespread use of microelectronics and integrated circuitry (IC). The wires used in IC have cross-section in the micrometer range and high current densities are achievable because of effective heatsinks. While the flux of displaced ions is proportional to the current density j, it was found experimentally (70), mostly through the work of Jim Black at Motorola, that the mean time to failure from a batch of identical samples varies with the square of the current density:

$$t = Aj^{-2} \exp \frac{E_a}{k_B T} \tag{5.1}$$

where A is a constant, E_a is an activation energy for failure, k_B is the Boltzmann constant and T, which in our case is a funtion of j, is the absolute temperature. Electromigration occurs more often around defects and grain boundaries where the ions have better mobility.

We fabricated strip waveguide samples with electrical contact pads similar to the ones used for the VOAs; strip waveguides were chosen because they were more readily available as no e-beam lithography was involved. The 4-wire method was used for sensing, which involves 4 thin, metallic probes in contact with the pads, two of which supply a constant current while the other pair measures the voltage. The current source was interfaced with a computer using a Labview environment and the measurement process was automated because of the timescale of the experiment (the time to failure of the waveguides varied from just under a minute to several days, depending on the width of the strip and the current). No LRSPPs were excited in the waveguides and the failure was solely due to the electrical current in the strips.

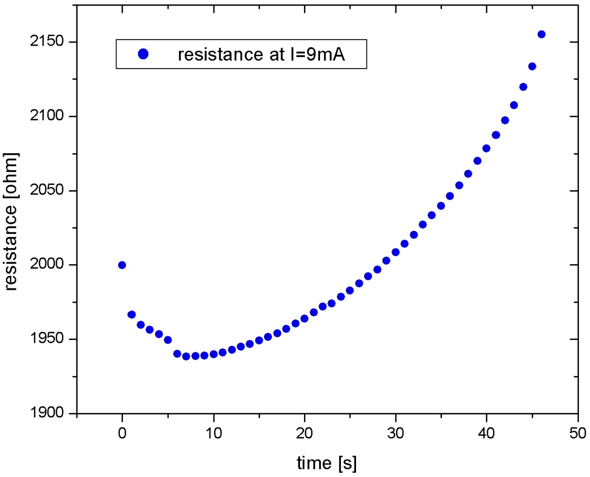

Figure 5.4: Resistance measurements over time with a constant current applied to the strip waveguide

In the above figure, the resistance as a function of time was plotted when a constant current of 9 mA was applied to a 4-micron-wide strip. It is interesting to note that when the strip is connected its resistance decreases slightly at first. Many of the strips displayed similar behavior; this might possible be caused by some additional annealing happening as the wire is suddenly heated.

When passing a constant current between 4-5 mA through our 4- and 6-micron-wide and 13 nm-thick gold strips, they did not fail for more than 40 hours, at which point the measurements were stopped. Once electrical currents around 8mA were applied the gold strips ruptured after a few hours or several minutes as illustrated in figure 5.5.

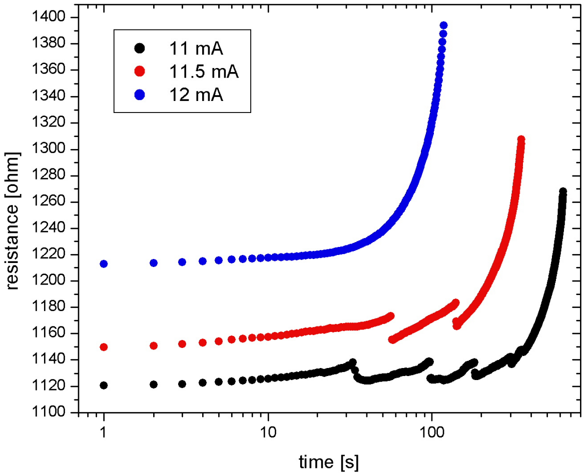

Figure 5.5: Constant current of different values applied to identical Au strips 6-micron-wide and 13 nm-thick

5.2 Nanowire waveguides

Insertion loss measurements and mode profile imaging

For measuring the insertion loss of the gold nanowire-based waveguides, a similar set-up was used as for the strip waveguides (illustrated in figure 5.1). We performed measurements on waveguides with gold wire cores with a nominal square cross-section of 100×100 nm and 180×180 nm, excited by a fiber-coupled laser with a free space wavelength of λ=1064 nm and λ=1550 nm respectively. In this paragraph we present the results for the measurements performed at λ=1064 nm; the nanowires with the larger cross-section were used in our current-driven optical attenuator and are discussed in more detail in the attached paper I.

Just like in the case of the strip waveguides presented previously, for exciting the LRSPPs in the waveguide, the end-fire method was used:

a laser of the appropriate wavelength (in this case a Nd:YAG laser for λ=1064 nm) was focused onto the end of a suitable polarization-maintaining fiber whose other end was then aligned with the end-facet of the individual nanowire waveguide sample. A three-axis translation stage was used to easily achieve precise alignment of the optical fiber the the plasmon waveguide. The output facet of the waveguide was imaged using a microscope objective and projected unto a calibrated photodetector. By measuring the output of the bare fiber (before coupling into the waveguide) and the output of the waveguide we could compute the losses. As previously, in the case of the strip waveguides, the cutback technique was used to derive the propagation and coupling loss (see figure 5.6).

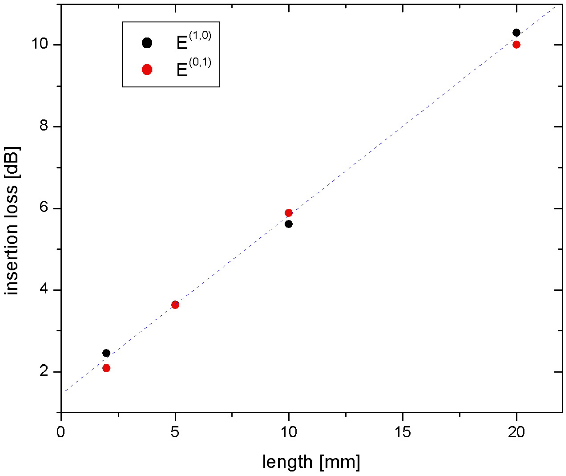

Figure 5.6: Insertion loss measurements in 100×100 nm nanowire waveguides at λ=1064 nm. Samples of 2-, 5-, 10- and 20 mm length were measured. As predicted by theory, the waveguides behave similarly for both TE and TM input polarizations.

No significant difference in transmission was found when TE and TM polarizations were applied at the input facet (achieved by physically rotating the input fiber 90^o). This is in accordance with previous results found in literature (71) and our own simulations: the waveguides base on metallic nanowire cores with a square cross-section support equally the $E^{(1,0)}$ and $E^{(0,1)}$ plasmon modes. The propagation loss for both polarizations in this particular case was measured to be 0.43 dB/mm and the coupling loss from the fiber to the waveguide was 1.5 dB.

We also observed a decrease in transmission at high input powers. This phenomenon is illustrated in figure 5.7, where the transmitted power is plotted as a function of variable input power through a 5 mm-long

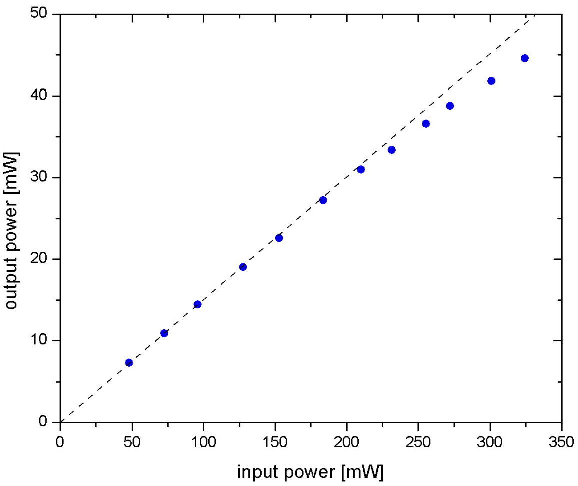

Figure 5.7: Transmission through a 5 mm-long nanowire waveguide at variable input power levels. At high power additional attenuation is observed due to heating of the waveguide core through absorption which in turn leads to heating of the polymer cladding and a change in its refractive index.

waveguide. At 350 mW input power a measurable attenuation (roughly 0.5 dB) is observed. We believe this is due to heating of the metallic nanowire through absorption; which implicitly leads to heating of the polymer cladding adjacent to the core, lowering its refractive index, thus reducing transmission. This is the same effect that we are looking to achieve in our optical attenuators, with the difference that in this case the heating of the metallic wire core is achieved by passing an electric current through it.

In order to image the profile of the plasmon mode as it couples out from the waveguide a 100× magnification microscope objective was used at the output facet; the microscope objective projected the image onto a CCD camera suitable for the used wavelength. Figure 5.8 shows a typical image recorded by the camera. The parallel lines across the profile are caused by dicing marks from the saw used to cut the sample from the 4-inch Si wafer.

From the images we can work out the mode field diameter of the plasmon mode to be roughly 20 μm. Figure 5.9 shows some profiles for an $E^{1,0}$ mode in waveguides of different lengths. We can observe that the mode

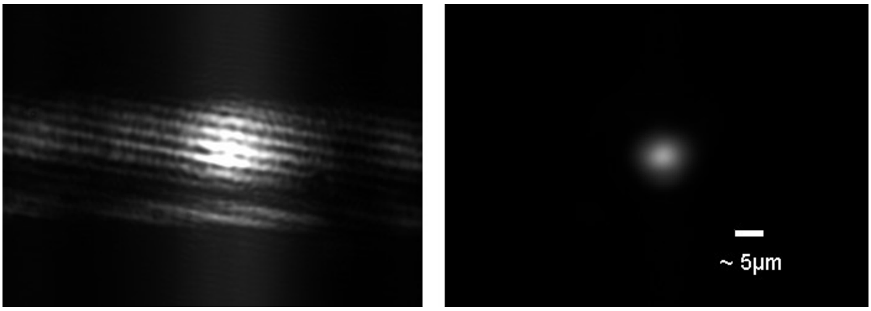

Figure 5.8: Waveguide mode image recorded with a CCD camera. On the right side the spot size of the laser out of the bare fiber is given as reference; the nominal mode field diameter is 5.4 μm

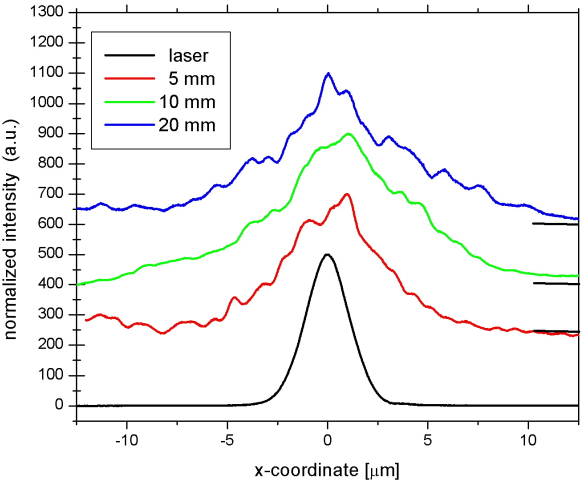

Figure 5.9: Mode profiles for $E^{1,0}$ plasmon propagating through waveguides of various lengths.

profiles do not change drastically as the LRSPP propagates through the waveguide. While not pictured here, both $E^{0,1}$ and $E^{0,1}$ modes look similar, as it is to be expected.

Polarization-dependent loss measurements

As we have stated earlier, one of the goals we wanted to achieve with our active LRSPP-based device was easy interfacing with existing fiber communications technology. We chose a gold core with a square cross-section because such a symmetry would make our device largely insensitive to the polarization of the light coupled from the input fiber. We performed polarization dependent loss (PDL) measurements on the waveguides; PDL is defined as the maximum variation in insertion loss when light in all possible polarization states is passed through the device.

A polarization analyzer was used to perform two type of PDL measurements, employing the machine's internal polarizers as well as an external polarization controller (the two methods are briefly illustrated in figure 5.10). The light source was a tunable laser operating at λ=1550 nm and optical fibers were used both to couple light into the sample and to pick up the light at the output facet (note that these fibers were not polarization-maintaining, but standard single-mode fibers). All the fibers were securely taped to the optical bench in order to avoid changes

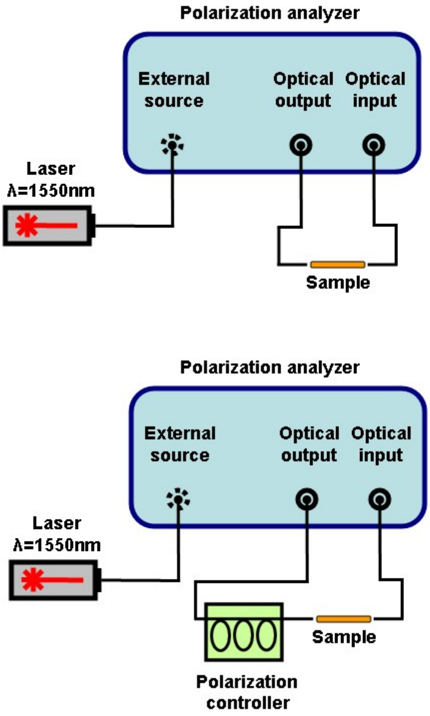
Polarization analyzer
External source
Optical output
Optical input
Laser
λ=1550nm
Sample
Polarization analyzer
External source
Optical output
Optical input
Laser
λ=1550nm
Sample
Polarization controller

Figure 5.10: Schematic representation of two polarization-dependent loss measurement techniques: the *Jones Matrix method* (top) and the *power min-max method* (bottom).

in polarization due to bending during the measurements. Prior to the measurements the polarization analyzer is calibrated by connecting its *input* and *output* ports with a short length of fiber. The so-called *Jones Matrix method* is largely automated. After the sample is connected to the *input* and *output* ports via optical fibers the analyzer's internal polarizers generate three linear polarization states, typically at 0°, 60° and 120°; it measures the transmitted power in these three states and computes the PDL from these values. Our sample contained waveguides with a nominal 180×180 nm Au core as well as deviations in width both ways from 150 nm to 210 nm; the results are contained in figure 5.11.

The second method we used is known as the *power min-max* method and it involves using an external polarization controller to generate many polarization states (the 'wiring diagram' is presented in figure 5.10). We utilized a manual polarization controller which consists of three consecutive optical fiber loops that can be rotated independently to generate, due to stress-induced birefringence, any polarization state. The polarization analyzer constantly measures the power transmitted through the sample while various random polarization states are generated across the entire Poincare sphere; then the PDL can be computed from the minimum and maximum transmitted power as well as the angle between the two polarization states to which these correspond.

Both methods yielded similar results with a PDL of around 6 dB for the 180×180 nm wires and increasing significantly for wires with an asymmetrical cross-section (by as much as 1 dB for a 5% variation in width). The angle between the minimum and maximum transmission states was measured to be $\theta \approx 170°$, diametrically opposite on the Poincare sphere which creespond to the horizontal and vertical linear polarizations (the $E^{(0,1)}$ and $E^{(1,0)}$ modes). We believe the 6 dB PDL, which is related to fabrication issues. PDL below 1 dB was measured in some of the devices

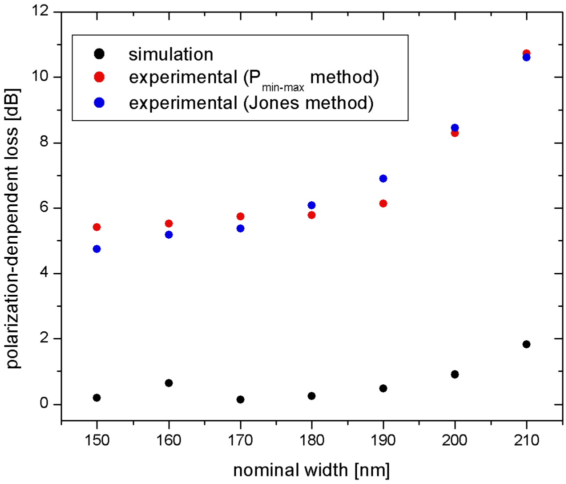

Figure 5.11: Polarization-dependent loss measurements and theoretical estimates for 2 mm-long nanowire waveguides of various widths. The nominal thickness of the wires is 180 nm, yielding a symmetrical cross-section for 180 nm width.

presented in papers I and III.

Current-driven optical attenuator

In this paragraph we introduce very briefly the propagation loss measurements performed on the plasmon waveguides while an electric current was passed through the metallic cores. This topic is the subject of the attached paper I and is just briefly mentioned here.

The waveguides were tested at wavelengths between 1525 nm and 1625 nm. As found in literature, passing an electric current through the metallic wire at the core of the waveguide will cause a rise in temperature in the nanowire, through resistive heating, and the polymer cladding near

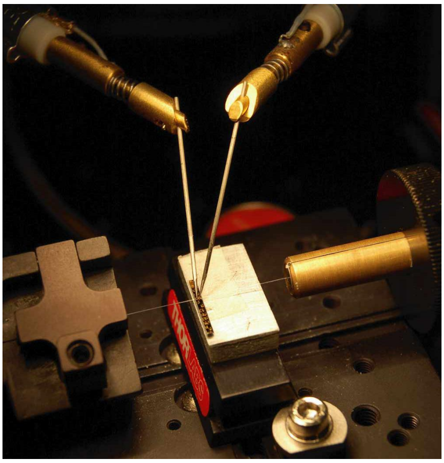

Figure 5.12: Photograph of a 1 mm-long sample during the VOA measurements. The input and output optical fibers are visible as well as the two metallic probes that provide the current through the waveguide core.

it, leading to a decrease in the polymer's refractive index and implicitly greater propagation loss, until transmission is entirely extinguished at higher voltages (no more than 3 V were needed for over 40 dB attenuation). The switching time was several hundred microseconds for heating and around 1 millisecond for cooling. The minimum insertion loss measured was 5 dB (for 1 mm-long waveguides), but we believe this could be further reduced by improving the quality of the metal nanowire or reducing the length of the waveguide while still allowing for sufficient attenuation.

5.3 Dielectric-loaded waveguides

As mentioned in chapter 4, dielectric-loaded surface plasmon-polariton waveguides (DLSPPW) have been fabricated with the intent of characterizing plasmon propagation through leakage radiation microscopy. The work was carried out in collaboration with Dr. Reinhardt's group in Hannover, Germany. This group has been manufacturing DLSPPWs using two-photon polymerization by direct laser writing (72) as well as experimenting with fabrication via nanoimprint lithography (73). One of the goals was to compare these structures to the ones fabricated by e-beam writing by our group.

A set-up was constructed to carry out leakage radiation measurements using a laser at λ=1550 nm as a light source. Leakage radiation microscopy is a far-field technique that allows us to observe the propagation of SPP at an interface on top of a transparent substrate. When SPPs

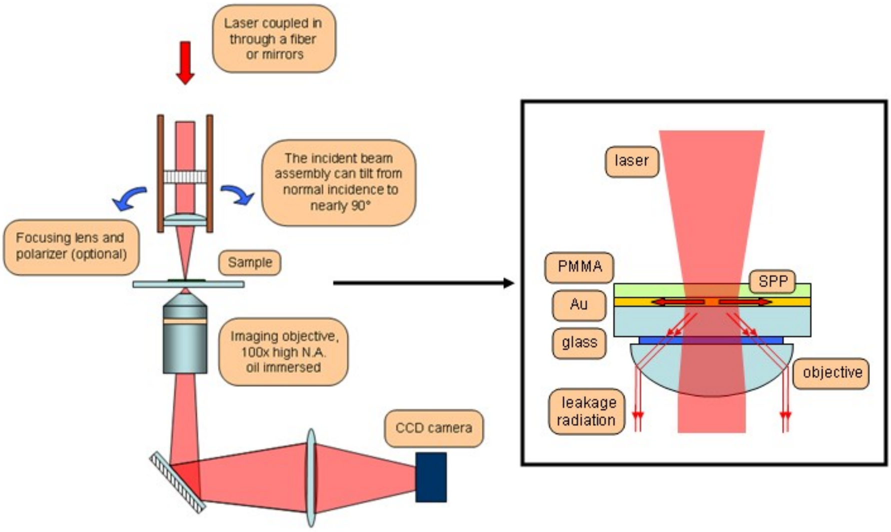
Laser coupled in through a fiber or mirrors
The incident beam assembly can tilt from normal incidence to nearly 90°
Focusing lens and polarizer (optional)
Sample
Imaging objective, 100x high N.A. oil immersed
CCD camera
laser
PMMA
SPP
Au
glass
objective
leakage radiation

Figure 5.13: Schematic illustration of the leakage radiation microscopy set-up and working principle.

propagate along the top interface of a dielectric/metal/air or asymmetric dielectric/metal/dielectric sandwich, radiation can leak into the dielectric provided that the metal is sufficiently thin. This causes additional propagation loss beside loss due to absorption in the metal, but, if the substrate is transparent to that specific wavelength, it allows us to monitor the plasmon propagation. Figure 5.13 illustrates the experimental set-up.

A microscope objective focuses the excitation beam, provided by an optical fiber, on the end of a waveguide (see figure 4.11 for an image of the actual waveguides). Surface roughness allows for the light to excite plas-

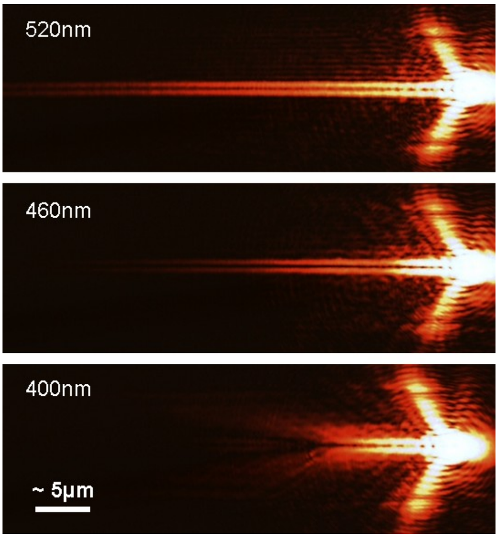

Figure 5.14: Leakage radiation microscope images of SPPs propagating along straight waveguides of different widths. It is clear that the waveguide geometry greatly influenced the propagation length (the widths of the waveguides are marked on each image). The bright spot on the right side of each image is the end of the waveguide where the laser was focused; the wavelength we used was λ=633 nm

mons that propagate along the waveguide; leakage radiation is emitted in a cone through the glass slide that serves as a substrate and is collected using a microscope objective with high numerical aperture. The image from this imaging objective (pictured as upside-down in figure 5.13) is directed onto a suitable CCD camera.

The top part of the set-up, responsible for focusing the laser onto the sample, can be tilted to allow excitation under different incidences. From the images taken through the microscope the intensity of the leakage radiation is measured along the waveguide, closely linked to the plasmon intensity, and the propagation loss for the plasmon mode can be derived (figure 5.14 shows a typical image taken through the microscope). The set-up also allows us to image the Fourier plane and compute the real part of the waveguide's effective refractive index. Article IV attached to this thesis details the results of the study; DLSPPWs fabricated by two-photon polymerization and nanoimprint lithography were used in this case.

6

Conclusions

In this thesis we reported the design, fabrication and characterization of plasmonic strip and nanowire waveguides and a plasmon-based variable optical attenuator at telecom wavelength working on the thermo-optic effect. The VOA device consists of a gold nanowire core with square cross-section (nominally 180×180 nm) embedded in a polymer with negative thermo-optic coefficient. The finite element method was used to model the long-range surface plasmon polariton modes supported by the structure and the geometry was optimized for minimizing coupling and propagation loss. The manufacturing steps were performed in a cleanroom and UV lithography, electron beam patterning and thermal deposition in vacuum were employed. Fiber-to-fiber measurements were carried out to assess the insertion loss and the mode profile was imaged using a digital camera working at λ=1550 nm. We achieved extinction ratios in excess of 20 dB for a 1 mm-long sample with switching times between 500-1000 μs. The insertion loss of the waveguide was around 5 dB. Future endeavors may include further decreasing the insertion loss by improving the quality of the metal wire to lower plasmon scattering on structural defects or by reducing the length of the waveguides to 400 μm or even less, however the latter option would also decrease the maximum achievable attenuation. Passing an electric current through the waveguide for long periods of time may result in device failure due to electromigration: mass transport through the metallic core in the direction of the electron flow causes a thinning of the wire cross-section, which in turn accelerates the process due to increased current density. We measured the mean time to failure of several geometries of Au strip waveguides for various drive current values. We also fabricated dielectric-loaded surface plasmon polariton waveguides (DLSPPW) for use at λ=1550 nm. Plasmon propagation through these waveguides was investigated using leakage radiation microscopy.

References

[1] S. A. Maier. *Plasmonics - Fundamentals and Applications.* Springer, 1st edition, 2007. 1, 3, 7, 9, 11

[2] N. W. Ashcroft and N. D. Mermin. *Solid State Physics.* Thomson Learning Inc., 1st edition, 1976. 1

[3] J. Homola, S. S. Yee, and G. Gauglitz. Surface plasmon resonance sensors: review. *Sensors and Actuators B*, 54, 1999. 1

[4] J. Homola. Surface plasmon resonance sensors for detection of chemical and biological species. *Chemical Reviews*, 108, 2008. 1

[5] S. J. Lee, Z. Guan, H. Xu, and M. Moskovits. Surface-enhanced raman spectroscopy and nanogeometry: The plasmonic origin of sers. *Journal of Physical Chemistry*, 111, 2007. 1

[6] S. Nie and S. R. Emory. Probing single molecules and single nanoparticles by surface-enhanced raman scattering. *Science*, 275, 1997. 1

[7] P. Berini. Bulk and surface sensitivities of surface plasmon waveguides. *Sensors and Actuators B*, 54, 1999. 1

[8] R. Charbonneau, M. Tencer, N. Lahoud, and P. Berini. Demonstration of surface sensing using long-range surface plasmon waveguides on silica. *Sensors and Actuators B*, 134, 2008. 1

[9] Y. H. Joo, S. H. Song, and R. Magnusson. Long-range surface plasmon-polariton waveguide sensors with a bragg grating in the asymmetric double-electrode structure. *Optics Express*, 17, 2009. 1

[10] S. A. Maier. Plasmonics Ű towards subwavelength optical devices. *Current Nanoscience*, 1, 2005. 2

[11] W.L. Barnes, A. Dereux, and T. W. Ebbesen. Surface plasmon subwavelength optics. *Nature*, 424, 2003. 2

[12] I. R. Girling, N. A. Cade, P. V. Kolinsky, G. H. Cross, and I. R. Peterson. Surface plasmon enhanced shg from a hemicyanine monolayer. *Journal of Physics D: Applied Physics*, 19, 1986. 2

[13] H. J. Lezec, A. Degiron, E. Devaux, R. A. Linke, L. Martin-Moreno, F. J. Garcia-Vidal, and T. W. Ebbesen. Beaming light from a subwavelength aperture. *Science*, 297, 2002. 2

[14] H. Raether. *Surface Plasmons on Smooth and Rough Surfaces and on Gratings*. Springer-Verlag, 1st edition, 1988. 2, 9

[15] J. J. Burke, G. I. Stegeman, and T. Tamir. Surface-polariton-like waves guided by thin, lossy metal films. *Physical Review B*, 33, 1986. 2

[16] P. Berini. Figures of merit for surface plasmon waveguides. *Optics Express*, 14, 2006. 3

[17] P. Berini. Plasmon-polariton modes guided by a metal film of finite width. *Optics Letters*, 24, 1999. 4

[18] R. Charbonneau and P. Berini. Experimental observation of plasmonŰpolariton waves supported by a thin metal film of finite width. *Optics Letters*, 25, 2000. 4

[19] P. Berini. Plasmon-polariton modes guided by a metal film of finite width bounded by different dielectrics. *Optics Express*, 7, 2000. 4

[20] P. Berini, Gagnon G, and S. J. Charbonneau. Thermo-optic plasmon-polariton devices. *US Patent 7043134*, 2006. 4, 13

[21] P. Berini. Optical waveguide structures. *US Patent 6741782*, 2004. 5, 40

[22] K. Tanaka and M. Tanaka. Simulations of nanometric optical circuits based on surface plasmon polariton gap waveguide. *Applied Physics Letters*, 82, 2003. 5

[23] K. Tanaka and M. Tanaka. Simulations of nanometric optical circuits: Open-type surface plasmon polariton gap waveguide. *Japanese Journal of Applied Physics*, 42, 2003. 5

[24] J. Q. Lu and A. A. Maradudin. Channel plasmons. *Physical Review B*, 42, 1990. 6

[25] I. V. Novikov and A. A. Maradudin. Channel polaritons. *Physical Review B*, 66, 2002. 6

[26] S. I. Bozhevolnyi, V. S. Volkov, E. Devaux, and T. W. Ebbesen. Channel plasmon-polariton guiding by subwavelength metal grooves. *Physical Review Letters*, 95, 2005. 6

[27] A. Boltasseva, V. S. Volkov, R. B. Nielsen, E. Moreno, S. G. Rodrigo, and S. I. Bozhevolnyi. Triangular metal wedges for subwavelength plasmon-polariton guiding at telecom wavelengths. *Optics Express*, 16, 2008. 6

[28] L. Liu, Z. Han, and S. He. Novel surface plasmon waveguide for high integration. *Optics Express*, 13, 2005. 6

[29] A. Mekis, J. C. Chen, I. Kurland, S. Fan, P. R. Villeneuve, and J. D. Joannopoulos. High transmission through sharp bends in photonic crystal waveguides. *Physical Review Letters*, 77, 1996. 6

[30] A. Boltasseva. Plasmonic components fabrication via nanoimprint. *Journal of Optics A*, 11, 2009. 6

[31] R. W. Rendell and D. J. Scalapino. Surface plasmons confined by microstructures on tunnel junctions. *Physical Review B*, 24, 1981. 7

[32] D. Heitmann. Radiative decay of surface plasmons excited by fast electrons on periodically modulated silver surfaces. *Journal of Physics C*, 10, 1977. 7

[33] M. V. Bashevoy, F. Jonsson, A. V. Krasavin, and N. I. Zheludev. Generation of traveling surface plasmon waves by free-electron impact. *Nano Letters*, 6, 2006. 7

[34] E. Kretschmann and H. Raether. Radiative decay of nonradiative surface plasmons excited by light. *Zeitschrift für Naturforschung A*, 23, 1968. 8

[35] A. Otto. Exitation of nonradiative surface plasma waves in silver by the method of frustrated total reflection. *Zeitschrift für Physik*, 216, 1968. 8

[36] G. J. Kovacs and G. D. Scott. Attenuated total reflection angular spectra and associated resonant electromagnetic oscillations of a dielectric slab bounded by ag films. *Applied Optics*, 17, 1978. 8

[37] T. Inagaki, M. Motosuga, E. T. Arakawa, and J. P. Goudonnet. Coupled surface plasmons excited by photons in a free-standing thin silver film. *Physical Review B*, 31, 1985. 9

[38] A. B. Evlyukhin, S. I. Bozhevolnyi, A. L. Stepanov, R. Kiyan, C. Reinhardt, S. Passinger, and B. N. Chichkov. Focusing and directing of surface plasmon polaritons by curved chains of nanoparticles. *Optics Express*, 15, 2007. 9

[39] G. I. Stegeman, R. F. Wallis, and A. A. Maradudin. Excitation of surface polaritons by end-fire coupling. *Optics Letters*, 8, 1983. 10

[40] I. I. Smolyaninov, D. L. Mazzoni, and C. C. Davis. Imaging of surface plasmon scattering by lithographically created individual surface defects. *Physical Review Letters*, 77, 1996. 11

[41] A. Drezet, A. Hohenau, D. Koller, A. Stepanov, H. Ditlbacher, B. Steinberger, F. R. Aussenegg, A. Leitner, and J. R. Krenn. Leakage radiation microscopy of surface plasmon polaritons. *Materials Science and Engineering B*, 149, 2008. 11

[42] T. W. Ebbesen, C. Genent, and S. I. Bozhevolnyi. Surface-plasmon circuitry. *Physics Today*, 61, 2008. 12

[43] A. Degiron, P. Berini, and D. R. Smith. Guiding light with long-range plasmons. *Optics and Photonics News*, 19, 2008. 12, 13

[44] F. Lopez-Tejeira, S. G. Rodrigo, L. Martin-Moreno, F. J. Garcia-Vidal, E. Devaux, T. W. Ebbesen, J. R. Krenn, I. P. Radko, S. I. Bozhevolnyi,

M. U. Gonzalez, J. C. Weeber, and A. Dereux. Efficient unidirectional nanoslit couplers for surface plasmons. *Nature Physics*, 3, 2007. 12

[45] M. U. Gonzalez, J. C. Weeber, A. D. Baudrion, A. Dereux, A. L. Stepanov, J. R. Krenn, E. Devaux, and T. W. Ebbesen. Design, near-field characterization, and modeling of 45 surface-plasmon bragg mirrors. *Physical Review B*, 73, 2006. 12

[46] A Hohenau, J. R. Krenn, A. L. Stepanov, A. Drezet, H. Ditlbacher, B. Steinberger, A. Leitner, and F. R. Aussenegg. Dielectric optical elements for surface plasmons. *Optics Letters*, 30, 2005. 12

[47] J. R. Krenn, H. Ditlbacher, G. Schider, A. Hohenau, A. Leitner, and F. R. Aussenegg. Surface plasmon micro- and nano-optics. *Journal of Microscopy*, 209, 2002. 12

[48] R. Charbonneau, N. Lahoud, G. Mattiussi, and P. Berini. Demonstration of integrated optics elements based on long-ranging surface plasmon polaritons. *Optics Express*, 13, 2005. 12

[49] S. I. Bozhevolnyi, V. S. Volkov, E. Devaux, J. Y. Laluet, and T. W. Ebbesen. Channel plasmon subwavelength waveguide components including interferometers and ring resonators. *Nature*, 440, 2006. 12

[50] R. Charbonneau, C. Scales, I. Breukelaar, S. Fafard, N. Lahoud, G. Mattiussi, and P. Berini. Passive integrated optics elements based on long-range surface plasmon polaritons. *Journal of Lightwave Technology*, 24, 2006. 12

[51] A. Boltasseva, T. Nikolajsen, K. Leosson, K. Kjaer, M. S. Larsen, and S. I. Bozhevolnyi. Integrated optical components utilizing long-range surface plasmon polaritons. *Journal of Lightwave Technology*, 23, 2005. 12

[52] M. P. Nezhad, K. Tetz, and Y. Fainman. Gain assisted propagation of surface plasmon polaritons on planar metallic waveguides. *Optics Express*, 12, 2004. 12

[53] M. C. Gather, K. Meerholz, N. Danz, and K. Leosson. Net optical gain in a plasmonic waveguide embedded in a fluorescent polymer. *Nature Photonics*, 4, 2010. 12

[54] T. Nikolajsen, K. Leosson, and S. I. Bozhevolnyi. Surface plasmon polariton based modulators and switches operating at telecom wavelengths. *Applied Physics Letters*, 85, 2004. 13

[55] T. Nikolajsen, K. Leosson, and S. I. Bozhevolnyi. In-line extinction modulator based on long-range surface plasmon polaritons. *Optics Communications*, 244, 2005. 14

[56] G. Gagnon, N. Lahoud, G. A. Mattiussi, and P. Berini. Thermally activated variable attenuation of long-range surface plasmon-polariton waves. *Journal of Lightwave Technology*, 24, 2006. 14

[57] S. Park and S. H. Song. Polymeric variable optical attenuator based on long range surface plasmon polaritons. *Electronics Letters*, 42, 2006. 14

[58] P. G. Hermannsson. *Simulations of long-range surface plasmon polariton waveguides and devices.* M.Sc. Thesis - University of Iceland, 1st edition, 2009. 34, 64

[59] J. Jung, T. S{o40, 41, 54
ndergaard, and S. I. Bozhevolnyi. Theoretical analysis of square surface plasmon polariton waveguides for long-range polarization independent waveguiding. *Physical Review B*, 76, 2007.

[60] R. Courant. Variational methods for the solution of problems of equilibrium and vibrations. *Bulletin of the American Mathematical Society*, 49, 1943. 44

[61] R. D. Cook. *Finite Element Methods For Stress Analysis.* John Wiley and Sons, 1st edition, 1995. 44

[62] M. J. Turner, R. W. Clough, H. C. Martin, and L. J. Topp. Stiffness and deflection analysis of complex structures. *Journal of the Aeronautical Sciences*, 23, 1956. 44

[63] L. J. Segerling. *Applied Finite Element Analysis.* John Wiley and Sons, 1st edition, 1984. 47

[64] D. V. Hutton. *Fundamentals of Finite Element Analysis.* McGraw-Hill Companies, 1st edition, 2004. 49

[65] J. E. Flaherty. *Finite Element Analysis (CSCI, MATH 6860).* Rensselaer Polytechnic Institute, 1st edition, 2000. 50

[66] H. Ditlbacher, A. Hohenau, D. Wagner, U. Kreibig, M. Rogers, F. Hofer, F.R. Aussenegg, and J.R. Krenn. Silver nanowires as surface plasmon resonators. *Physical Review Letters*, 95, 2005. 55

[67] M. Kuttge, E.J.R. Vesseur, J. Verhoeven, H.J. Lezec, H.A. Atwater, and A. Polman. Loss mechanisms of surface plasmon polaritons on gold probed by cathodoluminsecence imaging spectroscopy. *Applied Physics Letters*, 93, 2008. 55

[68] C. Reinhardt, S. Passinger, B.N. Chichkov, C. Marquart, I.P. Radko, and S. Bozhevolnyi. Laser-fabricated dielectric optical components for surface plasmon polaritons. *Optics Letters*, 31(9), 2006. 79

[69] J. Grandidier, S. Massenot, G. Colas des Francs, A. Bouhelier, J.C. Weeber, L. Markey, A. Dereux, J. Renger, M.U. Gonzalez, and R. Quidant. Dielectric-loaded surface plasmon polariton waveguides: Figures of merit and mode characterization by image and fourier plane leakage microscopy. *Physical Review B*, 78, 2008. 79

[70] J. R. Black. Electromigration - a brief survey and some recent results. *IEEE Transactions on Electronic Devices*, 1969. 86

[71] K. Leosson, T. Nikolajsen, A. Boltasseva, and S. I. Bozhevolnyi. Long-range surface plasmon polariton nanowire waveguides for device applications. *Optics Express*, 14. 90

[72] C. Reinhardt, R. Kiyan, S. Passinger, A.L. Stepanov, A. Ostendorf, and B.N. Chichkov. Rapid laser prototyping of plasmonic components. *Applied Physics A*, 89, 2007. 97

[73] A. Seidel, C. Ohrt, S. Passinger, C. Reinhardt, R. Kiyan, and B. N. Chichkov. Nanoimprinting of dielectric loaded surface-plasmon-polariton waveguides using masters fabricated by 2-photon polymerization technique. *Journal of the Optical Society of America B*, 26, 2009. 97

7

Included Papers

Paper I

Compact plasmonic variable optical attenuator

K. Leósson
T. Rosenzveig
P.G. Hermannsson
A. Boltasseva

*Optics Express **16**(20) (2008) 15546.*

Compact plasmonic variable optical attenuator

Kristjan Leosson,[1,*] Tiberiu Rosenzveig,[1] Petur Gordon Hermannsson, [1]
and Alexandra Boltasseva[2]

[1] *Science Institute, University of Iceland, Dunhagi 3, IS-107 Reykjavik, Iceland*
[2] *DTU Fotonik, Department of Photonics Engineering, Technical University of Denmark, Oersteds Plads*
Building 343, DK- 2800, Kgs. Lyngby, Denmark
**Corresponding author: kleos@hi.is*

Abstract: We demonstrate plasmonic nanowire-based thermo-optic variable optical attenuators operating in the 1525-1625 nm wavelength range. The devices have a footprint as low as 1 mm, extinction ratio exceeding 40 dB, driving voltage below 3 V, and full modulation bandwidth of 1 kHz. The polarization dependent loss is shown to be critically dependent on the nanowire geometry but devices with polarization-dependent loss as low as ±2.5 dB PDL over most of the attenuation range have been fabricated. We propose an even more compact device design to reduce insertion loss to approximately 1 dB.

©2008 Optical Society of America

OCIS codes: (130.2790) Guided waves; (230.3120) Integrated optics devices; (230.7390) Waveguides, planar; (240.6680) Surface plasmons.

References and links

1. S.A. Maier, *Plasmonics: Fundamentals and Applications* (Springer, New York, 2007).
2. T. W. Ebbesen, C. Genet, and S. I. Bozhevolnyi,"Surface plasmon circuitry," Phys. Today **61**, 44-50 (2008).
3. A. Degiron, P. Berini, and D. R. Smith, "Guiding light with long-range plasmons," Opt. Photon. News **19**, 29-34 (2008).
4. K. Leosson, T. Nikolajsen, A. Boltasseva, and S. I. Bozhevolnyi, "Long-range surface plasmon polariton nanowire waveguides for device applications," Opt. Express **14**, 314-319 (2006).
5. L. Eldada, "Optical communication components," Rev. Sci. Instrum. **75**, 575-593 (2004).
6. H. Ma, A.K.-Y. Jen, and L. R. Dalton, "Polymer-based optical waveguides: Materials processing and devices," Adv. Mater. **14**, 1339-1365 (2002).
7. L. Eldada, "Advances in Polymer Integrated Optics," IEEE J. Sel. Top. Quantum Electron. **6**, 54-68 (2000).
8. D. Li, Y. Zhang, L. Liu, and L. Xu, "Low consumption power variable optical attenuator with sol-gel derived organic/inorganic hybrid materials," Opt. Express **14**, 6029-6034 (2006).
9. X. Jiang, et al., "Compact Variable Optical Attenuator Based on Multimode Interference Coupler," IEEE Photon. Technol. Lett **17**, 2361-2363 (2005).
10. Y.-O. Noh, H.-J. Lee, Y.-H. Won, and M.-C. Oh, "Polymer waveguide thermo-optic switches with -70 dB optical crosstalk," Opt. Commun. **258**, 18-22 (2006).
11. T. Nikolajsen, K. Leosson, and S.I . Bozhevolnyi, "In-line extinction modulator based on long-range surface plasmon polaritons," Opt. Commun. **244**, 455-459 (2005).
12. S. Park and S. H. Song, "Polymeric variable optical attenuator based on long range surface plasmon polaritons," Electron. Lett. **42**, 402-404 (2006).
13. G. Gagnon, N. Lahoud, G. Mattiussi, and P. Berini, "Thermally activated variable attenuation of long-range surface plasmon-polariton waves," J. Lightwave Technol. **24**, 4391-4402 (2006).
14. P. Berini, "Optical Waveguide Structures," US patent number 6,741,782 (2004).
15. J. Jung, T. Søndergaard, and S. I. Bozhevolnyi, "Theoretical analysis of square surface plasmon-polariton waveguides for long-range polarization-independent waveguiding," Phys. Rev. B **76**, 035434 (2007).
16. P. B. Johnson and R. W. Christy, "Optical Constants of the Noble Metals," Phys. Rev. B **6**, 4370-4379 (1972).

#99889 - $15.00 USD Received 7 Aug 2008; revised 12 Sep 2008; accepted 13 Sep 2008; published 17 Sep 2008

1. Introduction

Surface plasmon photonics has received considerable attention in recent years [1]. A good deal of research has focused on plasmonic waveguiding and basic components operating at telecommunications wavelengths [2,3], where the optical properties of metals tend to be favourable. This emphasis has been motivated by the prospect of realizing highly integrated optical components by utilizing the strong light confinement possible at metal surfaces. However, two main factors still prevent plasmonic components from competing with current and emerging platforms for integrated optics: high loss and strong polarization dependence. In order to address these issues, we have previously investigated metallic nanowires that guide light of arbitrary polarization with comparatively low loss [4]. In the present work, we demonstrate a compact variable optical attenuator with a high extinction ratio based on such a waveguide. We believe that this device represents a first step towards a viable plasmonic integrated optical component design compatible with current technologies.

Optical components used in modern telecommunications systems are fabricated using a variety of technologies, each exhibiting particular strengths and weaknesses in terms of size, speed, cost, reliability, optical loss, power consumption, scalability, etc. [5] In particular, the variable optical attenuator (VOA) which is widely used in optical networks, can be realized using many different platforms, including opto-mechanics, MEMS, thermo-optics, electro-optics, microfluidics, liquid crystals or direct fibre manipulation. Advances in the development of reliable optical polymers for planar lightwave circuits [6,7] have made the planar polymer technology a prime candidate for meeting the demand for compact, highly scalable, low-cost optical components. Polymer materials are particularly suited for realizing integrated thermo-optic components since the absolute value of the thermo-optic coefficient *dn/dT* in polymers is an order of magnitude larger than that of glass. Various types of thermo-optic polymer VOAs, based on Mach-Zehnder [8] or multimode-interferometers [9] or on digital optical switches [10], have been reported and some are commercially available.

Attenuators based on plasmonic stripe waveguides embedded in polymers [11,12] or sandwiched between glass and polymer [13], have also been demonstrated. Here, attenuation occurs by increased absorption in the metal and/or radiation out of the waveguides, caused by refractive index gradients induced by heating up the waveguide core or by using an adjacent heater. The devices are based on long-range surface plasmon polariton (LRSPP) stripe waveguides, dimensioned to minimize propagation loss (PL) and coupling loss (CL) to standard single-mode fibres [11,13]. A common problem of these devices is their high insertion loss (6-10 dB) and single-polarization operation.

2. Simulation

In order to compete with existing technologies, a plasmonic VOA must meet the target specifications of low insertion loss (<=1 dB), high attenuation (>=20 dB), low polarization-dependent and wavelength-dependent loss over the whole attenuation range, and low power consumption. Furthermore, response times (limited by heat transfer) should be similar to other thermo-optic components. We used computer simulations to determine the optimum structure for a plasmonic attenuator meeting as many of these specifications as possible.

The fact that a metal-dielectric interface only supports a TM-polarized surface wave means that orthogonal polarizations can only be transmitted if the metallic waveguide is symmetric with respect to 90° rotation. A simple geometry which fulfils this condition is the square-cross-section nanowire waveguide first suggested by Berini [14]. In contrast to the plasmonic stripe waveguides that support a long-ranging supermode composed of coupled modes associated with the top and bottom surfaces of the metal film, the nanowire waveguide has two degenerate long-ranging modes formed by superpositions of four coupled corner plasmon polariton modes. These supermodes, denoted $E^{(1,0)}$ and $E^{(0,1)}$ by Jung et al. [15], have their electric field pointing primarily in the x and y directions, respectively.

Following the approach of Jung et al. [15], we performed finite-element analysis of gold nanowires embedded in a dielectric cladding. Calculations were performed using COMSOL

#99889 - $15.00 USD Received 7 Aug 2008; revised 12 Sep 2008; accepted 13 Sep 2008; published 17 Sep 2008

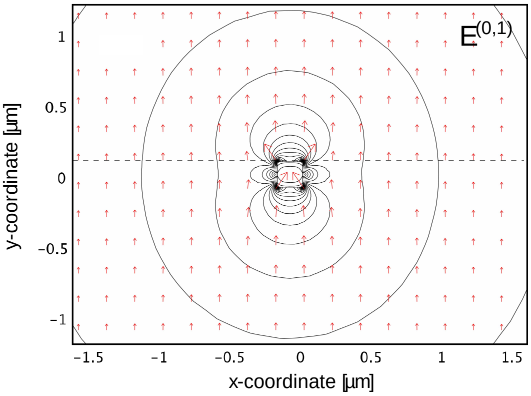

Fig. 1. Calculated magnitude and direction (in the x-y plane) of the electric field of the y-polarized $E^{(0,1)}$ mode in the vicinity of the wire, illustrating the high field intensity close to the corners

Multiphysics® (RF module) to determine the plasmonic modes in our devices. We modelled the cross-section of gold nanowire waveguides (n=0.52+10.7i, interpolated from the data of Johnson & Christy [16]) embedded in a 24-µm thick dielectric cladding (n=1.535, corresponding to our experimental conditions outlined below) bounded by air and silicon (n=3.48) on the top and bottom, respectively. We used rounded-square cross-sections (5 nm corner radius) for the wires with a maximum mesh density (<1 nm grid size) at the corners. Details of the corner rounding have been shown to have minimal effect on the calculation [15]. It should be emphasized, however, that the finite cladding thickness significantly influences the mode as the wire gets narrower. Due to the extra confinement, the finite cladding thickness results in higher propagation loss for a given wire cross-section, compared to the case of an “infinite” cladding assumed in previously published work [14,15]. The magnitude and direction of the electric field of the $E^{(0,1)}$ mode in a symmetric nanowire is shown in Fig. 1. At distances larger than a few 100 nm from the surface of the wire, the electric field is purely y-polarized. The x-polarized $E^{(1,0)}$ mode is obtained simply by 90° rotation about the z-axis.

Our calculations yielded a maximum achievable mode overlap of 93% (CL=0.3 dB) between a Gaussian fibre mode and the long-range modes of a square nanowire. For the particular case of a standard single mode fibre, with a mode-field diameter (MFD) of 10.5 µm, coupled to a gold wire embedded in a 24-µm thick BCB polymer, the maximum overlap occurs for wires with a 240 nm × 240 nm cross-section (1550 nm wavelength). This nanowire size, however, gives a substantial propagation loss of approximately 8 dB/mm. For a 1-mm long device, a minimum calculated insertion loss of 4.0 dB is obtained for a 180 nm × 180 nm cross-section (CL=1.1 dB/coupling, PL=1.7 dB/mm) which we used as a nominal design parameter in our devices.

In order to achieve optical attenuation, we use the concept of ref. [11], where light is expelled from the plasmonic waveguide by reducing the refractive index around the waveguide core. For a metallic waveguide embedded in a polymer ($dn/dT < 0$), this is simply done by passing an electrical current through the metal, directly heating the volume around the waveguide. The device geometry used in the present work is illustrated in Fig. 2.

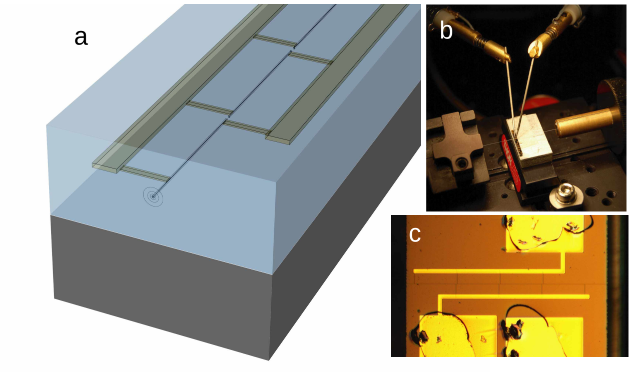

Fig. 2. (a) Schematic picture of the device geometry. The plasmonic nanowire waveguide is divided into short sections connected to common electrodes in order to increase device yield. (b) A 1-mm long chip containing 12 individual VOAs. Light is coupled to the device under test through polarization-maintaining optical fibres for extinction measurements. (c) Optical microscope image of a fully processed device, showing the layout of electrodes and contact pads.

3. Experiment

Our devices were fabricated as follows: A 100-mm silicon wafer was spin-coated with adhesion promoter (AP3000, DOW Chemical Co.) followed by a 12-µm thick layer of benzocyclobutene (BCB) polymer (CYCLOTENE 3022-57, DOW Chemical Co.). The BCB layer was cured in nitrogen atmosphere at 210°C for 40 minutes. The wafers were spin-coated with a 220-nm thick layer of ZEP520 electron beam resist (Zeon Corporation). The resist was covered with a 15 nm layer of thermally evaporated Al to avoid charge build-up during exposure and exposed in a JEOL-JBX9300FS electron-beam writer. The aluminium was removed by wet-etching before developing the resist using ZED-N50 developer (Zeon Corporation). Gold was deposited by e-beam evaporation to the desired wire thickness, followed by lift-off in resist remover. The wafer was then coated with a layer of photoresist (maN-1420, Micro Resist Technology GmbH) for patterning of contacts by UV-lithography. 300-nm thick gold contacts were fabricated using thermal deposition and lift-off in acetone. Finally, the wafer was covered with a second layer of BCB and hard-cured in nitrogen atmosphere at 250°C for 60 minutes. The wafer was diced into individual 1-mm and 2-mm long components. Contact pads were exposed by locally breaking off the polymer layer covering the pads. Fabricating electrically conducting millimetre-long, square-symmetric nanowires is a challenging task, and breaks commonly occur in our fabricated devices. In order to increase the device yield, we divided the waveguides into 200-µm long sections, individually connected to common electrodes (see Fig. 2). This resulted in an acceptable device yield, at the cost of increased propagation loss (due to isolation gaps and contact leads) and variation between individual devices (that might have one or more unheated sections).

Transmission measurements were carried out using a tuneable laser (Tunics Plus, GN Nettest) coupled to a polarization-maintaining fibre (Nufern PM1550-HP). The fibre was manually aligned to the plasmonic waveguide for maximum transmission. The signal was picked up at the output end using standard single mode fibre (Corning SMF-28) or a polarization maintaining fibre (as above) and measured with a calibrated Ge photodiode or a

#99889 - $15.00 USD Received 7 Aug 2008; revised 12 Sep 2008; accepted 13 Sep 2008; published 17 Sep 2008

fast InGaAs detector (Thorlabs, Inc.) for response time measurements. For extinction measurements, index matching liquid was used between the fibre and the sample to improve the coupling. Polarization dependent loss was measured with the Jones matrix method (using an Agilent/Hewlett-Packard 8509b Lightwave Polarization Analyzer) as well as by measuring the insertion loss while scanning the input state of polarization over the full Poincaré sphere. Mode images for different polarizations were obtained by imaging the output facet of the devices onto an infrared Vidicon camera (Hamamatsu) using a 0.85 NA 60× objective, while varying the polarization of the input fibre.

3. Results

Images of the mode output of a fabricated device are shown in Figs. 3(a) and (b), for input light polarized along the y or the x-direction, respectively. Both modes are close to circular with very similar mode shapes. In our devices, the x-polarized $E^{(1,0)}$ mode is always associated with higher insertion loss and more stray light in the cladding, possibly due to a slight deviation from square symmetry and/or increased scattering by the 500-nm wide contact leads.

The field intensity profiles directly above the nanowire (along the dashed line in Fig. 1), for the $E^{(0,1)}$ and $E^{(1,0)}$ modes, are shown in Fig. 3(c). The strong field intensity at the corners of the nanowire waveguide is a property of the surface plasmon polariton wave and cannot be imaged using free-space optics. In order to compare the measured mode profiles with the results of the simulation, we must therefore take into account the spatial resolution of our imaging system. We therefore performed a 2D-convolution of the calculated intensity distribution (time-averaged power) with a response function corresponding to the spatial resolution of our imaging system, given by $1.21\times\lambda/\mathrm{NA}$. Horizontal mode profiles were obtained by integrating the resulting intensity distribution along the y-axis. Experimentally obtained mode images were similarly integrated for the comparison.

We find that the experimental data is in excellent agreement with the resolution-corrected simulated profiles. The best fit to the measured data was obtained for a 190 nm × 190 nm wire which is close to the nominal dimensions of our fabricated structures (180 nm × 180 nm). The minimum measured insertion loss (5 dB and 8 dB for the $E^{(0,1)}$ mode in 1-mm and 2-mm long devices, respectively) was higher than expected from simulations (4.1 dB and 6.3 dB, respectively), presumably due to the combined effects of scattering due to metal roughness, scattering and absorption by contact leads and loss in the cladding. The insertion loss of a 1-mm device varied by ±1 dB over the tuning range of the laser, covering the C- and L-bands (1525-1625 nm). The lowest polarization dependent loss (PDL) measured in our 1-mm devices was 1.2 dB, although typical values were in the 3-6 dB range.

In order to determine the extinction characteristics, we measured the fibre-to-fibre loss of the attenuators while applying voltage to the electrodes and monitoring the electrical power dissipated as heat in the device. The input polarization was fixed at 45° with respect to the x and y axes while the intensity of x and y-polarized light transmitted through the device was measured separately using a polarizer in front of the detector. Fig. 4 shows results for three different devices. As the applied power increases, the transmitted intensity drops for both polarizations. In some cases, attenuation of over 40 dB was measured (e.g. for the $E^{(0,1)}$ mode in Fig. 4(c)). The response time of the device was measured to be 500 µs for heating and 1 ms for cooling, with a 3-dB decrease in modulation depth occuring at around 5 kHz for a fixed driving voltage amplitude.

Measurements of the electrical resistance of the nanowire waveguide indicated a temperature increase in the metal of about 80 K at 30 mW/mm applied power. Finite-element simulations of heat transfer in our devices yielded the same value and confirmed that at this level of heating, the real part of the effective refractive index of the long-range plasmonic modes in a symmetric wire is closely approaching that of unbound modes propagating in the cladding, increasing substantially the radiative loss from the waveguides.

The PDL over the attenuation range varied substantially between devices. Symmetric wires may exhibit different PDL at zero applied power (compare Figs. 4(a) and (b)) while the

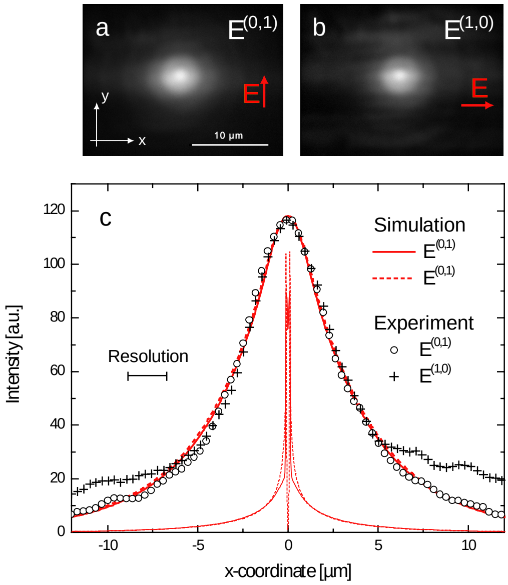

Fig. 3. Images of the output facet of a 2-mm long, nominally 180 nm × 180 nm square nanowire waveguide for (a) y-polarized and (b) x-polarized input light, corresponding to the $E^{(0,1)}$ and $E^{(1,0)}$ long-range corner plasmon polariton supermodes, respectively. The red arrows indicate the direction of the dominating electric field component of the output light. (c) The field intensity along the dashed line in Fig. 1 for the orthogonally polarized long-range modes (thin red lines) and the x-profile of the full calculated 2D intensity distribution of the same calculation, corrected for finite image resolution, integrated along the y-axis (thick red lines) and normalized in intensity. The experimental points represent the x-profile of panels a and b, integrated along the y-axis and scaled in absolute intensity. Results for the two modes are nearly identical, except for the increased background level in case of the x-polarized mode. The simulated data was obtained for a 190 nm × 190 nm wire, which gave the best fit to the experimental profiles.

relative extinction ratio for each mode can be similar (PDL varying within ±2.5 dB over most of the attenuation range). Slightly asymmetric wires (width > height), however, exhibit large PDL at higher attenuation, indicating that the x-polarized mode is more easily coupled out of the wire while the y-polarized mode is more strongly bound. It is clear that achieving consistently low PDL in this type of attenuator requires fabrication tolerances below 10 nm for patterning of the metal stripes.

Evidently, our fabricated devices still suffer from too high insertion loss to meet the target specifications listed above, even with improvements in contact geometry, wire quality and coupling. Nevertheless, several strategies can be pursued in order to reach acceptable loss values. Coupling loss to narrow wires with low propagation loss can be significantly reduced using large mode area waveguides at the input and output. This, however, would limit the bending radius of other components and lead to lower integration density. On-chip mode conversion similarly requires propagation lengths that would counteract the advantages of a compact attenuator. Engineering the refractive index profile of the cladding, however, might provide a means of tailoring the mode size while maintaining acceptable propagation loss.

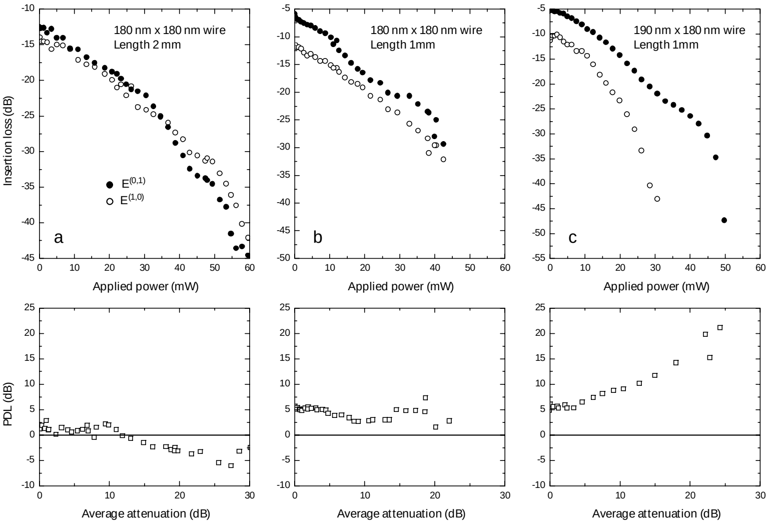

Fig. 4. The upper panels show fibre-to-fibre insertion loss for three different device geometries. The input was linearly polarized at 45° with respect to the waveguide axes and the x and y-polarized output was measured. Insertion loss is plotted relative to the direct fibre-to-fibre transmission of each polarization direction. The difference between the x and y-polarized insertion loss is plotted in the lower panels, illustrating the variation between devices and the high sensitivity to small variations in the cross-sectional geometry. The maximum driving voltage in all cases is below 3V.

Shorter devices would also reduce the overall insertion loss, reaching approximately 1 dB for 100-µm long wires. The extinction ratio achievable with such devices is yet to be determined.

4. Conclusions

In conclusion, we have demonstrated a nanowire-based plasmonic variable optical attenuator with a 1-mm footprint, >20 dB extinction ratio, <3V driving voltage and >1 kHz modulation bandwidth, operating in the 1525-1625 nm wavelength range. The minimum dimensions of the structures are within the capabilities of current photolithographic techniques and the device structure is compatible with a planar polymer processing platform. The PDL at high attenuation was shown to be critically dependent on the square symmetry of the nanowire waveguide, with a <5% tolerance in the width-to-height ratio of the metal wire.

Acknowledgments

We thank P. Shi at Danchip, Technical University of Denmark (DTU), for assistance with e-beam lithography and C. Peucheret at the Department of Photonics Engineering, DTU, for providing the PDL test equipment. The project was supported by the Icelandic Research Fund. T.R. acknowledges support from the Eimskip Research Fund at the University of Iceland. A.B. acknowledges support from the Danish Research Council for Technology and Production Sciences (FTP).

Paper II

Modelling of polarization-dependent loss in plasmonic nanowire waveguides

T. Rosenzveig
P.G. Hermannsson
K. Leósson

Plasmonics ***5****(1) (2010) 75.*

Plasmonics (2010) 5:75–77
DOI 10.1007/s11468-009-9118-y

Modelling of Polarization-Dependent Loss in Plasmonic Nanowire Waveguides

**Tiberiu Rosenzveig · Petur G. Hermannsson ·
Kristjan Leosson**

Received: 24 March 2009 / Accepted: 22 December 2009 / Published online: 16 January 2010
© Springer Science+Business Media, LLC 2010

Abstract We have investigated the potential of using gold nanowires embedded in a dielectric cladding environment as polarization-independent long-range surface plasmon polariton waveguides at telecom wavelengths. We performed finite-element analysis on various symmetric and close-to-symmetric cross-sectional geometries and evaluated the effects of cladding thickness on the propagation and coupling loss. The calculations confirm that fabrication of polarization-independent waveguides with reasonable tolerances is feasible and that straight-waveguide insertion losses around 1.5 dB for short (0.5 mm) devices can be realized when coupling to and from conventional dielectric waveguide geometries.

Keywords Surface plasmons · Nanowires · Integrated optics

The field of surface plasmon–polariton (SPP) optics has attracted considerable interest recently. Passive and active devices based on surface plasmons have been proposed to complement conventional dielectric optical circuits [1]. There are mainly two potential advantages that devices based on SPPs can offer over traditional dielectric technologies: firstly, since the electromagnetic mode is strongly bound to the interface between the dielectric and the metal, a much higher degree of confinement is possible than with dielectric waveguides. On one hand, this allows for very compact devices to be designed and fabricated as light can be compressed to below the diffraction limit and, on the other hand, very high field intensities can be realized in relatively small volumes. Secondly, the bound electromagnetic wave is very sensitive to changes to the refractive index of the surrounding medium, making SPPs a prime candidate for sensing applications [2].

SPP circuits do, however, have several drawbacks when compared with traditional dielectric waveguides. The plasmon–polaritons propagating at the interface between a metal and a dielectric exhibit a high propagation loss due to the damping effect of the metal. This problem can be somewhat mitigated by using a thin film of metal (with thickness on the order of 10 nm) sandwiched between dielectric layers with equal refractive index [3–6]. In this case, the SPPs propagating at the upper and lower interface of the metal film couple and form a long-range surface plasmon polariton (LRSPP) supermode that is weakly bound to the metal film, thus reducing the losses. However, devices based on such waveguides only support modes with the electric field polarized perpendicular to the metal strip which is a strong disadvantage in interfacing with conventional fiber-optics. Berini suggested substituting the metal strip with a metallic nanowire with a symmetric square cross-section to solve the polarization problem [7] and propagation of orthogonal linear polarizations in such wires was recently confirmed experimentally [8]. Unlike the metallic strip, a wire with a square cross-section can support long-range supermodes with the electric field polarized predominantly along the x or y directions (denoted by Jung et al. [9] as $E^{(1,0)}$ and $E^{(0,1)}$, respectively). These supermodes are formed by specific superpositions of four corner-plasmon–polariton modes that propagate along the edges of the wire.

In this paper, we present simulations of propagation loss (due to metal absorption) and coupling loss (to standard single-mode fibers) at 1,550 nm wavelength for straight nanowire waveguides. The waveguides consist of gold wires embedded in a polymer cladding. We also calculate the effects of slight deviations from the symmetrical square

---

T. Rosenzveig (✉) · P. G. Hermannsson · K. Leosson
Department of Physics, Science Institute, University of Iceland,
Dunhagi 3,
IS-107 Reykjavik, Iceland
e-mail: jptibirosen@raunvis.hi.is

cross-section (rectangular and trapezoidal waveguides) on the polarization-dependent loss. Previous simulations of plasmonic nanowire waveguides in the literature have been concerned with modeling wires in an infinite cladding environment [9]. Here, we consider the effects of a finite cladding thickness on the loss figures and show how a finite cladding thickness can substantially affect the propagation and coupling loss. A suitable cladding geometry can thus be used to reduce the total insertion loss of short nanowire waveguide devices.

We performed finite-element analysis on plasmonic waveguides consisting of gold nanowires embedded in a polymer cladding. Commercially available finite-element software, COMSOL Multiphysics (RF module) was used for modeling. The modelled system consisted of a gold nanowire, characterized by a complex refractive index $\tilde{n}$= 0.52+10.7i at 1,550 nm wavelength [10] surrounded by dielectric with n=1.535 (similar to, e.g., [4]), bounded by air on all sides as shown in the inset of Fig. 1. For simplicity, we did not take into account the presence of a substrate. For thin cladding layers, radiation will leak into a high-index substrate (e.g., silicon) but this can be avoided by using an intermediate lower-index dielectric layer between the cladding and the substrate.

We first investigated nanowires with square cross-section with different side lengths. To avoid unrealistically sharp corners, the squares were rounded with a radius of 5 nm. The literature suggests [9] that a modest rounding of the corners has a minimal effect on the results of the finite-element calculations. Propagation loss was determined from the calculated effective refractive index of the linearly polarized supermodes, whereas coupling loss was obtained from the 2-D overlap integral between the LRSPP mode field and the field from a standard single-mode optical fiber

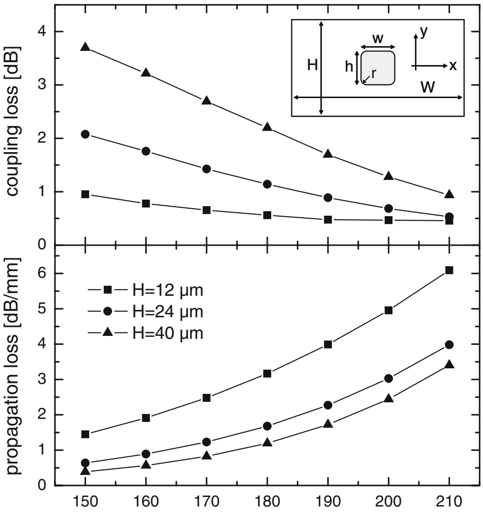

Fig. 1 Coupling loss and propagation loss in symmetric nanowire waveguides. Calculations for three different cladding thicknesses are shown. Results are shown for the long-range mode with the electric field polarized in the *y-direction*, as indicated in the figure

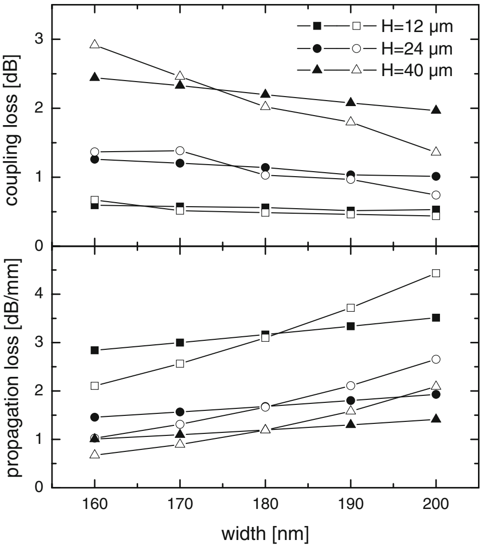

Fig. 2 Propagation loss and coupling loss in asymmetric nanowire waveguides for the y-polarized $E^{(0,1)}$ mode (*closed symbols*) and the x-polarized $E^{(1,0)}$ mode (*closed symbols*). The height of the wires is fixed at h=180 nm

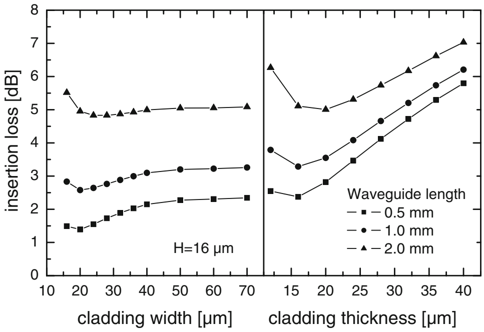

Fig. 3 Total insertion loss for different lengths of symmetric nanowire waveguides (180×180 nm) when the extent of the dielectric cladding layer is limited vertically (*right panel*) and both vertically and horizontally (*left panel*)

(taken as Gaussian, with a mode–field diameter of 10.5 μm). It should be noted that the maximum overlap between the fiber mode and the LRSPP mode occurs where the 1/e mode width measure used in [9] is much smaller than the 1/e mode size of the fiber due to the high field intensity occurring at the corners of the metal wire, reflecting the importance of using suitable measures of plasmon mode size for a particular application, as pointed out by Oulton et al. [11].

Figure 1 shows the calculated propagation loss and coupling loss for gold wires with a square cross-section, with the side length of the square varying between 150 and 210 nm. Since the polymer layers are not infinitely thick, they provide an additional confinement for the plasmon mode. Calculations for infinitely wide dielectric therefore give weaker confinement and lower propagation loss values [7, 9]. The total thickness of the cladding in our simulations was varied between 12 and 40 μm, with the wire being sandwiched halfway through. As expected, similar results are obtained for both polarizations in the symmetric wire case. It should be emphasized that the simulation only accounts for propagation loss due to the damping effect of the metal. A weakly bound mode with low damping will suffer larger bending losses as well as increased scattering losses due to imperfections in the metal wire (roughness) or polymer film.

While the propagation loss increases with the size of the wire cross-section, the coupling loss decreases, as the overlap with the fiber mode improves. As noted above, the finite-thickness cladding also provides additional confinement. For narrow wires, the increased confinement from a thinner cladding substantially decreases the coupling loss while causing only a modest increase in propagation loss for short devices. In order to minimize the insertion loss for a given device length, a compromise must therefore be reached, depending on the geometry of the particular geometry.

In order to determine geometric tolerances for realizing polarization-independent waveguides, we considered the case of slightly asymmetrical cross-sections: a rectangle with the height of 180 nm and widths ranging from 160 to 200 nm (with the same rounded corners as in case of the symmetrical wires). The results of the simulation are shown in Fig. 2. It is evident that a 5% asymmetry ($[h-w]/h$) can result in substantial polarization-dependent loss. The coupling and propagation loss values, however, are affected differently, and the variation is also influenced by the cladding thickness. Again, the correct compromise based on the actual device geometry can be used to improve the tolerance to fabrication errors.

In order to determine the minimum insertion loss for straight-waveguide sections of different length, we calculated propagation losses and fiber-to-fiber coupling losses for different cladding thicknesses as shown in Fig. 3, right panel. Taking the cladding thickness that gives a minimum insertion loss for short (0.5–1 mm) devices, we also calculated the effect of reducing the width of the cladding layer in the horizontal direction, as shown in Fig. 3, left panel. This results in a minimum insertion loss close to 1.4 dB for the 0.5 mm device length. We have previously demonstrated short (1–2 mm) variable optical attenuator (VOA) devices with high extinction ratio based on electrically heated straight plasmonic nanowire waveguides [12] and propose that such devices can be made even shorter in order to realize insertion losses of around 1–2 dB. Such compact VOA devices could, e.g., be integrated within a polymer PLC platform.

Finally, we have noted experimentally that metal deposition of nanostructures with high aspect ratios does not result in vertical sidewalls. We therefore investigated the effect of a trapezoidal wire shape on the calculated polarization dependence of the wires while keeping the cross-sectional area constant. For modest side wall angles (up to 6°), the difference in propagation loss for the two linear polarizations remains small (<0.1 dB/mm) and should not contribute significantly to PDL in short samples.

In summary, we have modeled plasmonic nanowire waveguides consisting of gold nanowires embedded in a dielectric cladding and investigated the effects of the shape of the wire cross-section and the cladding thickness on the propagation and coupling loss. The critical dimensions and geometric tolerances required for realizing zero-PDL long-range plasmonic waveguides are within the capabilities of current lithographic techniques. Compact (sub-millimeter) components utilizing the properties of the metallic waveguide could therefore be considered for integration with conventional dielectric waveguide platforms operating at telecom wavelengths.

Acknowledgments The project was supported by the Icelandic Research Fund, the Eimskip Research Fund at the University of Iceland.

References

1. Ebbesen TW, Genet C, Bozhevolnyi SI (2008) Phys Today 61:44
2. Hoa XD, Kirk AG, Tabrizian M (2007) Biosens Bioelectron 23:151
3. Berini P (1999) Opt Lett 24:1011
4. Nikolajsen T, Leosson K, Salakhutdinov I, Bozhevolnyi SI (2003) Appl Phys Lett 82:668
5. Boltasseva A, Nikolajsen T, Leosson K, Kjaer K, Larsen MS, Bozhevolnyi SI (2005) J Lightwave Technol 23:413
6. Degiron A, Berini P, Smith DR (2008) Opt Photon News 19:29
7. Berini P (2004) US Patent number 6,741,782
8. Leosson K, Nikolajsen T, Boltasseva A, Bozhevolnyi SI (2006) Opt Express 14:314
9. Jung J, Søndergaard T, Bozhevolnyi SI (2007) Phys Rev B 76:035434
10. Johnson PB, Christy RW (1972) Phys Rev B 6:4370
11. Oulton RF, Bartal G, Pile DFP, Zhang X (2008) New J Phys 10:105018
12. Leosson K, Rosesnzveig T, Hermannsson PG, Boltasseva A (2008) Opt Express 16:15546

Paper III

Optimizing performance of plasmonic devices for photonic circuits

T. Rosenzveig
P.G. Hermannsson
A. Boltasseva
K. Leósson

Applied Physics A ***100****(2) (2010) 341.*

Appl Phys A
DOI 10.1007/s00339-010-5862-2

Applied Physics A
Materials Science & Processing

Optimizing performance of plasmonic devices for photonic circuits

Tiberiu Rosenzveig · Petur Gordon Hermannsson ·
Alexandra Boltasseva · Kristjan Leosson

Received: 13 August 2009 / Accepted: 1 June 2010
© Springer-Verlag 2010

Abstract We demonstrate the feasibility of fabricating thermo-optic plasmonic devices for variable optical attenuation and/or low-frequency (kHz) signal modulation. Results of finite-element simulations and experimental characterization of prototype devices indicate that a plasmonic device can reach specifications similar to or better than commercially available thermo-optic integrated optical components. Specifically, we have considered the insertion loss, power consumption, footprint, polarization-dependent loss, extinction ratio, and frequency response of the plasmonic devices, in addition to fabrication and material-related issues. The most serious fabrication challenge is to realize metallic nanowire waveguides with a sufficiently accurate cross-section to ensure low polarization-dependent loss at high extinction ratios.

1 Introduction

Surface plasmon polaritons (SPPs) are often associated with sub-wavelength confinement of light and a number of passive and active devices based on guiding of highly confined SPPs have been proposed [1]. It is, however, also possible to use so-called long-range surface plasmon polariton (LRSPP) waveguides [2–4] with weaker confinement to realize individual optical components that maintain compatibility with current mode-size standards but can, in some cases, have a significantly smaller footprint than their dielectric counterparts [5, 6]. Nevertheless, several challenges have to be overcome in order to compete with glass or polymer-based integrated optics, mainly those of insertion loss and polarization dependence. Other factors such as response time, power consumption, dynamic range, scalability and fabrication tolerances also have to be critically assessed.

In the present paper, we address these issues for plasmonic waveguide devices designed for variable optical attenuation and/or low-frequency modulation at telecom wavelengths, using finite-element simulations and experimental characterization.

2 Target specifications

A variable optical attenuator (VOA) attenuates the intensity of an optical input in a controlled manner. VOAs are important components of modern optical networks where they are used for regulating power levels to protect receivers and prevent saturation, gain flattening in wavelength division multiplexed networks, dynamic channel equalization in cross-connected nodes, channel blanking and channel labeling for network monitoring, etc.

As a reference component, we consider a commercially available thermo-optic polymer-based integrated variable optical attenuator supplied by Enablence Technologies Inc. (previously DuPont Photonics).[1] According to the manufac-

T. Rosenzveig · P.G. Hermannsson · K. Leosson (✉)
Science Institute, University of Iceland, Dunhagi 3, 107
Reykjavik, Iceland
e-mail: kleos@hi.is
Fax: +354-552-8911

A. Boltasseva
School of Electrical and Computer Engineering, Birck
Nanotechnology Center, Purdue University, West Lafayette, IN
47907, USA

A. Boltasseva
DTU Fotonik, Department of Photonics Engineering, Nano·DTU,
Technical University of Denmark, DTU Building 343, 2800
Kongens Lyngby, Denmark

---

[1] http://www.enablence.com/media/pdf/enablence_ivoa_datasheet.pdf.

Published online: 22 June 2010

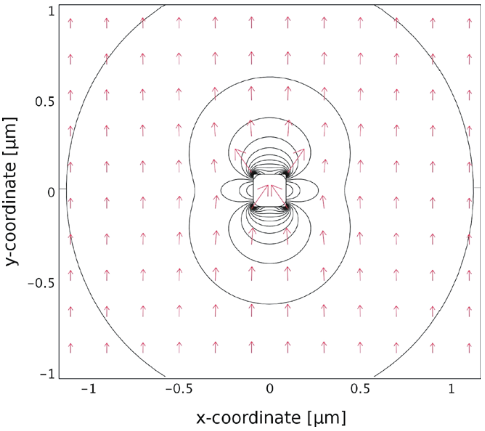

Fig. 1 The calculated magnitude and direction of the electric field of the predominantly y-polarized $E^{(0,1)}$ mode propagating along a 180 nm × 180 nm gold wire embedded in a dielectric cladding. The x-polarized $E^{(1,0)}$ mode is obtained by 90° rotation

turers datasheet, the packaged device has an off-state insertion loss of 1.3 dB, extinction ratio of 20 dB, response time of 3 ms, power consumption of 40 mW/channel and PDL ≤ 0.7 dB over the attenuation range. Although not stated in the datasheet, it can be assumed that the devices operate on an interferometric principle, with the actual device length being around 10 mm [7].

3 Waveguide structure

Polarization-dependent loss (PDL) is one of the key features of devices in the optical network where polarization generally changes randomly with time. Components based on conventional LRSPP waveguides consisting of thin metal stripes embedded in a homogeneous dielectric environment only support guiding of light polarized perpendicular to the stripe surface. Square cross-section nanowire waveguides, however, were proposed [8] and experimentally verified [9] to serve as polarization-independent plasmonic waveguides. A metallic wire with a square cross-section in an uniform dielectric environment supports long-range supermodes (combinations of four corner modes) with the electric field oriented predominantly along the x or y directions, as shown in Fig. 1. Following Jung et al. [10], we label these modes $E^{(1,0)}$ and $E^{(0,1)}$, respectively. In practical situations, the dielectric cladding will have a finite thickness, which may influence the plasmonic modes as discussed in Sec. 4.

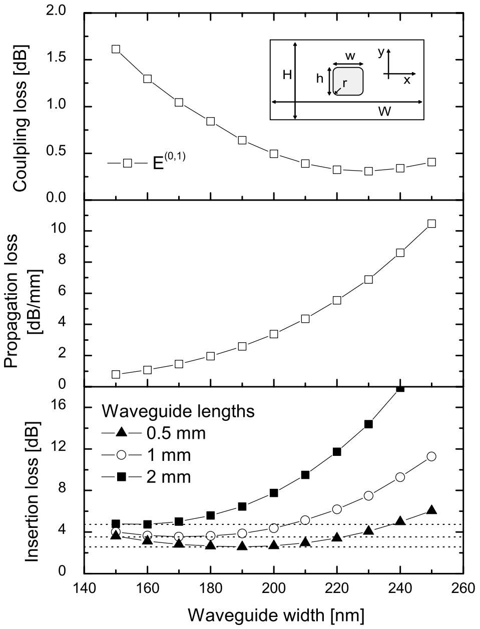

Fig. 2 Calculated coupling loss, propagation loss and fiber-to-fiber insertion loss for 0.5-, 1- and 2-mm long gold nanowire waveguides in a 20 µm thick cladding layer at $\lambda = 1550$ nm. Similar values are obtained for both polarizations, so only the $E^{(0,1)}$ results are shown. The *inset* in the top panel schematically shows the simulated device geometry

4 Insertion loss

Effective mode indices and field distributions were determined by finite-element analysis[2] of plasmonic waveguides consisting of square-symmetric gold nanowires embedded in a polymer cladding, similar to experimentally fabricated devices [6]. Modeling was performed using a free-space wavelength of 1550 nm. The gold nanowire ($\tilde{n} = 0.52 + 10.7i$ [11]) was surrounded by a dielectric cladding ($n = 1.535$), bounded by air on all sides as shown in the inset of Fig. 2. For each nanowire side length, the resulting mode profile was used to determine the minimum end-fire coupling loss by calculating the overlap with the Gaussian fiber mode of a single-mode fiber (SMF28) having a mode-field diameter of 10.5 µm.

Propagation loss due to absorption in the metal (neglecting scattering, absorption in the polymer and radiation leakage) was derived from the calculated effective mode indices. The results are shown in Fig. 2 along with the insertion loss (2 × CL + PL × length) of 0.5-, 1- and 2-mm long straight waveguide components with 20 µm cladding thickness. A minimum coupling loss of 0.31 dB (corresponding to a mode overlap of 93%) was obtained for a waveguide having 230-nm side length. However, for this side length, the propagation loss has an unacceptably large value of 6 dB/mm. For short waveguide sections (0.5–1 mm), the optimum wire side length is in the range 170–190 nm. Nevertheless, the lowest theoretical insertion loss for a 0.5-mm device (around 3 dB), still exceeds our target specifications.

---

[2] Comsol Multiphysics (RF module), http://www.comsol.com.

In order to further tailor the mode size of the plasmonic nanowire modes, additional confinement can be provided by modifying the cladding geometry, as described in detail in Ref. [12]. For narrow wires in particular, the increased confinement from a thinner cladding substantially decreases the coupling loss while causing only a modest increase in propagation loss. Furthermore, performance can be optimized using a hybrid dielectric-plasmonic waveguide geometry with the nanowire embedded in a square dielectric core with a side length of about 16 µm (in air). This results in a minimum insertion loss close to 1.4 dB for a 0.5-mm device length. More realistically, the hybrid plasmonic-dielectric waveguide should be embedded in a low-index polymer (e.g. Cytop or Teflon AF) which will give a slightly different optimum dielectric core size.

Previously, short (1–2 mm) VOA devices with high extinction ratios have been realized [6] and we propose that such devices can be made even shorter in order to bring insertion losses down to 1–2 dB. It remains to be seen, however, how the added confinement and reduced length affect the power consumption and achievable extinction ratio of the VOA device.

5 Extinction mechanism

The operation of the currently investigated plasmonic VOA makes use of the negative thermo-optic coefficient of polymers [13]. By passing electrical current through the waveguide core, the effective refractive index of the guided mode is changed due to the temperature-dependent refractive index of the cladding material. The exact extinction mechanism, however, has not previously been determined. By simulating the heat flow in our nanowire devices (see inset of Fig. 3) and determining the resulting temperature and refractive index profiles, we followed the change in the eigenmodes of the structure as heating power was increased. The temperature dependence of the dielectric function of gold [14] was also included in the model. As expected, the long-range modes expand upon heating and become slightly asymmetric due to the asymmetric cooling conditions above and below the cladding (here, the presence of a substrate acting as an effective heat sink was taken into account, while cooling at the top surface was treated as simple heat conduction to still air). The effective refractive index of the guided mode drops and eventually crosses into the regime corresponding to freely propagating modes in the cladding which develops a significant index gradient due to the temperature profile.

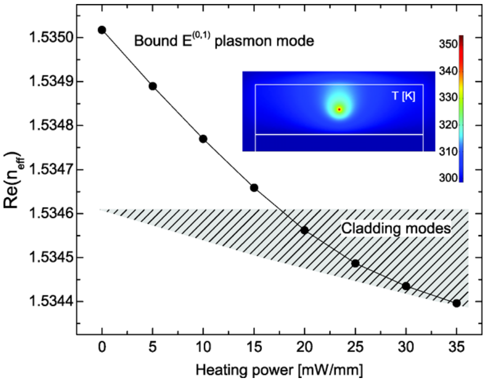

Fig. 3 The real part of the effective index for the $E^{(0,1)}$ mode versus electrical heating power for a gold nanowire. The grey area corresponds to the refractive index of the cladding layer which has a temperature-induced index gradient. The calculated temperature profile (color) is shown in the *inset*, corresponding to a heating power of 20 mW/mm

By calculating propagation and coupling losses for an electrically heated 180 nm × 180 nm wire, we can determine whether changes in these parameters fully account for the extinction ratio observed in our VOA devices. The calculation assumes an abrupt (non-adiabatic) coupling to the heated section which is reasonable since the temperature gradient along the propagation direction from heated to unheated sections of the waveguide only extends over a few wavelengths. In general, the coupling loss increases with heating power while propagation loss decreases, as shown in Fig. 4. The combined effect, however, only amounts to a 4–6 dB extinction at 30 mW/mm heating power for 1-mm long devices, whereas 10–15 dB are observed experimentally in wires with similar dimensions [6] at the corresponding power levels. We therefore conclude that scattering of plasmons to radiative cladding modes contributes substantially to the extinction. We have shown experimentally that extinction ratios significantly higher than our target specification can be realized, even in devices as short as 1 mm [6].

6 Fabrication issues; symmetry, adhesion layers, hysteresis

Geometric tolerances for realizing polarization-independent waveguides were considered in Ref. [12], where it was

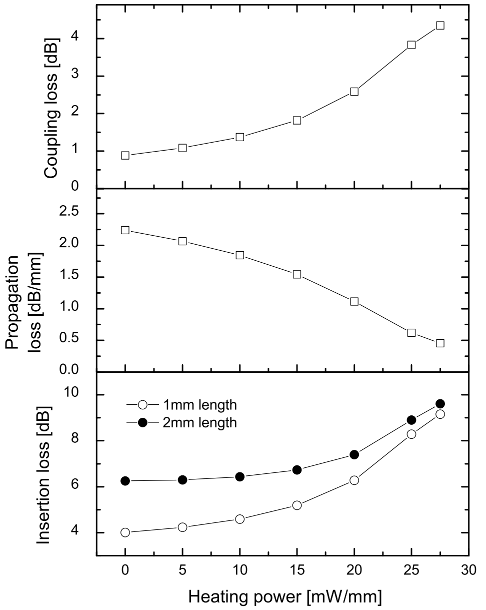

Fig. 4 Effect of heating on coupling loss and propagation loss in nanowire waveguides. The total insertion loss increases with heating, but the change is considerably smaller than observed in experiment

found that a small deviation from square symmetry will result in significantly polarization-dependent propagation and coupling loss, although the two contributions partially cancel out. Simulation results indicate that for 1-mm long devices, the total PDL is < 0.6 dB, for up to $\pm 10\%$ asymmetry, which is within acceptable limits from the fabrication point of view. Experiments show, however, that the PDL at high extinction ratios depends much more critically on wire dimensions [6]. In order to meet target specifications for PDL over the whole attenuation range, therefore, asymmetry of the wires presumably has to be kept below 2%.

Another potential source of polarization dependence is the presence of a thin adhesion layer, required to avoid delamination of the waveguides from the polymer substrate during the lift-off process. Adhesion layers were found to have a substantial impact on the localization of near-field resonances in bow-tie antennas [15] as well as for fluorescence enhancement in plasmonic structures [16], and the selection of adhesion layer materials was shown to be critical. Due to the high electric field concentration at the corners of the nanowire waveguide, significant effects can also be expected on the transmission and polarization dependence of such waveguides. We have therefore evaluated the effect of two commonly used adhesion materials, Cr and Ti, on the propagation loss and polarization dependence in symmetric nanowire waveguides, using finite-element calculations. Part of the waveguide material was replaced by the adhesion layer material, keeping the total thickness of the structure constant. As shown in Fig. 5, the propagation loss for a 180 nm × 180 nm waveguide increases from below 2 dB/mm for the case with no adhesion layer, to about 3 dB/mm for the y-polarized mode when using a 3-nm layer of Ti or Cr. The effect, however, is less pronounced for the x-polarized mode. The PDL can be balanced, therefore, by using a slightly asymmetric structure (width > height), at the cost of increased overall insertion loss.

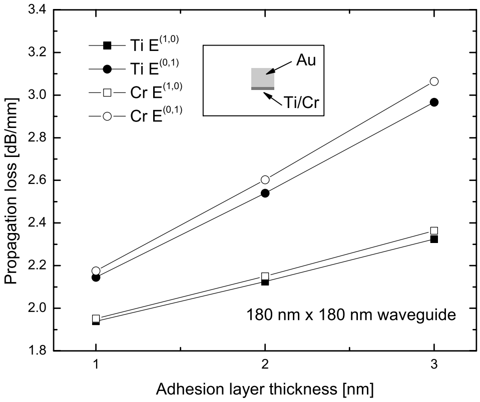

Fig. 5 Calculated effect of adhesion layers on propagation loss and polarization dependence in a 1-mm long symmetric nanowire waveguide

As discussed above, the time response to thermo-optical modulation of plasmonic nanowire devices generally follows a simple model: When stepping the heating current, the power dissipation will change instantly but the waveguide core temperature will change in accordance with the heat capacity and thermal resistance to the heat sink (silicon substrate). Effectively, this is an exponential decay towards steady-state. The time constant of this thermal time response is in the sub-millisecond range, as shown in the following section. However, the BCB polymer also demonstrates a time-dependent thermo-optical memory effect (hysteresis), where the refractive index is a function of both present and past temperature. This effect is observed when bringing a VOA from the off-state up to a high-extinction state and then back (Fig. 6). The magnitude of the effect grows with the maximum temperature and the time constant of relaxation, back to the original starting point, is of the order of several hours. The plasmonic VOA functionality relies on having a negative thermo-optic coefficient. Many optical polymers are available for realizing plasmonic VOA's, and proper care

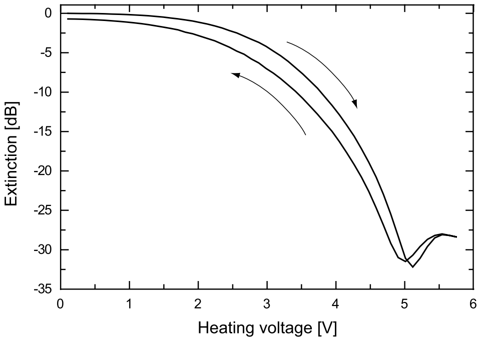

Fig. 6 Measured thermo-optical memory effect in BCB polymer. A plasmonic VOA heated to achieve >30 dB extinction exhibits a slowly reversible refractive index change when returned to the off-state

must be taken when selecting cladding materials to ensure proper thermal characteristics, stability, etc.

In general, the structural quality of the metallic waveguides is of central importance for ensuring low polarization dependence, low scattering loss, and long lifetime (limited by electromigration effects, which will be the subject of a separate publication).

7 Response time

As with other thermo-optic components, the time response of the plasmonic VOA device discussed here is limited by heat transfer. We performed simulations of thermal transients upon switching the device from the on-state to the off-state. Results were compared with measurements of the modulation of the optical signal as a function of frequency for a fixed-amplitude square-wave driving signal. Calculations show 1–2 ms heat transients which agrees well with the observed modulation roll-off at around 1 kHz, see Fig. 7. Small-signal modulation up to 100 kHz is possible at reduced output power, making the device suitable for, e.g., low-frequency pilot-tone generation (for channel labeling). Improved heat conduction from the core, e.g. through reduction of cladding thickness, will increase the bandwidth of the device but the power consumption for full modulation will simultaneously increase. The optimum tradeoff will depend on the particular application of the device.

8 Conclusions

In summary, we have shown that plasmonics can play a role in integrated optics outside the nanophotonic regime, by providing an efficient method of thermo-optic control of guided signals. To be fully competitive with existing technologies, however, the main fabrication challenge lies in highly accurate patterning of metallic nanostructures. With the current rapid improvements in nanoscale fabrication techniques and the importance of high-quality metallic nanostructures for plasmonics in general, these challenges might well be overcome in the near future.

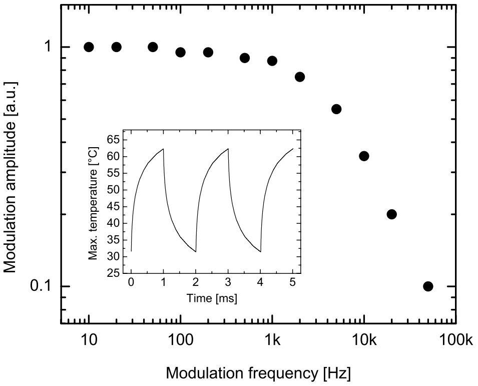

Fig. 7 Measured frequency response of the plasmonic nanowire attenuator/modulator for a fixed driving voltage amplitude (2 V). The inset shows the simulated temperature transients in the vicinity of the wire for a 0.5 kHz modulation, with the extent of the y-axis corresponding to full modulation

Acknowledgements The project was supported by the Icelandic Research Fund (grant no. 00700221021) and the Eimskip Research Fund.

References

1. T.W. Ebbesen, C. Genet, S.I. Bozhevolnyi, Phys. Today **61**, 44 (2008)
2. P. Berini, Opt. Lett. **24**, 1011 (1999)
3. T. Nikolajsen, K. Leosson, I. Salakhutdinov, S.I. Bozhevolnyi, Appl. Phys. Lett. **82**, 668 (2003)
4. P. Berini, Adv. Opt. Photon. **1**, 484 (2009)
5. A. Boltasseva, S.I. Bozhevolnyi, T. Nikolajsen, K. Leosson, J. Lightwave Technol. **24**, 912 (2006)
6. K. Leosson, T. Rosenzveig, P.G. Hermannsson, A. Boltasseva, Opt. Express **16**, 15546 (2008)
7. L. Eldada, R. Norwood, R. Blomquist, L.W. Shacklette, M.J. McFarland, in *Proc. Optical Fiber Communication Conf.* (2000), p. W124
8. P. Berini, Optical waveguide structures. U.S. Patent 6,741,782 2004
9. K. Leosson, T. Nikolajsen, A. Boltasseva, S.I. Bozhevolnyi, Opt. Express **14**, 314 (2006)
10. J. Jung, T. Søndergaard, S.I. Bozhevolnyi, Phys. Rev. B **76**, 035434 (2007)
11. P.B. Johnson, R.W. Christy, Phys. Rev. B **6**, 4370 (1972)

12. T. Rosenzveig, P.G. Hermannsson, K. Leosson, Plasmonics **5**(1), 75–77 (2010)
13. T. Nikolajsen, K. Leosson, S.I. Bozhevolnyi, Opt. Commun. **244**, 455 (2005)
14. M. Rashidi-Huyeh, B. Palpant, Phys. Rev. B **74**, 075405 (2006)
15. X. Jiao, J. Goeckeritz, S. Blair, M. Oldham, Plasmonics **4**, 37 (2009)
16. H. Aouani, J. Wenger, D. Gerard, H. Rigneault, E. Devaux, T.W. Ebbesen, F. Mahdavi, T. Xu, S. Blair, ACS Nano **3**, 2043 (2009)

Paper IV

Demonstration of laser-fabricated DLSPPW at telecom wavelength

A. Seidel
C. Reinhardt
T. Holmgaard
W. Cheng
T. Rosenzveig
K. Leósson
S.I. Bozhevolnyi
B.N. Chichkov

IEEE Photonics Journal ***2****(4) (2010) 652.*

IEEE Photonics Journal
An IEEE Photonics Society Publication

Demonstration of Laser-Fabricated DLSPPW at Telecom Wavelength

Volume 2, Number 4, August 2010

Andreas Seidel
Carsten Reinhardt
Tobias Holmgaard
Wei Cheng
Tiberiu Rosenzveig
Kristjan Leosson
Sergey I. Bozhevolnyi
Boris N. Chichkov

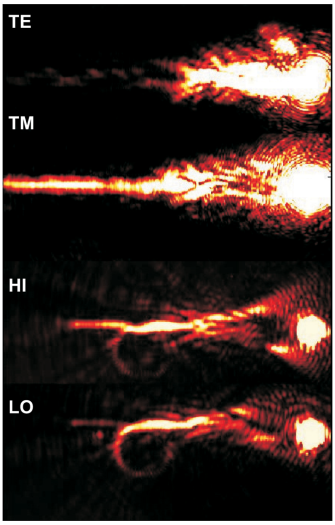

DOI: 10.1109/JPHOT.2010.2056490
1943-0655/$26.00 ©2010 IEEE

Demonstration of Laser-Fabricated DLSPPW at Telecom Wavelength

Andreas Seidel,[1] **Carsten Reinhardt,**[1] **Tobias Holmgaard,**[2]
Wei Cheng,[1] **Tiberiu Rosenzveig,**[3] **Kristjan Leosson,**[3]
Sergey I. Bozhevolnyi,[4] **and Boris N. Chichkov**[1]

[1]Laser Zentrum Hannover e.V., 30419 Hannover, Germany
[2]Department of Physics and Nanotechnology, Aalborg University, 9220 Aalborg Øst, Denmark
[3]Science Institute, University of Iceland, 107 Reykjavik, Iceland
[4]Institute of Sensors, Signals, and Electrotechnics, University of Southern Denmark,
5230 Odense M, Denmark

DOI: 10.1109/JPHOT.2010.2056490
1943-0655/$26.00 ©2010 IEEE

Manuscript received June 1, 2010; revised June 23, 2010; accepted June 23, 2010. Date of publication June 29, 2010; date of current version July 19, 2010. This work was supported by the PLASMOCOM project under Grant EC FP6 IST 034754 STREP, COST Action MP 0803, and the Center for Quantum Engineering and Space-Time Research (QUEST). Corresponding author: A. Seidel (e-mail: a.seidel@lzh.de).

Abstract: We investigate dielectric-loaded surface plasmon-polariton waveguides (DLSPPWs) fabricated by two-photon polymerization direct laser writing and nanoimprinting at the telecom wavelength of 1550 nm. We examine several types of structures such as lines and bends as individual plasmonic components. Racetrack resonators are presented as a potential application of this technology. These plasmonic components can be investigated at 1550-nm wavelength by leakage radiation microscopy using an InGaAs camera. The experimentally observed behavior of these components in a leakage radiation microscope matches the theoretical expectations. The results demonstrate the practical feasibility of laser-fabricated DLSPPW components at telecom wavelength.

Index Terms: Plasmonics, DLSPPW, two-photon polymerization.

1. Introduction

Future increases of speed and efficiency in the area of information technology require a shift from electronic to photonic components and their miniaturization. Such a route of technological development demands new materials with the capability to guide optical signals at dimensions shorter than the wavelength, below the diffraction limit. Within the field of nanophotonics, plasmonics, and, in particular, plasmonic waveguides offer such a route.

Surface plasmon-polaritons (SPPs) are collective oscillations of surface electrons in a metal coupled to light at the metal–dielectric interface [1], along which they can propagate and along which they are highly confined [2]. Components utilizing propagating SPPs have been proposed for performing a variety of functions, such as highly sensitive sensing [3], but are particularly promising in the area of information technology to provide a link between electronics and integrated optics [4], [5]. Several technologies have been proposed for plasmonic waveguides, including metal strips embedded in a dielectric also known as long-range plasmons [6], the opposite configuration—dielectric stripes embedded in metal [7], and nanowires [8]. Another approach is that of dielectric-loaded surface plasmon-polariton waveguides (DLSPPWs), which is generating growing interest and attention [9]–[15].

We present DLSPPW structures fabricated by two-photon polymerization (2PP) direct laser writing technology and nanoimprinting using molds from masters made by the aforementioned

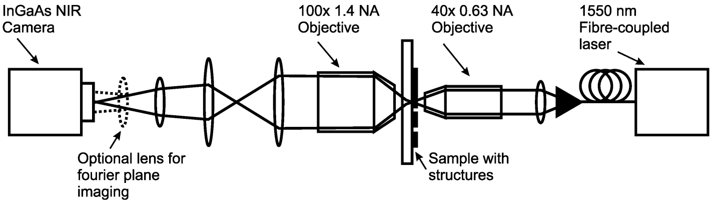

Fig. 1. Schematic image of the leakage radiation microscopy setup. An additional lens can be inserted just in front of the camera for Fourier plane imaging.

method. The structures are analyzed by leakage radiation microscopy at the 1550-nm telecommunications wavelength.

Two-photon polymerization has already been shown to be a highly flexible, versatile, and efficient tool in making DLSPPW structures [16]–[18]. The greatest advantage of this technique compared to, for example, UV mask lithography, is the fact that it is suitable as a rapid prototyping technique of DLSPPW structures, where new designs can be rapidly and cheaply produced. Nanoimprinting large numbers of structures in parallel has been used for the fabrication of plasmonic waveguides in general [4] and has also been demonstrated to work for DLSPPW structures [19].

2. Structure Fabrication

Using the 2PP method, the structures are directly written in a UV-curable photoresist on a glass substrate covered with a 50-nm gold layer. The photoresist is the spincoatable mr-NIL 6000.3 made by the company microresist in Berlin, Germany. The gold layer must be thick enough to support SPPs with reasonable propagation length, and at the same time, it must be thin enough to allow for sufficient leakage radiation to obtain useful measurement data. Fifty nanometers has proved to be the optimum thickness for fulfilling both requirements. After development, the DLSPPW structures consist of ridges of 500–600-nm width and 500-nm height. This geometry has been shown to be a single-mode plasmonic waveguide at 1550 nm [20], [21].

While the 2PP process is fast and highly flexible, it is a serial process not well adapted for mass-production of plasmonic components. Therefore, we consider it important to show that nanoimprinting (a parallel process) is also a suitable fabrication method. Here, master structures are fabricated on glass and used to make a PDMS mold, which in turn is used to imprint structures using the same photoresist as above onto a new glass substrate also covered with a 50-nm gold layer. The entire procedure is given in more detail in source [19].

3. Experimental Setup

For the characterization of the DLSPPW, leakage radiation microscopy is applied. This method has been demonstrated at visible wavelengths [19], [22]. Here, we use the same method at telecom wavelength wavelengths to demonstrate its applicability to the near-infrared regime.

As our primary light source we use a fiber laser emitting at 1550 nm. After collimation, the light is focused by a 40 × 0.63 NA objective onto the structures. To collect the leakage radiation it is necessary to use a high-NA objective due to the shallow emission angle. We use a 100 × 1.4 NA objective with oil immersion. The light is then focused onto a Hamamatsu InGaAs camera, which is highly sensitive in this spectral range. The camera is used to image both the direct image plane, as well as the Fourier plane by adding an additional lens. A schematic of the setup is shown in Fig. 1.

4. Leakage Radiation Microscopy Results and Interpretation

We show DLSPPW mode propagation on several different samples and different DLSPPW geometries. First, we will consider straight waveguides of 50–100 μm length with funnels attached on one end to aid excitation of the DLSPPW mode. The funnels have a base width of 10 μm and are

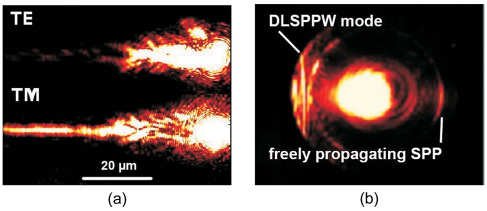

(a) (b)

Fig. 2. Leakage radiation microscope images of a line waveguide with funnel, being excited at the funnel end by TE and TM polarized light, respectively. As can be seen in (a), the waveguide cannot support an optical TE mode but only a plasmonic TM mode. The Fourier plane image of the TM mode is shown in (b).

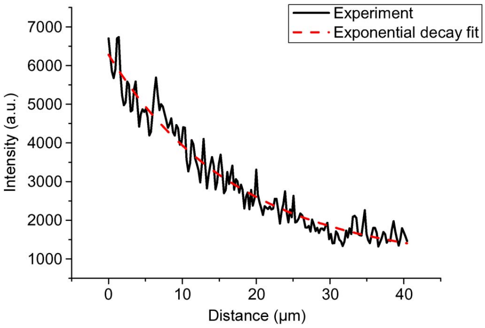

Fig. 3. Plot of the leakage radiation measured inside a line waveguide which is a direct indication of radiation intensity. An exponential fit is also shown.

25 μm long. We excite the DLSPPW mode in all our structures by focusing our laser beam on the edge of the funnel base. The resulting SPPs are viewed by leakage radiation microscopy. Fig. 2 illustrates the fact that the DLSPPW structures can only support plasmonic TM modes and not optical TE modes. While the waveguide is brightly illuminated in TM mode, showing strong evidence of leakage radiation from a plasmonic mode, it is completely dark when polarization is switched to TE. The Fourier plane image is also shown in Fig. 2. By taking into account that the innermost circle of the image corresponds to our objective's NA of 0.63, we can calculate the real part of the effective index of our DLSPPW structure simply by measuring the distance of the mode from the center of the circle. We measure an effective index of $\mathrm{Re}(n_{\mathrm{eff}}) = 1.13 \pm 0.01$. This low value is due to the refractive index $n = 1.29$ of the polymer.

The intensity of the DLSPPW mode inside the waveguide is measured using the leakage radiation, which is fitted to an exponential curve to extract the propagation length L_{prop}. That this is a reasonable method and provides a good match can be seen in Fig. 3, where such a fit curve is superimposed on the experimental results. The waveguides are clearly single mode, an improvement over the multimode waveguides published previously [14]. An analysis of the decay rate of the DLSPPW mode in several straight waveguides (line waveguides) with funnels, combined with the effective index $n_{\mathrm{eff}} = 1.13$, gives us an average propagation length of $L_{\mathrm{prop}} = 20 \pm 1$ μm. This shows some improvement compared with figures previously published using similar structures fabricated by UV mask lithography [23].

Additionally, we have a nanoimprinted version of the line waveguide. Fig. 4 shows a DLSPPW mode propagating inside a nanoimprinted line waveguide. Analysis of the mode decay rate in these

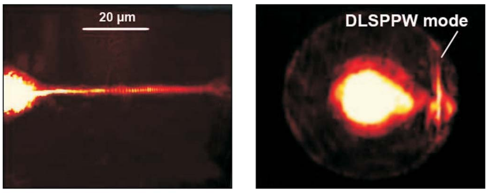

(a) (b)

Fig. 4. (a) Leakage radiation microscopy image showing a nanoimprinted line waveguide with incoupling funnel. (b) The Fourier plane image of the same line.

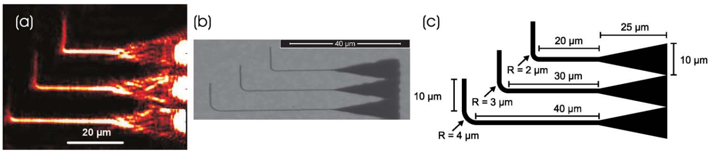

Fig. 5. (a) Leakage radiation microscope images of three bends with different curve radius. Descending from top to bottom, the curve radius is 2, 3 and 4 μm. The three images were taken separately and then merged. (b) SEM image of the structures. (c) A schematic drawing of the structures.

TABLE 1

Transmission results for bend DLSPPW structures

bend radius (μm)	transmission
2	0.17
3	0.26
4	0.31

nanoimprinted waveguides reveals an effective index $n_{\text{eff}} = 1.11$ and a propagation length of $L_{\text{prop}} = 7.6 \pm 0.3$ μm. These results are in the same range as previous results from nanoimprinted waveguides examined at 632-nm wavelength [19], but in contrast to the previous waveguides, these are single mode. There is a significant difference in the value of the propagation length when we compare the nanoimprinted and the directly written case. The explanation for this is the presence of a thin residual layer of polymer covering the sample surface in the nanoimprinted case, which leads to increased scattering, and the inclusion of dust particles in the nanoimprinting process, which leads to increased roughness and minor distortions of the structures. Both of these aspects could be improved by using more advanced equipment in a cleanroom environment.

To realize fully the potentials of DLSPPW structures for proposed miniature photonic-plasmonic hybrid circuits [24], curved waveguides are necessary. In fact, the minimal bend radius with tolerable signal losses defines the level of miniaturization that is obtainable; therefore, the investigation of bended DLSPPWs is a prerequisite for more complicated components. A series of 90° bends fabricated directly on gold by 2PP was investigated. We find that for bend radii of 2, 3 and 4 μm, the DLSPPW mode is guided through the bend, albeit with some scattering out of the waveguide. An image of the bends is shown in Fig. 5. An SEM image showing the design of the entire structure is also shown. The bend structure is designed to ease fabrication and characterization by providing a compact structure with a common baseline.

Transmission measurements were performed using the leakage radiation. The starting and ending points of the waveguide bend itself were taken as reference points for each waveguide, without regard to the incoupling waveguides. The results, which are listed in Table 1), show that

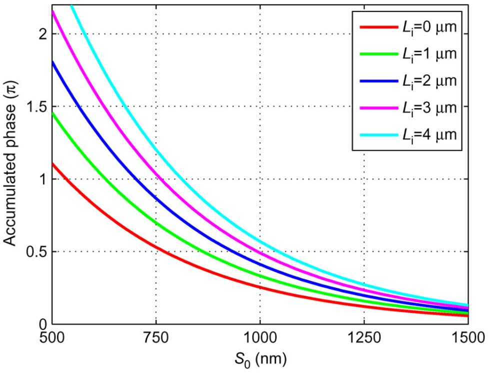

Fig. 6. EIM calculation of the accumulated phase difference ($\lambda = 1550$ nm) throughout the racetrack resonator as a function of the center-to-center separation of the (500-nm-wide and 600-nm-tall) waveguide ridges in the parallel section ($S_0 = 500$ nm corresponds to the absence of gap). The accumulated phase is plotted in units of π for different lengths of the parallel section ranging from $L_i = 0$ μm (ring resonator) to $L_i = 4$ μm. The waveguide parameters are adapted from [26].

waveguides with larger bend radii are more efficient at guiding the DLSPPW mode around a corner due to the reduction in bend scattering losses.

A more-complex DLSPPW component is a racetrack resonator. These resonators consist of a racetrack-shaped line in close proximity to a straight-line waveguide. In our investigations, the gap between racetrack and line was 500 nm. The DLSPPW mode can couple from the line waveguide in which it is launched to the racetrack resonator. Depending on wavelength or resonator length, the radiation inside the racetrack will be either in phase or out of phase with the mode in the line waveguide, which will lead to constructive or destructive interference. As such, these racetrack resonators can act as resonant filters for a variable-frequency signal. Ring-shaped DLSPPW resonators fabricated by UV lithography have already been shown to work in very similar fashion with variable laser frequency [25].

Racetrack resonators differ from ring resonators in that they have a straight interaction section which runs parallel with the waveguide, thus elongating the interaction region. This implies that one can increase the waveguide-resonator separation for a desired coupling ratio to the resonator, thus relaxing the requirements on the resolution in the fabrication. This feature is demonstrated by calculating the accumulated phase difference throughout the whole racetrack resonator (see Fig. 6), using effective index method (EIM) calculations and the supermode approach, which has previously proven accurate for describing the coupling between two adjacent DLSPPWs [26].

In plasmonic resonators, one usually requires ca. 50% coupling to the resonator [25] in order to obtain critical coupling, which translates into an accumulated phase difference of $\pi/2$. For a ring resonator, this can be achieved with a center-to-center separation of $S_0 = 770$ nm, implying a gap of only 270 nm, whereas a racetrack resonator with a parallel section of 3 μm, increases this gap to 500 nm, as shown in Fig. 6. Such an increase is in many fabrication techniques crucial in order to realize well-resolved structures, thus making the racetrack resonator a promising structure in plasmonics.

An example of racetrack resonators, fabricated directly on gold by 2PP, in operation is shown in Fig. 7, where two slightly different racetrack resonators are shown. The long waveguide (at the top in the image) shows constructive interference in the output waveguide. The difference in length of the racetrack resonators in the two pictures is 2 μm. To translate this into effective wavelengths, we must first calculate the value of the effective wavelength in the waveguide using the effective index $n_{\text{eff}} = 1.13$, which gives us $\lambda_{\text{eff}} = 1.3717$ μm. If we then divide the length difference by this value,

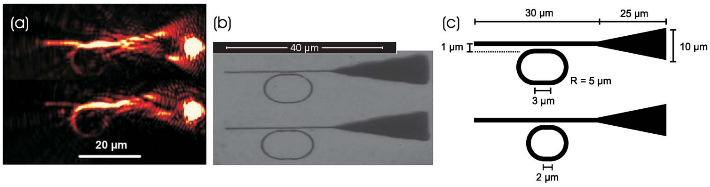

Fig. 7. (a) Leakage radiation microscope images of two racetrack resonator structures. The length difference between the two racetracks is 2 μm, which amounts to a nearly 180° phase difference, resulting in destructive interference at the waveguide output in the case of the shorter racetrack resonator. The damping is in excess of 16 dB. (b) SEM image of the structures. (c) A schematic drawing of the structures.

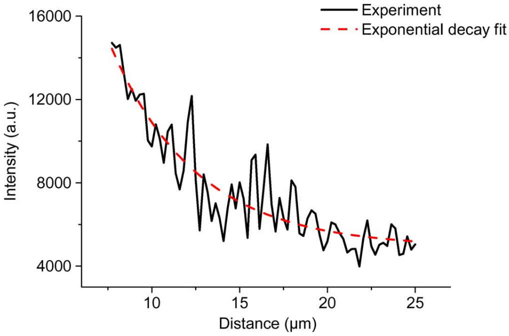

Fig. 8. Plot of the leakage radiation intensity inside the semi-circular bend of a racetrack waveguide. An exponential fit is also shown.

we get a difference of 1.46 wavelengths. Consequently, the phase change is nearly 180°, leading to an expectation of a high suppression of output in the case of the shorter resonator, which is precisely what we see in the experimental results. However, the racetrack resonator and subsequent interference is not the main cause of this result. The measured propagation length for the 5 μm semi-circular bend is $L_{\text{prop}} = 4.92 \pm 0,72$ μm, indicating some scattering out of the waveguide, which is also visible in the image. A plot of the intensity inside the bend and a superimposed exponential fit is shown in Fig. 8.

When we now consider the total length of the racetrack resonator, it becomes clear that the signal inside the racetrack becomes too weak to interfere significantly with the signal inside the line waveguide. The results stem from the fact that in the case of a 3-μm interaction length, the phase difference along this stretch is close to 2π, which means that the mode couples to the racetrack and back again. In the case of the shorter interaction length, the mode couples only to the racetrack and is diverted away. The large coupling is due to the low mode effective index of 1.13 and the corresponding low mode confinement.

5. Conclusion

In conclusion, we have demonstrated DLSPPW mode guiding by leakage radiation microscopy in laser-fabricated and nanoimprinted DLSPPW structures at the 1550-nm telecommunication wavelength. We presented DLSPPW racetrack resonators as a potential application of this technology in the form of resonant filters. The racetrack resonators show large coupling to the resonator. Due to the low mode confinement, the coupling is much larger than anticipated, and due to the low propagation length, the fabricated structures do not operate as designed, but this can be remedied by increasing the mode effective index by using different waveguide materials in the future.

References

[1] S. A. Maier, *Plasmonics—Fundamentals and Applications*. New York: Springer-Verlag, 2007.

[2] H. Raether, *Surface Plasmons on Smooth and Rough Surfaces and on Gratings*. New York: Springer-Verlag, 1988.

[3] S. Lal, S. Link, and N. J. Halas, “Nano-optics from sensing to waveguiding,” *Nat. Photon.*, vol. 1, no. 11, pp. 641–648, Nov. 2007.

[4] A. Boltasseva, “Plasmonic components fabrication via nanoimprint,” *J. Opt. A, Pure Appl. Opt.*, vol. 11, no. 11, p. 114001, Sep. 2009.

[5] T. W. Ebbesen, C. Genet, and S. I. Bozhevolnyi, “Surface-plasmon circuitry,” *Phys. Today*, vol. 61, no. 5, pp. 44–50, 2008.

[6] A. Degiron, P. Berini, and D. R. Smith, “Guiding light with long-range plasmons,” *Opt. Photon. News*, vol. 19, no. 7, pp. 29–34, 2008.

[7] E. Verhagen, J. Dionne, L. Kuipers, H. Atwater, and A. Polman, “Near-field visualization of strongly confined surface plasmon polaritons in metal-insulator-metal waveguides,” *Nano Lett.*, vol. 8, no. 9, pp. 2925–2929, Sep. 2008.

[8] K. Leosson, T. Rosenzveig, P. Hermannsson, and A. Boltasseva, “Compact plasmonic variable optical attenuator,” *Opt. Express*, vol. 16, no. 20, pp. 15 546–15 552, Sep. 2008.

[9] R. Wan, F. Liu, and Y. Huang, “Ultrathin layer sensing based on hybrid coupler with short-range surface plasmon polariton and dielectric waveguide,” *Opt. Lett.*, vol. 35, no. 2, pp. 244–246, Jan. 2010.

[10] J. Chen, Z. Li, S. Yue, and Q. Gong, “Hybrid long-range surface plasmon-polariton modes with tight field confinement guided by asymmetrical waveguides,” *Opt. Express*, vol. 17, no. 26, pp. 23 603–23 609, Dec. 2009.

[11] W. Xue, Y. Guo, and W. Zhang, “Modified surface plasmonic waveguide formed by nanometric parallel lines,” *Chin. Phys. B*, vol. 19, no. 1, p. 017302, Jan. 2010.

[12] M. Ranjbaran and X. Li, “Performance-enhanced superluminescent diode with surface plasmon waveguide,” *Opt. Express*, vol. 17, no. 26, pp. 23 643–23 654, Dec. 2009.

[13] V. Popescu, “Power absorption efficiency in plasmon—Polariton optical superconducting planar and rib waveguides,” *Optoelectron. Adv. Mater. Rapid Commun.*, vol. 3, pp. 1259–1263, 2009.

[14] C. Reinhardt, A. Seidel, A. Evlyukhin, W. Cheng, and B. Chichkov, “Mode-selective excitation of laser-written dielectric-loaded surface plasmon polariton waveguides,” *J. Opt. Soc. Amer. B, Opt. Phys.*, vol. 26, no. 12, pp. B55–B60, Sep. 2009.

[15] H. Luo, Y. Li, H. Cui, and Y. Hong, “Dielectric-loaded surface plasmon-polariton nanowaveguides fabricated by two-photon polymerization,” *Appl. Phys. A, Solids Surf.*, vol. 97, no. 3, pp. 709–712, Nov. 2009.

[16] J. Serbin, A. Ovsianikov, and B. Chichkov, “Fabrication of woodpile structures by two-photon polymerization and investigation of their optical properties,” *Opt. Express*, vol. 12, no. 21, pp. 5221–5228, Oct. 2004.

[17] R. Kiyan, C. Reinhardt, S. Passinger, A. L. Stepanov, A. Hohenau, H. R. Krenn, and B. N. Chichkov, “Rapid prototyping of optical components for surface plasmon polaritons,” *Opt. Express*, vol. 15, no. 7, pp. 4205–4215, Apr. 2007.

[18] A. B. Evlyukhin, S. I. Bozhevolnyi, A. L. Stepanov, R. Kiyan, C. Reinhardt, S. Passinger, and B. N. Chichkov, “Focusing and directing of surface plasmon polaritons by curved chains of nanoparticles,” *Opt. Express*, vol. 15, no. 25, pp. 16 667–16 680, 2007.

[19] A. Seidel, C. Ohrt, S. Passinger, C. Reinhardt, R. Kiyan, and B. Chichkov, “Nanoimprinting of dielectric loaded surface-plasmon-polariton waveguides using masters fabricated by 2-photon polymerization technique,” *J. Opt. Soc. Amer. B, Opt. Phys.*, vol. 26, no. 4, pp. 810–812, Mar. 2009.

[20] T. Holmgaard and S. Bozhevolnyi, “Theoretical analysis of dielectric-loaded surface plasmon-polariton waveguides,” *Phys. Rev. B, Condens. Matter*, vol. 75, no. 24, p. 245 405, Jun. 2007.

[21] T. Holmgaard, S. Bozhevolnyi, L. Markey, and A. Dereux, “Dielectric-loaded surface plasmon-polariton waveguides at telecommunication wavelengths: Excitation and characterization,” *Appl. Phys. Lett.*, vol. 92, no. 1, p. 011124, Jan. 2008.

[22] A. L. Stepanov, J. R. Krenn, H. Ditlbacher, A. Hohenau, A. Drezet, B. Steinberger, A. Leitner, and F. R. Aussenegg, “Dielectric optical elements for surface plasmons,” *Opt. Lett.*, vol. 30, no. 8, pp. 893–895, Apr. 2005.

[23] J. Grandidier, G. des Francs, S. Massenot, A. Bouhelier, L. Markey, J. C. Weeber, C. Finot, and A. Dereux, “Gain-assisted propagation in a plasmonic waveguide at telecom wavelength,” *Nano Lett.*, vol. 9, no. 8, pp. 2935–2939, Aug. 2009.

[24] X. Guo, M. Qiu, J. Bao, B. Wiley, Q. Yang, X. Zhang, Y. Ma, H. Yu, and L. Tong, “Direct coupling of plasmonic and photonic nanowires for hybrid nanophotonic components and circuits,” *Nano Lett.*, vol. 9, no. 12, pp. 4515–4519, Dec. 2009.

[25] T. Holmgaard, Z. Chen, S. I. Bozhevolnyi, L. Markey, and A. Dereux, “Dielectric-loaded plasmonic waveguide-ring resonators,” *Opt. Express*, vol. 17, no. 4, pp. 2968–2975, Feb. 2009.

[26] T. Holmgaard, Z. Chen, S. I. Bozhevolnyi, L. Markey, and A. Dereux, “Design and characterization of dielectric-loaded plasmonic directional couplers,” *J. Lightwave Technol.*, vol. 27, no. 24, pp. 5521–5528, Dec. 2009.